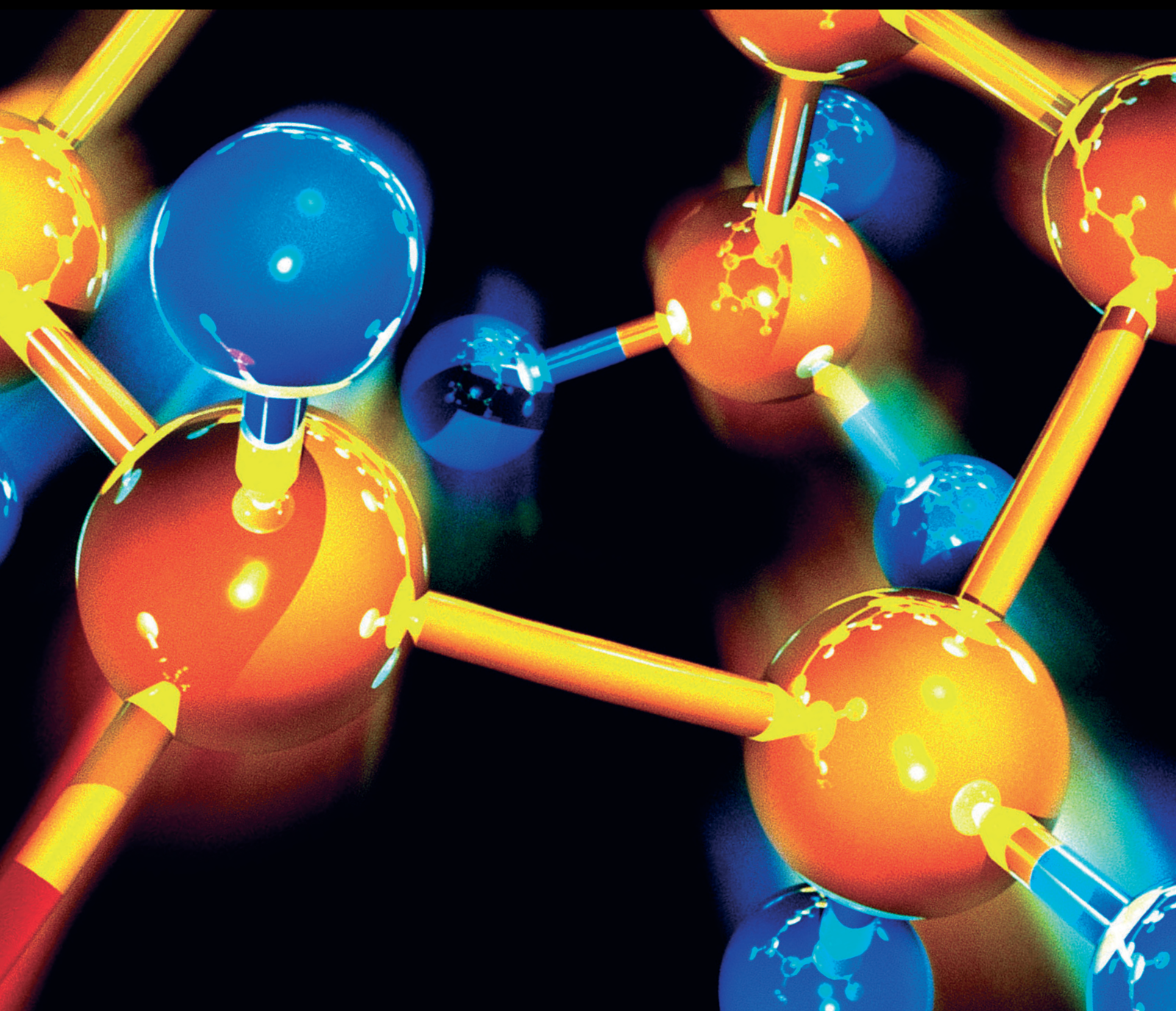


Bionic Structure and Smart Coatings

Lead Guest Editor: Yuxin Wang

Guest Editors: Jian Chen, Guang Cheng, and Zhen He





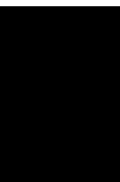
Bionic Structure and Smart Coatings

Journal of Chemistry

Bionic Structure and Smart Coatings

Lead Guest Editor: Yuxin Wang

Guest Editors: Jian Chen, Guang Cheng, and Zhen He



Copyright © 2021 Hindawi Limited. All rights reserved.


This is a special issue published in "Journal of Chemistry." All articles are open access articles distributed under the Creative Commons Attribution License, which permits unrestricted use, distribution, and reproduction in any medium, provided the original work is properly cited.

Chief Editor

Kaustubha Mohanty, India

Associate Editors

Mohammad Al-Ghouthi, Qatar


Tingyue Gu , USA


Teodorico C. Ramalho , Brazil

Artur M. S. Silva , Portugal


Academic Editors

Jinwei Duan, China

Luqman C. Abdullah , Malaysia

Dr Abhilash , India


Amitava Adhikary, USA

Amitava Adhikary , USA

Mozhgan Afshari, Iran

Daryoush Afzali , Iran

Mahmood Ahmed, Pakistan


Islam Al-Akraa , Egypt


Juan D. Alché , Spain

Gomaa A. M. Ali , Egypt

Mohd Sajid Ali , Saudi Arabia

Shafaqat Ali , Pakistan


Patricia E. Allegretti , Argentina

Marco Anni , Italy

Alessandro Arcovito, Italy

Hassan Arida , Saudi Arabia


Umair Ashraf, Pakistan


Narcis Avarvari , France

Davut Avci , Turkey


Chandra Azad , USA

Mohamed Azaroual, France

Rasha Azzam , Egypt


Hassan Azzazy , Egypt

Renal Backov, France

Suresh Kannan Balasingam , Republic of Korea

Sukanta Bar , USA

Florent Barbault , France

Maurizio Barbieri , Italy

James Barker , United Kingdom

Salvatore Barreca , Italy

Jorge Barros-Velázquez , Spain

THANGAGIRI Baskaran , India

Haci Baykara, Ecuador

Michele Benedetti, Italy

Laurent Billon, France

Marek Biziuk, Poland

Jean-Luc Blin , France

Tomislav Bolanca , Croatia

Ankur Bordoloi , India

Cato Brede , Norway


Leonid Breydo , USA


Wybren J. Buma , The Netherlands

J. O. Caceres , Spain

Patrizia Calaminici , Mexico


Claudio Cameselle , Spain

Joaquin Campos , Spain

Dapeng Cao , China

Domenica Capasso , Italy

Stefano Caporali , Italy

Zenilda Cardeal , Brazil

Angela Cardinali , Italy

Stefano Carli , Italy

Maria F. Carvalho , Portugal

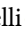
Susana Casal , Portugal


David E. Chavez, USA

Riccardo Chelli , Italy

Zhongfang Chen , Puerto Rico

Vladislav Chrastny , Czech Republic

Roberto Comparelli , Italy

Filomena Conforti , Italy

Luca Conti , Italy


Christophe Coquelet, France

Filomena Corbo , Italy

Jose Corchado , Spain

Maria N. D.S. Cordeiro , Portugal

Claudia Crestini, Italy

Gerald Culioli , France

Nguyen Duc Cuong , Vietnam

Stefano D'Errico , Italy


Matthias D'hooghe , Belgium


Samuel B. Dampare, Ghana

Umashankar Das, Canada

Victor David, Romania

Annalisa De Girolamo, Italy


Antonio De Lucas-Consuegra , Spain

Marcone A. L. De Oliveira , Brazil

Paula G. De Pinho , Portugal

Damião De Sousa , Brazil

Francisco Javier Deive , Spain

Tianlong Deng , China

Fatih Deniz , Turkey
Claudio Di Iaconi, Italy
Irene Dini , Italy
Daniele Dondi, Italy
Yingchao Dong , China
Dennis Douroumis , United Kingdom
John Drexler, USA
Qizhen Du, China
Yuanyuan Duan , China
Philippe Dugourd, France
Frederic Dumur , France
Grégory Durand , France
Mehmet E. Duru, Turkey
Takayuki Ebata , Japan
Arturo Espinosa Ferao , Spain
Valdemar Esteves , Portugal
Cristina Femoni , Italy
Gang Feng, China
Dieter Fenske, Germany
Jorge F. Fernandez-Sanchez , Spain
Alberto Figoli , Italy
Elena Forte, Italy
Sylvain Franger , France
Emiliano Fratini , Italy
Franco Frau , Italy
Bartolo Gabriele , Italy
Guillaume Galliero , France
Andrea Gambaro , Italy
Vijay Kumar Garlapati, India
James W. Gauld , Canada
Barbara Gawdzik , Poland
Pier Luigi Gentili , Italy
Beatrice Giannetta , Italy
Dimosthenis L. Giokas , Greece
Alejandro Giorgetti , Italy
Alexandre Giuliani , France
Elena Gomez , Spain
Yves Grohens, France
Katharina Grupp, Germany
Luis F. Guido , Portugal
Maolin Guo, USA
Wenshan Guo , Australia
Leena Gupta , India
Muhammad J. Habib, USA
Jae Ryang Hahn, Republic of Korea

Christopher G. Hamaker , USA
Ashanul Haque , Saudi Arabia
Yusuke Hara, Japan
Naoki Haraguchi, Japan
Serkos A. Haroutounian , Greece
Rudi Hendra , Indonesia
Javier Hernandez-Borges , Spain
Miguel Herrero, Spain
Mark Hoffmann , USA
Hanmin Huang, China
Doina Humelnicu , Romania
Charlotte Hurel, France
Nenad Ignjatović , Serbia
Ales Imramovsky , Czech Republic
Muhammad Jahangir, Pakistan
Philippe Jeandet , France
Sipak Joyasawal, USA
Sławomir M. Kaczmarek, Poland
Ewa Kaczorek, Poland
Mostafa Khajeh, Iran
Srećko I. Kirin , Croatia
Anton Kokalj , Slovenia
Sevgi Kolaylı , Turkey
Takeshi Kondo , Japan
Christos Kordulis, Greece
Ioannis D. Kostas , Greece
Yiannis Kourkoutas , Greece
Henryk Kozłowski, Poland
Yoshihiro Kudo , Japan
Avvaru Praveen Kumar , Ethiopia
Dhanaji Lade, USA
Isabel Lara , Spain
Jolanta N. Latosinska , Poland
João Paulo Leal , Portugal
Woojin Lee, Kazakhstan
Yuan-Pern Lee , Taiwan
Matthias Lein , New Zealand
Huabing Li, China
Jinan Li , USA
Kokhwa Lim , Singapore
Teik-Cheng Lim , Singapore
Jianqiang Liu , China
Xi Liu , China
Xinyong Liu , China
Zhong-Wen Liu , China







Eulogio J. Llorent-Martínez , Spain
Pasquale Longo , Italy
Pablo Lorenzo-Luis , Spain
Zhang-Hui Lu, China
Devanand Luthria, USA
Konstantin V. Luzyanin , United Kingdom
Basavarajaiah S M, India
Mari Maeda-Yamamoto , Japan
Isabel Mafra , Portugal
Dimitris P. Makris , Greece
Pedro M. Mancini, Argentina
Marcelino Maneiro , Spain
Giuseppe F. Mangiatordi , Italy
Casimiro Mantell , Spain
Carlos A Martínez-Huitle , Brazil
José M. G. Martinho , Portugal
Andrea Mastinu , Italy
Cesar Mateo , Spain
Georgios Matthaiolampakis, USA
Mehrab Mehrvar, Canada
Saurabh Mehta , India
Oinam Romesh Meitei , USA
Saima Q. Memon , Pakistan
Morena Miciaccia, Italy
Maurice Millet , France
Angelo Minucci, Italy
Liviu Mitu , Romania
Hideto Miyabe , Japan
Ahmad Mohammad Alakraa , Egypt
Kaustubha Mohanty, India
Subrata Mondal , India
José Morillo, Spain
Giovanni Morrone , Italy
Ahmed Mourran, Germany
Nagaraju Mupparapu , USA
Markus Muschen, USA
Benjamin Mwashote , USA
Mallikarjuna N. Nadagouda , USA
Lutfun Nahar , United Kingdom
Kamala Kanta Nanda , Peru
Senthilkumar Nangan, Thailand
Mu. Naushad , Saudi Arabia
Gabriel Navarrete-Vazquez , Mexico
Jean-Marie Nedelec , France
Sridhar Goud Nerella , USA
Nagatoshi Nishiwaki , Japan
Tzortzis Nomikos , Greece
Beatriz P. P. Oliveira , Portugal
Leonardo Palmisano , Italy
Mohamed Afzal Pasha , India
Dario Pasini , Italy
Angela Patti , Italy
Massimiliano F. Peana , Italy
Andrea Penoni , Italy
Franc Perdih , Slovenia
Jose A. Pereira , Portugal
Pedro Avila Pérez , Mexico
Maria Grazia Perrone , Italy
Silvia Persichilli , Italy
Thijs A. Peters , Norway
Christophe Petit , France
Marinos Pitsikalis , Greece
Rita Rosa Plá, Argentina
Fabio Polticelli , Italy
Josefina Pons, Spain
V. Prakash Reddy , USA
Thathan Premkumar, Republic of Korea
Maciej Przybyłek , Poland
María Quesada-Moreno , Germany
Maurizio Quinto , Italy
Franck Rabilloud , France
C.R. Raj, India
Sanchayita Rajkhowa , India
Manzoor Rather , India
Enrico Ravera , Italy
Julia Revuelta , Spain
Muhammad Rizwan , Pakistan
Manfredi Rizzo , Italy
Maria P. Robalo , Portugal
Maria Roca , Spain
Nicolas Roche , France
Samuel Rokhum , India
Roberto Romeo , Italy
Antonio M. Romerosa-Nievas , Spain
Arpita Roy , India
Eloy S. Sanz P rez , Spain
Nagaraju Sakkani , USA
Diego Sampedro , Spain
Shengmin Sang , USA

Vikram Sarpe , USA
Adrian Saura-Sanmartin , Spain
Stéphanie Sayen, France
Ewa Schab-Balcerzak , Poland
Hartwig Schulz, Germany
Gulaim A. Seisenbaeva , Sweden
Serkan Selli , Turkey
Murat Senturk , Turkey
Beatrice Severino , Italy
Sunil Shah Shah , USA
Ashutosh Sharma , USA
Hideaki Shirota , Japan
Cláudia G. Silva , Portugal
Ajaya Kumar Singh , India
Vijay Siripuram, USA
Ponnurengam Malliappan Sivakumar ,
Japan
Tomás Sobrino , Spain
Raquel G. Soengas , Spain
Yujiang Song , China
Olivier Soppera, France
Radhey Srivastava , USA
Vivek Srivastava, India
Theocharis C. Stamatatos , Greece
Athanasios Stavrakoudis , Greece
Darren Sun, Singapore
Arun Suneja , USA
Kamal Swami , USA
B.E. Kumara Swamy , India
Elad Tako , USA
Shoufeng Tang, China
Zhenwei Tang , China
Vijai Kumar Reddy Tangadanchu , USA
Franco Tassi, Italy
Alexander Tatarinov, Russia
Lorena Tavano, Italy
Tullia Tedeschi, Italy
Vinod Kumar Tiwari , India
Augusto C. Tome , Portugal
Fernanda Tonelli , Brazil
Naoki Toyooka , Japan
Andrea Trabocchi , Italy
Philippe Trens , France
Ekaterina Tsipis, Russia
Esteban P. Urriolabeitia , Spain

Toyonobu Usuki , Japan
Giuseppe Valacchi , Italy
Ganga Reddy Velma , USA
Marco Viccaro , Italy
Jaime Villaverde , Spain
Marc Visseaux , France
Balaga Viswanadham , India
Alessandro Volonterio , Italy
Zoran Vujcic , Serbia
Chun-Hua Wang , China
Leiming Wang , China
Carmen Wängler , Germany
Wieslaw Wiczkowski , Poland
Bryan M. Wong , USA
Frank Wuest, Canada
Yang Xu, USA
Dharmendra Kumar Yadav , Republic of
Korea
Maria C. Yebra-Biurrún , Spain
Dr Nagesh G Yernale, India
Tomokazu Yoshimura , Japan
Maryam Yousaf, China
Sedat Yurdakal , Turkey
Shin-ichi Yusa , Japan
Claudio Zaccone , Italy
Ronen Zangi, Spain
John CG Zhao , USA
Zhen Zhao, China
Antonio Zizzi , Italy
Mire Zloh , United Kingdom
Grigoris Zoidis , Greece
Deniz ŞAHİN , Turkey

Contents

Preparation and Recent Developments of Ti/SnO₂-Sb Electrodes

Fangcheng Cao , Jingyi Tan , Shengping Zhang , Hongqing Wang , Caizhen Yao , and Yuan Li 


Review Article (13 pages), Article ID 2107939, Volume 2021 (2021)

Corrosion Behaviors of Microarc Oxidation Coating and Anodic Oxidation on 5083 Aluminum Alloy

Haiou Sun, Liangcai Li, Zhongyi Wang , Bin Liu , Meng Wang, and Yunliang Yu



Research Article (11 pages), Article ID 6082812, Volume 2020 (2020)

Preparation of Microfiber Grating for Real-Time Sensing of *Escherichia Coli* Concentration

Qingyan Qiu, Min Dai , Caidong Luo, Ying Mu, Wei Du, Yu Li, Jun Luo, and Rong Li




Research Article (6 pages), Article ID 9016890, Volume 2020 (2020)

Effects of Laser Scanning Speed on Microstructure, Microhardness, and Corrosion Behavior of Laser Cladding Ni45 Coatings

Yanxin Qiao , Jie Huang, Ding Huang, Jian Chen, Wen Liu, Zhengbin Wang , and Zheng Zhibin






Research Article (11 pages), Article ID 1438473, Volume 2020 (2020)

A Simple Way to Achieve Self-Cleaning Surfaces with Unique Antifouling Property

Caizhen Yao , Shizhen Xu , Xiaodong Jiang, Jiaxuan Chen, and Xiaodong Yuan 

Research Article (13 pages), Article ID 9072432, Volume 2020 (2020)

A Low-Cost High-Temperature Sensor Based on Long-Period Fiber/Microfiber Gratings by Local Fictive Temperature Modification

Guorui Zhou, Chuanchao Zhang , Xiufang Xie, Yi Wan, Caizhen Yao , Jun Liu, Longfei Niu, Xinxiang Miao , Hai Zhou, Xiaodong Jiang, Shizhen Xu , and Haibing Lv 

Research Article (6 pages), Article ID 9076874, Volume 2020 (2020)

Evaluation of Oxidation Performance of TRISO Fuel Particles for Postulated Air-Ingress Accident of HTGR

Fangcheng Cao , De Zhang, Qingjie Chen, Hao Li, and Hongqing Wang 

Research Article (8 pages), Article ID 6568987, Volume 2020 (2020)

Review Article

Preparation and Recent Developments of Ti/SnO₂-Sb Electrodes

Fangcheng Cao ¹, Jingyi Tan ², Shengping Zhang ³, Hongqing Wang ¹,
Caizhen Yao ^{3,4} and Yuan Li ⁵

¹School of Chemistry and Chemical Engineering, University of South China, Hengyang 421001, Hunan, China

²School of Health Sciences, Guangzhou Xinhua College, Guangzhou 510520, Guangdong, China

³School of Materials Science and Engineering, Jiangsu University of Science and Technology, Zhenjiang 212003, Jiangsu, China

⁴Laser Fusion Research Center, China Academy of Engineering Physics, Mianyang 621900, Sichuan, China

⁵Institute of Applied Electronics, China Academy of Engineering Physics, Mianyang 621900, Sichuan, China

Correspondence should be addressed to Yuan Li; hankliyuan@126.com

Received 15 May 2020; Accepted 21 July 2020; Published 15 February 2021

Academic Editor: Jian Chen

Copyright © 2021 Fangcheng Cao et al. This is an open access article distributed under the Creative Commons Attribution License, which permits unrestricted use, distribution, and reproduction in any medium, provided the original work is properly cited.

Ti/SnO₂-Sb electrode, which is one of the dimensionally stable anode (DSA) electrodes, offers high specific conductivity, excellent electrocatalytic performance, and great chemical stability. For these reasons, Ti/SnO₂-Sb electrode has been extensively studied in the fields of wastewater treatment. This review covers essential research work about the advanced oxidation technology and related DSA electrodes. It gives an overview of preparation methods of SnO₂ electrodes, including sol-gel method, dip-coating method, electrodeposition method, chemical vapor deposition method, thermal decomposition method, magnetron sputtering method, and hydrothermal method. To extend service life and improve electrocatalytic efficiency, the review provides comprehensive details about the modification technologies of Ti/SnO₂-Sb electrode, such as doping modification, composite modification, and structural modification. In addition, the review discusses common problems in industrial applications of Ti/SnO₂-Sb electrode and highlights the promising outlook of Ti/SnO₂-Sb electrode.

1. Introduction

Nowadays, the treatment of wastewater has become a more challenging issue and a crucial factor for the sustainable development of modern industry, where essential measures are necessary to ensure clean environments. Most environmental pollutants can be successfully eliminated or converted to nontoxic materials by one or more processes, including biological method, physical method, and chemical methods. Regarding the different qualities of wastewater and the variety of organic pollutants in the wastewater, the wastewater treatment procedures would be complicated and different. Compared with biological method and physical method, the removal or alleviation of pollutants in water by a chemical method is easier to control and more effective, which has received an intensive interest for wastewater treatment.

Among the chemistry-based approaches, the advanced oxidation technique is the most common technique for

removal of pollutants in wastewater. Advanced oxidation technology can decompose organic pollutants in wastewater into inorganics such as carbon dioxide and water through the hydroxyl radical OH[•] generated in the oxidation process. Advanced oxidation technology has been widely used because of the following unique advantages: (1) the hydroxyl radical has a powerful oxidation ability; (2) the hydroxyl radical reaction is extensive and nonselective, so it can directly interact with various organic pollutants; (3) the advanced oxidation technology is relatively inexpensive, and the efficiency of organic pollutants degradation can be greatly improved by combining with other treatment technologies [1]. Among the advanced oxidation technologies as shown in Figure 1, electrocatalytic oxidation technology has attracted significant attention for wastewater treatment and is considered to be a potent tool for breaking up even the most resistant organic compounds.

Figure 2 presents the mechanism of electrocatalytic oxidation technology. In electrocatalytic oxidation

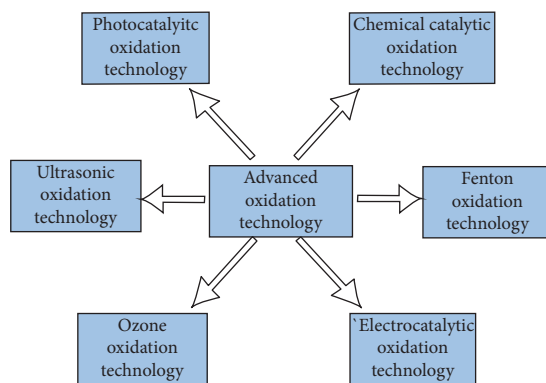


FIGURE 1: Classification of advanced oxidation technology.

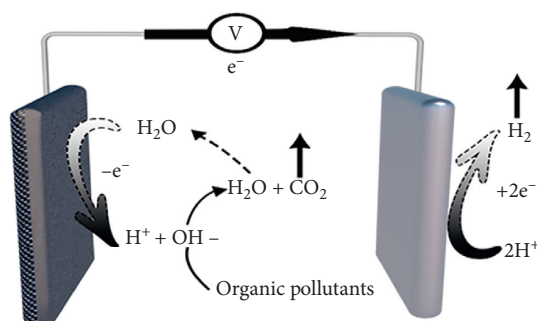


FIGURE 2: Schematic diagram of electrocatalytic oxidation technology.

technology, the electrocatalytic anode material plays a vital role. The electrocatalytic material will directly determine the oxidation process and the final oxidation products. Currently, the main electrocatalytic oxidation electrodes are noble metal electrodes, carbon electrodes, boron-doped diamond (BDD) electrodes, and metal oxide electrodes, of which metal oxide electrodes are also named as DSA electrodes. DSA electrodes have been widely used in various fields due to their advantages of stable size, long service life, high electrocatalytic performance, and low cost.

Table 1 compares four types of DSA electrodes, among which Ti/SnO_2-Sb electrode has a better degradation efficiency for organic pollutants, especially for some toxic organics that are difficult to be degraded, such as perfluorooctanoic acid, acid orange, *p*-chlorophenol, and other organic pollutions. Ti/SnO_2-Sb has a high oxygen evolution potential. The high oxygen evolution potential makes it possible to suppress the occurrence of oxygen evolution—the side reaction during oxidative degradation, thereby improving current efficiency and reducing reaction energy consumption. During the process of electrocatalysis, a large number of hydroxyl radicals can be generated, which significantly enhances the electrocatalytic efficiency of the Ti/SnO_2-Sb electrode. Besides, the doping of Bi, Sb, and other elements can greatly improve the conductivity and electrocatalytic ability of SnO_2 electrodes.

2. Synthesis of SnO_2-Sb Electrode

Currently, there are many preparation methods for Ti/SnO_2-Sb electrodes, including sol-gel method, electrodeposition method, thermal decomposition method, dip-coating method, hydrothermal method, sputtering method, ultrasonic atomization decomposition method, and self-assembly method. It is worth noting that different preparation methods will significantly affect the microstructure and performance of the Ti/SnO_2-Sb electrode. In this review, the fundamentals of each technology are briefly discussed in order to better understand their advantages and limitations for the applications in the removal and treatment of environmental pollutants in wastewater.

2.1. Sol-Gel Method. Sol-gel method mainly undergoes in few steps to generate the final metal oxide and those are hydrolysis, condensation, and drying process. The solution is obtained by dissolving tin-antimony inorganic salt in water or alcohol and then hydrolysis or alcoholysis produces sol particles. After the aggregation of sol particles, a gel is formed. By the pulling method or the coating method using the gel, the film on the titanium plate substrates can be prepared. The dried films are then heat-treated at different temperatures to obtain the electrodes. The tin-antimony oxide electrode prepared by the sol-gel method can cover the surface of the titanium substrate uniformly. However, it was found that when the concentration of the prepared sol is low,

TABLE 1: Comparison of different DSA electrodes.

DSA electrodes	Preparation method	Advantages and disadvantages	Application
Titanium-based manganese dioxide electrode	Thermal decomposition method, electrodeposition method	High-specific heat capacity, low cost, environmentally friendly	Electrocatalytic degradation of organic pollutants, anodizing methanol, electrowinning extraction of nonferrous metals, etc.
Titanium-based lead dioxide electrode	Electrodeposition method	Low cost, good corrosion resistance, good conductivity and simple preparation conditions, high brittleness, difficult machining, secondary pollution during application	Chemical power supply, chemical production, wastewater treatment, etc.
Titanium-based ruthenium-based, and iridium-based electrodes	Thermal decomposition method, electrodeposition method	Low chlorine evolution potential, good stability, short service life, low electrocatalytic ability	Chloralkali industry, wastewater treatment, electrowinning extraction of nonferrous metals, cathodic protection, etc.
Titanium-based antimony-doped tin dioxide electrode	Thermal decomposition method, electrodeposition method, vapor deposition method, etc.	Simple preparation conditions, low cost, high oxygen evolution potential, good electrochemical catalytic ability	Wastewater treatment, organic electrosynthesis, etc.

the spalling of the surface-active layer with poor binding strength would occur. Besides, the viscosity of the sol would also affect the performance of the electrode. At the same time, due to the inevitable volatilization of the solvent during the heat treatment process and the volumetric shrinkage caused by the temperature change, the formation of cracks in electrode would occur. As a result, the possible penetration of electrolyte into the electrodes with cracks and weak binding strength would cause corrosion of the titanium substrate and destroy the stability of the electrode material.

Sol-gel method is facile, economical, high-yield, and suitable for large-scale production of Ti/SnO₂-Sb electrode [2–5]. Duan et al. [2] fabricated an efficient Ti/Sb-SnO₂ electrode modified with nitrogen-doped graphene nanosheets (NGNSs) via a sol-gel method. Compared with a Ti/Sb-SnO₂ electrode, the NGNS-modified electrode possesses a smaller unit crystalline volume, smaller electrical resistivity, and lower charge-transfer resistance. The accelerated lifetime of Ti/Sb-SnO₂-NGNS electrode is prolonged significantly, which is 4.45 times as long as that of Ti/Sb-SnO₂ electrode. The results also indicated that introducing NGNS into the active coating can increase more reaction active sites to enhance the electrocatalytic efficiency. The electrochemical dye decolorization analysis demonstrates that Ti/Sb-SnO₂-NGNS presents efficient electrocatalytic performance for methylene blue and orange II decolorization. Zhong et al. [3] used SnCl₄·5H₂O and SbCl₃ as precursors to synthesize spherical SnO₂-Sb nanoparticles in ethanol solution by a sol-gel method and revealed the effects of calcination temperature and calcination time on the grain size, crystallinity, lattice parameters, and resistivity of the SnO₂-Sb nanoparticles. Zhou et al. [4] reported the preparation of Ti/SnO₂-Sb anode using sol-gel method and investigated the effects of applied current density, initial pH, and inorganic anions on the degradation kinetics.

2.2. Dip-Coating Method. Dip-coating technique process consists of several consecutive steps. First, the substrate should be immersed in the tin-antimony inorganic salt with a constant speed. Next, the substrate with thin layer of

material is pulled up at a constant speed after remaining inside the solution for some time. Alternatively, the precursor solution can be spread by brushing over the pre-treated substrate. The formed film then undergoes a series of heat treatment processes with the redox of the inorganic salt. As a result, a tin-antimony oxide film is obtained. The film properties and film thickness depend on several parameters, such as immersion time, withdrawal speed, number of dipping cycles, solution composition, concentration, and heating temperature [6, 7]. However, the preparation of thick films requires repeated steps of the dip-coating technique, which is time-consuming and labor-intensive. Besides, the limited solubility in the tin-antimony inorganic salt solution affects the application of the method.

Sun et al. [8] studied the electrochemical characteristics of Ti/SnO₂-Sb-Pd electrode prepared by the dip-coating method. Comparing the Ti/SnO₂-Sb electrode and Ti/SnO₂-Sb-Pt anode (as shown in Figure 3), it was found that the activity of tin oxide electrode doped with a small amount of Pd was greatly improved. These results suggested the greatly deteriorated electrochemical activity of both the deactivated undoped and Pd-doped Ti/SnO₂-Sb electrodes.

In addition to the traditional heat treatment in a muffle furnace, different heating sources have been employed for electrode performance improvements. Santos et al. [9] reported the optimization of Ti/SnO₂-Sb synthesis by CO₂ laser as the primary heating source for the first time. The laser-made Ti/SnO₂-Sb anode exhibited better electrocatalytic performance and improved the service life up to 5-fold as compared to the conventionally prepared anodes, envisaging its future applications in wastewater treatment.

2.3. Electrodeposition. Electrodeposition method, also known as electroplating, is an electric current driving deposition method. By controlling the composition of the electrolyte and the precipitation potential, the tin-antimony ions in the aqueous or nonaqueous solution are deposited on the titanium substrate by redox reactions. In general, the Ti/SnO₂-Sb

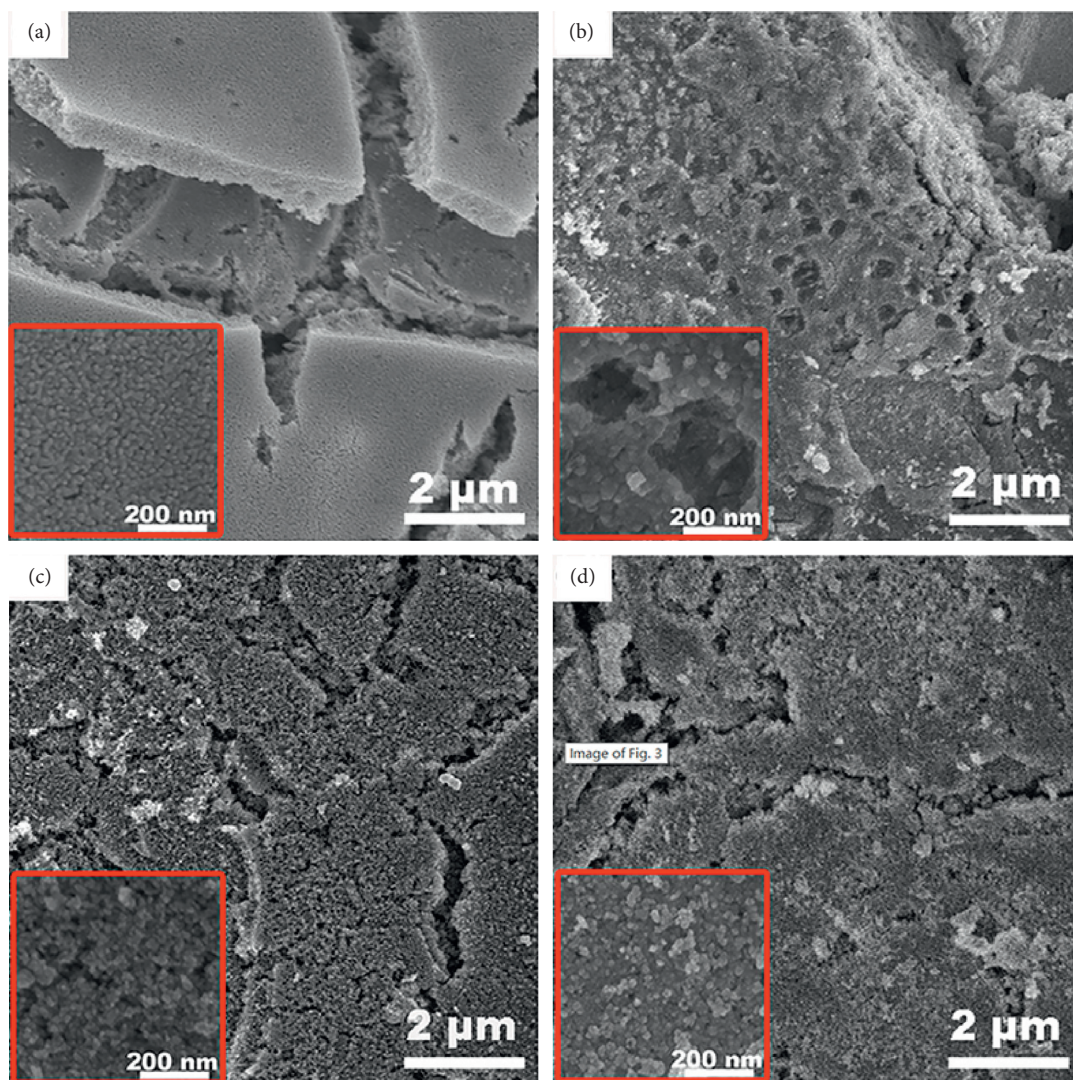


FIGURE 3: SEM images of (a) freshly prepared undoped $\text{Ti/SnO}_2\text{-Sb}$ electrode, (b) deactivated undoped $\text{Ti/SnO}_2\text{-Sb}$ electrode, (c) freshly prepared Pd-doped $\text{Ti/SnO}_2\text{-Sb}$ electrode, and (d) deactivated Pd-doped $\text{Ti/SnO}_2\text{-Sb}$ electrode; the insets show the enlargement of local area [8].

electrode prepared by electrodeposition has excellent binding strength and uniform thickness without cracks. Besides, the electrochemical deposition process is relatively simple and easy to control. Electrodeposition gives a precise control of the structure and performance of the coating.

The electrodeposition generally starts with the cathode electrodeposition step in electrolytic solutions, followed by the calcination step to form mixed metal oxides [10–12]. Duan et al. [12] fabricated different $\text{Ti/SnO}_2\text{-Sb}$ electrodes using pulsed electrodeposition in a colloidal medium. Compared with an electrode prepared in an aqueous solution, these electrodes had a rougher and more compact surface with smaller grain sizes. The electrodes prepared in a colloidal medium displayed high oxygen evolution potentials, low charge exchange resistances, significantly enhanced lifetimes, and superior electrocatalytic activities. These electrodes also performed better for the adsorption and decolorization of methyl orange. Sun et al. [13] provided an eco-friendly, economical, and facile method for fabricating

$\text{Ti/SnO}_2\text{-Sb}$ electrode with high performance via electrodeposition using a deep eutectic solvent, which showed better electrochemical activity and longer service life than the conventional $\text{Ti/SnO}_2\text{-Sb}$ electrode electrodeposited using aqueous solvent.

Furthermore, some recent research directly fabricated $\text{SnO}_2\text{-Sb}$ anode by pulse reverse electrodeposition technique, without the traditional calcination procedures [14, 15]. Wu et al. [14] developed a unique $\text{SnO}_2\text{-Sb}$ anode on TiO_2 nanotubes by a pulse reverse electrodeposition method, which presented a high oxygen evolution potential and a strong electrochemical oxidation ability. Compared with the $\text{SnO}_2\text{-Sb}$ electrode prepared by traditional sol-gel method, the SnO_2 electrode prepared by the pulse electrodeposition method had a higher crystallinity and lower oxygen vacancy concentration. Besides, the SnO_2 electrode exhibited total organic carbon removal rates and mineralization efficiency, which are 2.6 times and 3.3 times of that for the traditional SnO_2 electrode, respectively.

2.4. Chemical Vapor Deposition. Chemical vapor deposition has been widely used in the development of various thin film materials with high purity and density. During chemical vapor deposition, the constituents of a vapor phase, often diluted with an inert carrier gas, are introduced into a reaction chamber and adsorbed on a heated substrate surface, which results in a solid coating via a chemical reaction. During the process, the substrate temperature is critical and can influence the occurrence of different reactions. Besides, several gradients or variable coatings can also be obtained by changing the gas phase composition.

Yao et al. [16] fabricated the Ti/SnO₂ anodes by chemical vapor deposition using a gas phase mixture of SnCl₄ and H₂O as a precursor at 550°C. It was found that the new electrodes had compact microstructure, high overpotential for oxygen evolution, and superior activity for pollutant oxidation. The surface quality of the electrode prepared by the chemical vapor deposition method could be well controlled, but the relatively expensive vapor precursor limits the chemical vapor deposition method in the application of Ti/SnO₂-Sb synthesis. To overcome the cost and throughput limitations of high vacuum techniques of the chemical vapor deposition method, Scott et al. [17] developed SnO₂-Sb thin films via mist chemical vapor deposition, a nonvacuum solution-based technique that involves the gas-assisted transport of ultrasonically generated aerosols from simple aqueous Sn and Sb precursors. The electrical properties of the resulting films were similar to those achieved using molecular beam epitaxy and other more sophisticated high vacuum techniques.

2.5. Self-Assembly Method. The self-assembly technique is the spontaneous association and organization of numerous individual units, such as molecules, nanomaterials, micrometers, or larger-scale components into coherent and well-defined structures without external intervention. Self-assembly involves diffusion followed by the association of molecules through noncovalent interactions, such as hydrogen bonding, ionic bonding, hydrophobic interactions, and van der Waals interactions. These interactions, although weak, are capable of forming the higher ordered structures.

Liu et al. [18] synthesized self-assembled 3D flower-like SnO₂ architectures. Fan et al. [19] fabricated SnO₂ mesoporous films through a sol-gel-based self-assembly process using Pluronic P-123 as a structure-directing agent. The self-assembled 3D flowerlike or mesoporous SnO₂ architectures possessed excellent electrical conductive performance and high specific surface area; thus, the SnO₂ electrodes would present remarkable electrochemical performance. Li et al. [20] prepared a SnO₂/TiO₂-NTs electrode with a 2D macropore structure using a self-assembly method with liquid crystal flexible membrane. It was found that this electrode showed good photocatalytic performance and electrocatalytic performance. Therefore, it exhibited high-efficiency photoelectric synergistic oxidation performance when degrading organic pollution. Fan et al. [21] fabricated a new SnO₂-Sb electrode with a high specific surface area and excellent electrocatalytic oxidation performance by

evaporation-induced self-assembly. The results showed that the SnO₂-Sb electrode had nano-scale particles, high crystallinity, and ordered porous structures. The porous structures provided more in situ active sites and promoted the adsorption of organic pollutants. Therefore, the mesoporous SnO₂-Sb electrodes possessed better electrochemical activity than traditional tin-antimony oxide electrode and higher kinetic constant, and its initial mineralization current efficiency could also be greatly improved. Wang et al. [22] synthesized SnO₂-Sb nano-thin film electrodes by template-assisted self-assembly, which presented good electrical conductivity, and had extremely high crystallinity with an ordered mesoporous structure.

2.6. Ultrasonic Spray Pyrolysis Method. The liquid in the form of thin film when allowed to flow on a vibrating surface (frequency >20 kHz) breaks up into fine droplets. This phenomenon is known as ultrasonic atomization. During ultrasonic atomization, the metal salt solution is sprayed onto the pretreated titanium substrate. After dry and heat treatment, an oxide film on the substrate could be obtained. For the ultrasonic spray pyrolysis technology, the required operation equipment is relatively inexpensive, and the decomposition conditions are easy to control. Besides, the microstructure of the film surface can be optimized by the formation of ultrafine liquid droplets via ultrasonic atomization, thereby improving the performance of the film.

Until now, many literatures have reported SnO₂ film prepared via ultrasonic spray pyrolysis [23–27]. Chen et al. [25] fabricated Ti/SnO₂-Sb electrode with different nickel concentrations by a spray pyrolysis technique. The nickel and antimony co-doped Ti/SnO₂ anodes showed different structures and onset potential for oxygen evolution. SnO₂ thin films grew in preferential orientation along the (101) plane as the nickel concentration increases. The onset potential of oxygen increased due to the introduction of nickel doping. These results are significant in developing advanced SnO₂-based electrodes with a high oxidation potential to treat a broad kind of organic pollutant. Sánchez-García et al. [26] used tin dichloride ethanol solution as the raw material to quickly prepare tin dioxide film by an ultrasonic spray pyrolysis method. The results showed that the film prepared by this method was uniform and dense, whose surface could be completely oxidized. Besides, the film thickness and surface uniformity could also be well controlled. Yao [27] deposited the Sb doping SnO₂ film on the titanium substrate by ultrasonic spray pyrolysis at 600°C. The results showed that the crystal size of SnO₂-Sb increased with the increasing doping content. When the doping level of Sb was about 3%, the Ti/SnO₂-Sb electrode possessed the lowest resistivity and the best electrocatalytic activity.

2.7. Hydrothermal Method. Hydrothermal synthesis refers to heterogeneous reactions in a sealed and heated solution above ambient temperature and pressure. Hydrothermal synthesis facilitates the solubility and chemical reactions of the hardly soluble metal salt precursors in hot water (or organic solvent) under high pressure, followed by

supersaturation and crystallization. Generally, the pretreated titanium substrate is usually put into an aqueous solution under high-temperature and high-pressure conditions, and a tin-antimony oxide film is directly formed on the titanium substrate after the hydrothermal reaction.

Xu et al. [28] embedded SnO₂-Sb into TiO₂ nanotubes by hydrothermal synthesis to form a three-dimensional electrode (TiO₂-NTs/Sb-SnO₂). Compared with the Ti/SnO₂-Sb₂O₅ electrode prepared by conventional methods, the TiO₂-NTs/SnO₂-Sb electrode prepared exhibited a higher density and longer service life. An et al. [29] developed SnO₂-Sb film coated with sol layer by a hydrothermal method and spin coating method with the formation of solution-based transparent conductive oxides. The results showed that the SnO₂-Sb film with five sol layers had excellent resistivity and light transmittance. Besides, the increase in the density and thickness of the sol coating layer could improve the performance of the film. However, the increase in carrier concentration led to a reduction of mobility. Xu and Lian [30] designed a novel SnO₂-Sb nanorod anode with Ti sheet as a substrate (Ti/SnO₂-Sb-NRs) through the hydrothermal process. The results indicated that Ti/SnO₂-Sb-NRs anode possessed SnO₂-Sb-NRs which were about 70 nm in width, as well as a better wettability, a lower charge-transfer resistance, a larger current at constant potential, and a longer lifetime than the conventional Ti/SnO₂-Sb anode prepared by pulse electrodeposition. Yang et al. [31] successfully fabricated Ti/SnO₂-Sb electrode with a nano-scaled sphere-stacking structure using a solvothermal synthesis approach, which possessed superior electrochemical properties to an electrode prepared using dip-coating methods.

2.8. Magnetron Sputtering Method. Magnetron sputtering is a versatile method to create very dense films with good adhesion. Magnetron sputtering is a plasma-based coating method that generates a magnetically confined plasma near the surface of a target. Then, positively charged energetic ions from the plasma collide with the negatively charged target material, and atoms from the target are ejected or sputtered, which then deposit on a substrate. The magnetron sputtering method has been widely employed in the preparation of various alloys and compounds. Montero et al. [32] deposited SnO₂-Sb thin films from metal targets onto glass substrates by direct current magnetron sputtering at room temperature. The results showed that the deposited films exhibited amorphous or nanocrystalline structures. Besides, the optical and electrical properties of the film mainly depended on the deposition parameters. Yan et al. [33] obtained Ti/SnO₂-Sb anodes with a microrod structure prepared by magnetron sputtering. The SnO₂ coating on the above Ti substrate by magnetron sputtering with postannealing was comprised of microrod and had longer service time than the traditional Ti/SnO₂ anode.

3. Research Progress of Ti/SnO₂-Sb Electrode

Ti/SnO₂-Sb electrode has various advantages, but it is worth noting that the relatively short service life and unstable electrocatalytic efficiency limit the application of titanium-based tin-antimony oxide electrode. In recent years, many

studies aim to improve both the service life and electrocatalytic performance of tin-antimony oxide electrodes. For instance, it was found that increasing the bonding strength between the surface-active layer and the substrate could prevent the corrosion failure inside the electrodes. Therefore, it is of great importance to develop appropriate modification techniques for electrodes. Currently, the modification technology includes doping modification, structural modification, and composite modification.

3.1. Doping Modification. Doping different elements into Ti/SnO₂-Sb electrodes can effectively promote electrocatalytic oxidation performance, electrode life, and surface morphology of electrodes. The doping elements for the modification of Ti/SnO₂-Sb electrode can be included as follows:

- (1) Doping of rare Earth metals, such as Nd, Eu, and Dy [34–36]. Zhu et al. [35] investigated Ti/SnO₂-Sb electrodes doped with different rare Earth elements (Ce, Dy, La, and Eu), which were prepared by the thermal decomposition method at 550°C (as shown in Figure 4). The results demonstrated that the electrocatalytic degradation performances of Ti/SnO₂-Sb electrodes were improved to different levels by doping different rare Earth ions. According to the improvement effects, the electrodes doped with four rare Earth elements rank in the order: Ti/SnO₂-Sb-La electrode > Ti/SnO₂-Sb-Eu electrode > Ti/SnO₂-Sb-Dy electrode > Ti/SnO₂-Sb-Ce electrode. It worth noting that Ti/SnO₂-Sb-La electrode has a higher oxygen evolution potential, better electrocatalytic activity, and longer electrode life. Li et al. [36] prepared a Pd-modified Ti/SnO₂-Sb anode via thermal decomposition. It was found that Pd doping could effectively change the surface morphology and lattice parameters of the metal oxide electrode. Pd can also facilitate the entry of more Sb into SnO₂ crystals and promote the reduction of Sb. At the same time, with Pd doping, the lifetime of the electrode was increased more than 40 times, demonstrating the good potential for application in industry.
- (2) Doping of precious metals, such as Pt, Ru, and Ir [37, 38]. Berenguer et al. [38] compared Pt- and Ru-doped Ti/SnO₂-Sb anodes to conventional Ti/RuO₂ and Ti/Co₃O₄ anodes. It was found that the Ti/SnO₂-Pt anode exhibits the best electroactivity, fastest kinetics, and highest current efficiency among the studied anodes but poor electrochemical stability. The introduction of small amounts of Ru (3.25–9.75 at.%) brings about a slight loss of the electrocatalytic performance, but it causes a remarkable increase in the stability of the electrode.
- (3) Doping with iron group metals and other metals, such as Fe, Co, and Ni [37, 39]. Yang et al. [37] studied six elements of Fe, Ni, Co, Ru, Ce, and Pd doped into the optimized SnO₂-Sb electrode, which aimed to reveal the most effective dopants and the

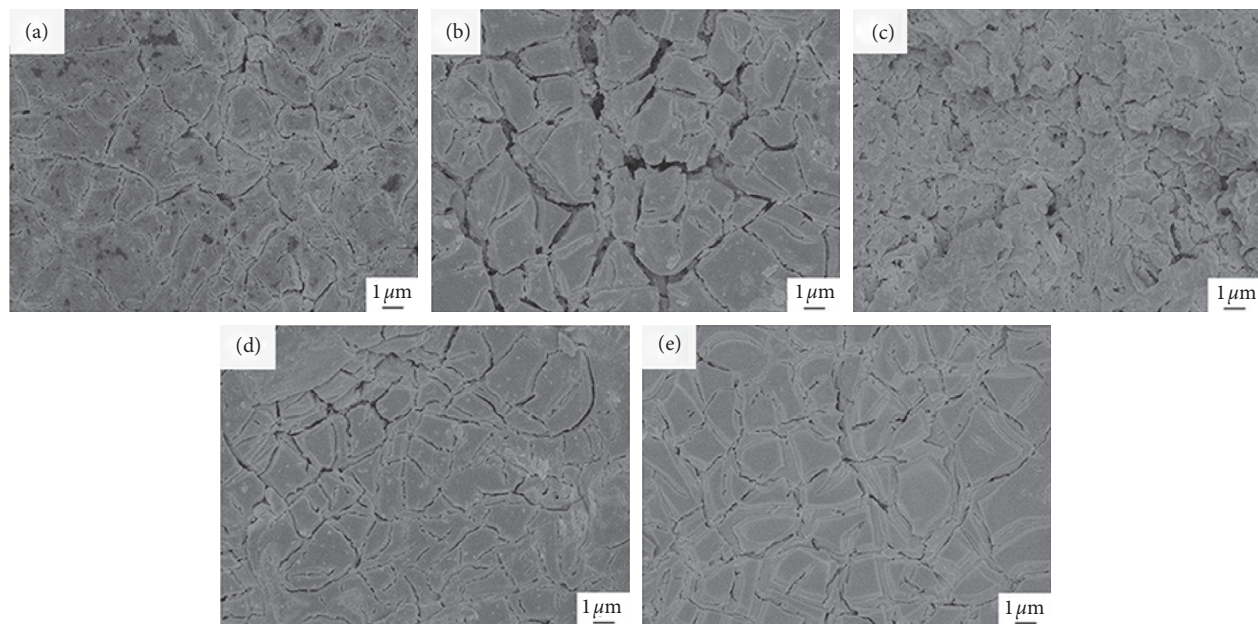


FIGURE 4: SEM images of Ti/SnO₂-Sb electrodes undoped and doped with different rare earths: (a) undoped; (b) Ce; (c) Dy; (d) La; (e) Eu [35].

best combinations to improve the electrocatalytic activity of SnO₂ electrode to pollutants. The results showed that the optimal doping amount of Sb in the Sb-SnO₂ electrode was 5–10%. The doping of Ni and Fe enhanced the electrocatalytic activity of the electrode. Notably, the doping of Ni significantly increased the degradation efficiency of phenol and the removal rates of total organic carbon. However, the doping of precious metals, such as Pd, Ru, and Co, led to a significant reduction in the oxygen evolution potential of the electrode, resulting in low efficiency of the electrode when degrading pollutants. Liang et al. [39] investigated the effect of Mo with different molar ratios on the characterization of Ti/SnO₂-Sb-Mo electrodes prepared by the sol-gel method (as shown in Figure 5). The results showed that the electrode at the Mo content of 1 at.% provided optimal catalytic activity for phenol degradation and the longest lifetime. The Ti/SnO₂-Sb electrode coating with 7 at.% Mo presented the highest oxygen evolution overpotential, indicating the diverse effects for different Mo molar ratio doping.

3.2. Compound Modification. Compound modification methods mainly include metal-metal carbide compound, metal nitride compound, nanocarbon material compound, and organic polymer compound [10, 40–44]. Since the electrode prepared by the electrodeposition method has good binding strength and the morphology and thickness of the deposited layer can be controlled by adjusting the parameters, the nanomaterial is mainly doped into the coating by means of electrodeposition. Duan et al. [10] prepared Ti/SnO₂-Sb electrode modified with TiN nanoparticles by a

pulse electrodeposition method. The prepared Ti/Sb-SnO₂-TiN electrode had a dense film structure and a small unit cell volume (as shown in Figure 6). Compared to traditional Ti/SnO₂-Sb electrode, Ti/Sb-SnO₂-TiN electrode had higher decolorization efficiency and kinetic rate constant (as shown in Figure 7). Zhang et al. [41] prepared a new type of CNT-modified Ti/SnO₂-Sb electrode by pulse electrodeposition. Compared with the electrode without CNT modification, the electrode modified with CNT had a larger specific surface area and smaller microcrystalline particles. Besides, the electrode modified with CNT had higher oxygen evolution potential, kinetic rate constant, chemical oxygen demand, total organic carbon removal rate, and mineralization current efficiency. Pahlevani et al. [42] synthesized Ti/SnO₂-Sb electrode modified by graphene oxide using dip-coating technique and thermochemical decomposition, with the formation of uniform SnO₂ nanoparticles ranging 15–26 nm and presence of reduced graphene oxide. The graphene oxide modified anode led to a higher oxygen evolution overpotential and less energy being consumed for competitive reactions, resulting in high electrocatalytic activity for the fabricated anode.

Li et al. [43] investigated the electrocatalytic degradation of aniline by Ti/SnO₂-Sb, Ti/Sb-SnO₂/Pb₃O₄, and Ti/Sb-SnO₂/PbO₂ anodes in different electrolytes. In 5 wt% Na₂SO₄ electrolyte, aniline could be degraded relatively faster on the Ti/Sb-SnO₂ anode. While in 5 wt% NaCl electrolyte, Ti/Sb-SnO₂/Pb₃O₄ would be more beneficial for aniline degradation. Besides, the Ti/Sb-SnO₂/PbO₂ could exhibit a better capability to enhance biodegradability in both electrolytes. Jin et al. [44] deposited SnO₂-Sb and α -PbO₂ onto the surface of a titanium substrate, followed by the fabrication of β -PbO₂ doped with Fe element and

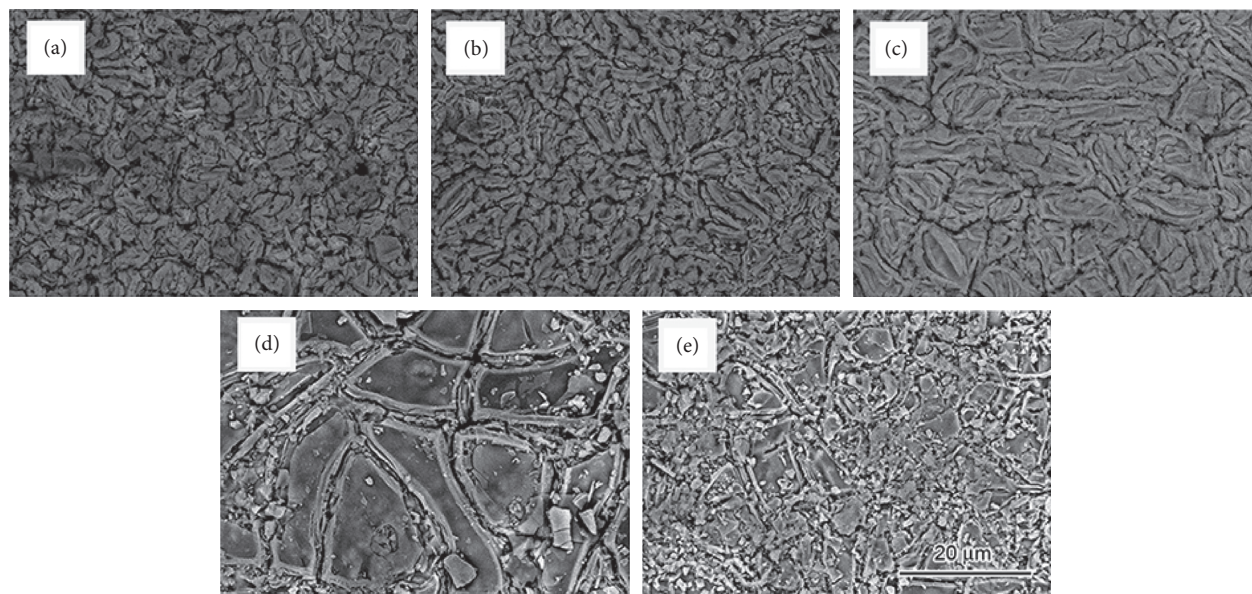


FIGURE 5: SEM images of Ti/SnO₂-Sb-Mo electrodes of different Mo doping molar ratios: (a) 0.0 at.%; (b) 1.0 at.%; (c) 3.0 at.%; (d) 5.0 at.%; (e) 7.0 at.% [39].

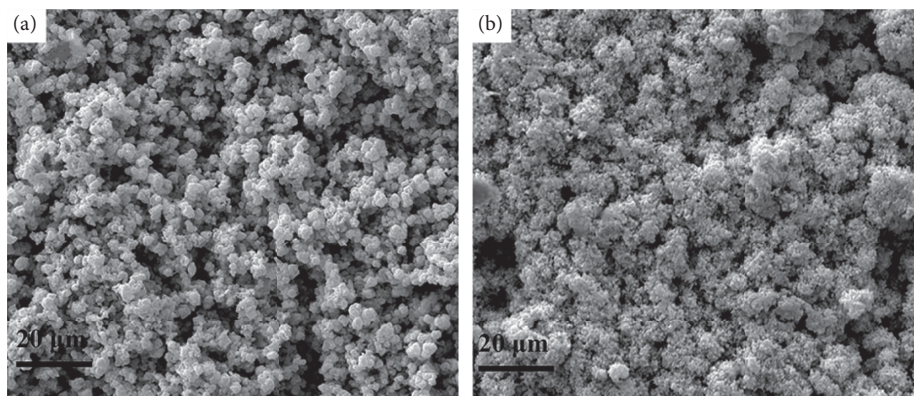


FIGURE 6: SEM images of (a) Ti/Sb-SnO₂ electrode and (b) Ti/Sb-SnO₂-TiN electrode [10].

polytetrafluoroethylene (PTFE) thereon. The optimized superhydrophobic electrode modified with PTFE exhibited lower charge-transfer resistance and good oxidative ability towards organics. Due to the collaborative contribution of α -PbO₂ and PTFE, the stability of the Ti/SnO₂-Sb/ α -PbO₂/Fe- β -PbO₂-PTFE electrode was found to be significantly improved. Such superhydrophobic Ti/SnO₂-Sb/ α -PbO₂/Fe- β -PbO₂-PTFE electrodes could effectively degrade organic pollutants under low voltages, which is of great significance for reducing energy consumption.

3.3. Structural Modification. The structural modification methods for Ti/Sb-SnO₂ electrodes mainly include intermediate layer structural modification and active layer structural modification. The intermediate layer structure modification method consists of the addition of the intermediate layer and the modification of the titanium-based structure. The addition of the intermediate layer can increase

the binding strength between the active layer and the substrate, prevent the substrate from being passivated after corrosion, extend the service life, and improve the stability of the electrode during electrocatalytic degradation. Santos et al. [45] used 4 or 16 repetitive alternating Sn and Sb electrodeposition methods on the titanium foil with Pt as the intermediate layer, and finally, Ti/Pt/SnO₂-Sb₂O₄ electrode was obtained after high-temperature calcination. Compared with traditional Ti/SnO₂-Sb₂O₄ electrode with Pt as the middle layer had a higher service life, electrochemical stability, and mechanical stability. Furthermore, it was found that the Ti/Pt/SnO₂-Sb₂O₄ electrode had high removal rates of chemical oxygen demand to chloroauric acid, diclofenac, and ibuprofen. Bi et al. [46] prepared Ti/SnO₂-Sb-La electrodes by the sol-gel method with two kinds of Ce-Mn and Fe-Mn composite intermediate layers, a Mn intermediate layer, or no intermediate layer (as shown in Figure 8). The results indicated the lifetime of the electrode with the intermediate layer

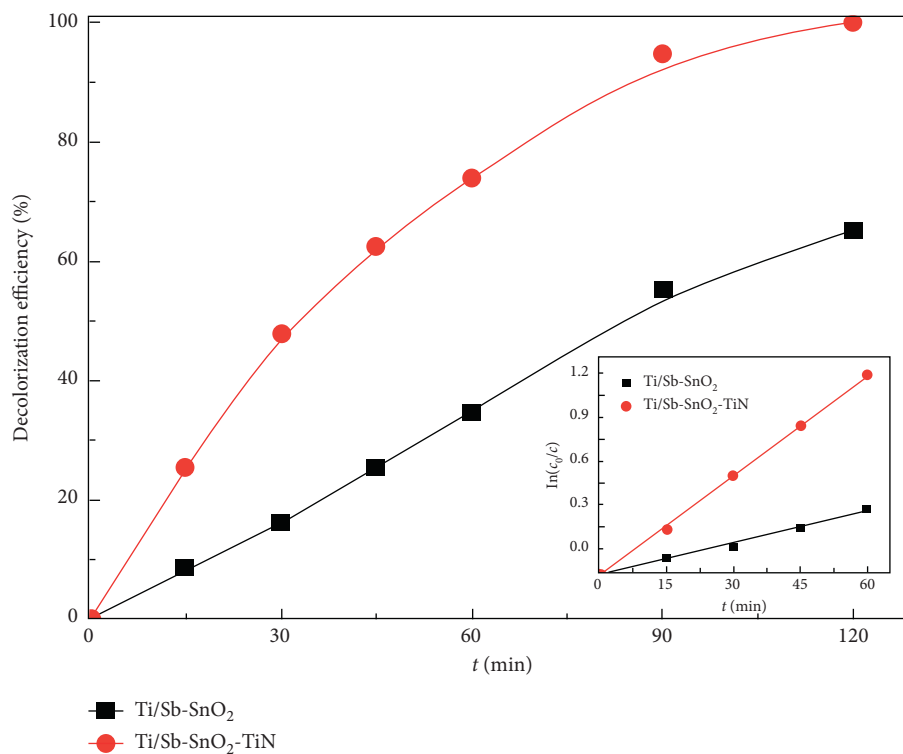


FIGURE 7: Variations in decolorization efficiency with time. The inset is the pseudo-first-order of methylene blue decolorization on Ti/Sb-SnO₂ and Ti/Sb-SnO₂-TiN electrodes [10].

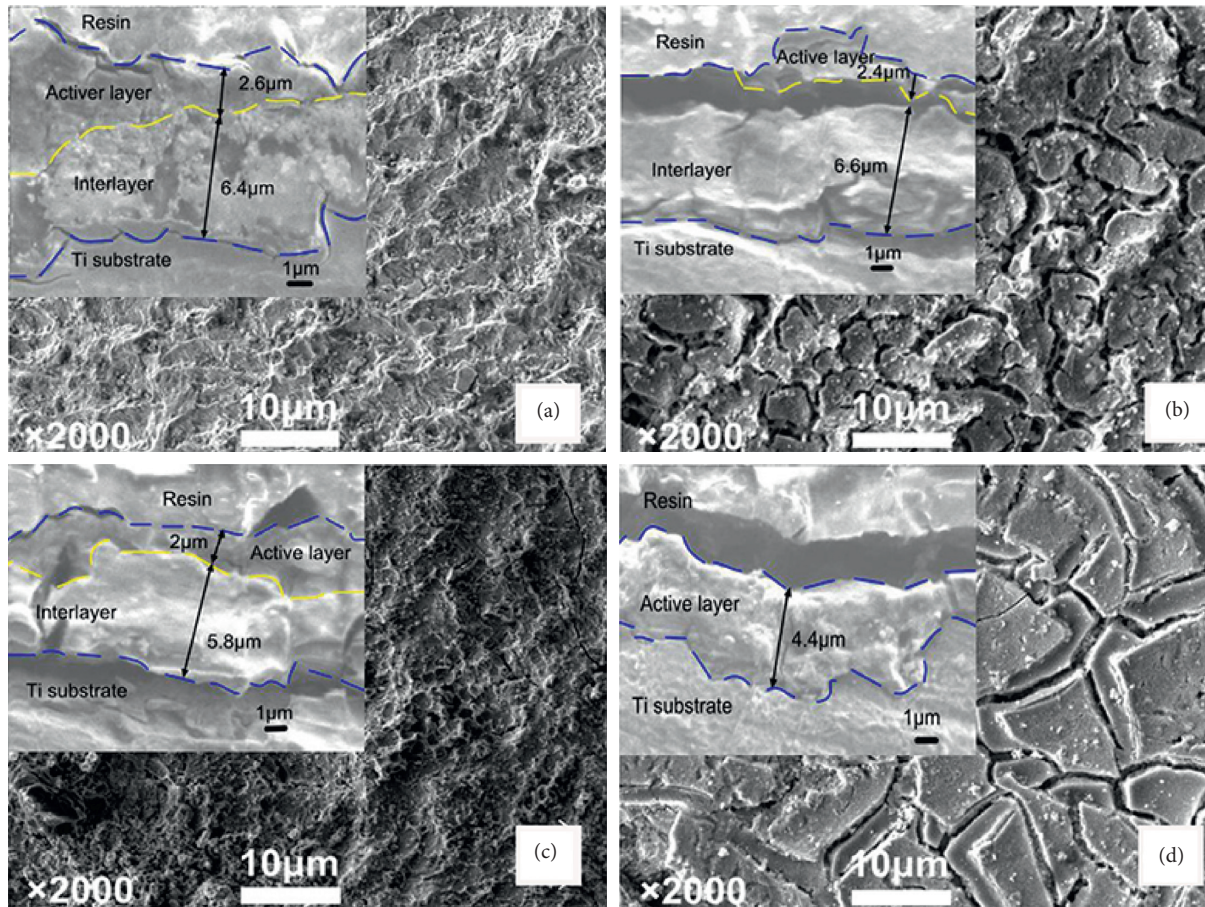


FIGURE 8: SEM images of different electrodes: (a) Ti/Ce-Mn/SnO₂-Sb-La; (b) Ti/Fe-Mn/SnO₂-Sb-La; (c) Ti/Mn/SnO₂-Sb-La; (d) Ti/SnO₂-Sb-La [46].

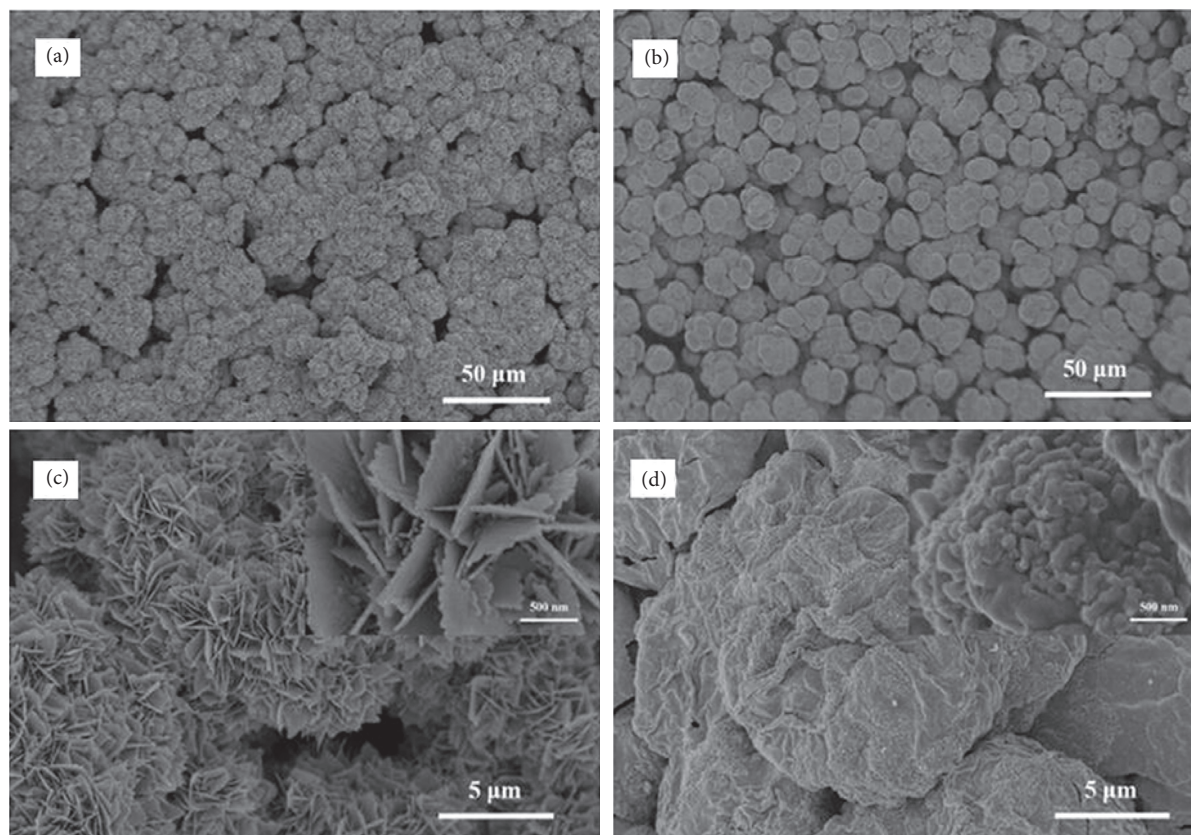


FIGURE 9: SEM images of the surface morphologies of (a, c) Ti/SnO₂-Sb-HFs electrode and (b, d) Ti/SnO₂-Sb electrode [50].

increased. Especially, the electrochemical performance of the electrode can be significantly improved by adding a Ce-Mn composite intermediate layer with high oxygen evolution potential. Moreover, such addition also enhances the capacity of the electrode for electrocatalytic oxidation degradation of phenol to some degrees, showing high removal rate of phenol and the maximum removal rate of chemical oxygen demand.

The primary way to modify the titanium-based structure is to obtain a highly ordered array of titanium dioxide nanotubes (TiO₂-NTs) by anodizing the titanium plate surface. TiO₂-NTs as a tubular template can increase the contact area between the surface-active layer and the matrix and the specific surface area of the active layer to provide more active sites for the catalytic layer. Wang et al. [47] prepared Sb-doped SnO₂ coatings on different TiO₂-NTs substrates by electrodeposition with different anodic oxidation times and voltages of the titanium substrate. The results indicated that TiO₂-NTs could significantly improve the electrocatalytic efficiency of the electrodes. Meanwhile, the pore size and length of TiO₂-NTs played a crucial role in the degradation efficiency of TiO₂-NTs/SnO₂-Sb electrode. When the pore size of TiO₂-NTs was 85 nm and the length was 5 μm, the electrode had the best degradation efficiency on target pollutants.

The active layer structure modification method is actually to prepare Ti/SnO₂-Sb electrode with special active layer structure to improve the electrocatalytic ability of the

electrode. Asim et al. [48] developed a simple template removal method to prepare two different types of layered porous SnO₂-Sb electrodes (honeycomb Ti/Sb-SnO₂ electrodes and mesh Ti/Sb-SnO₂ electrodes). In terms of microstructures, both the two types of electrodes presented extremely high porosity and were arranged layer by layer in multiple directions. The high specific surface area results in more electrochemically active sites on the electrode surface. Compared with traditional SnO₂-Sb electrodes, these two types of porous electrodes exhibited better electrochemical activity and higher reaction rates for electrocatalytically degrading organic pollutants. Besides, the presence of porous channels could significantly promote adsorption and diffusion of pollutant molecules. Moir et al. [49] prepared a 3D SnO₂-Sb nanoelectrode with a disordered macropore structure by the template method. The results showed that the 3D macropore structure improved the specific surface area of the active layer significantly, so the electrode possessed an efficient electrocatalytic performance. Recently, Wang et al. [50] achieved a novel Ti/SnO₂-Sb electrode with a 3D hierarchical flower-like structure (HFs), which was firstly prepared using a hydrothermal method. Compared the traditional Ti/SnO₂-Sb electrode, this novel Ti/SnO₂-Sb-HFs electrode has a larger electrochemical active surface area, a lower charge-transfer resistance, and a higher oxygen evolution potential (as shown in Figure 9). Especially, the stability of the electrode is improved most obviously.

4. Conclusion

Electrocatalytic oxidation technology has attracted much interest in the field of water treatment technology. Based on this technology, it is of great importance to choose proper electrode materials. Among them, Ti/Sb-SnO₂ electrode has been widely used in various fields due to its good conductivity and stability. However, the shortages including low catalytic performance and poor stability limited the industrial applications of the electrode. To expand the application of the Ti/Sb-SnO₂ electrode, the following problems are urgent to be solved:

- (1) The traditional Ti/Sb-SnO₂ electrode has relatively poor stability and short service life. Although modification technology can improve its service life to a certain extent, the service life is still shorter than other DSA electrodes.
- (2) The electrode synthesized by electrodeposition has good binding strength and long service life, but generally with low catalytic efficiency, which affects the efficiency of degrading organic pollutants in wastewater. In addition, when the electrode is prepared by the electrodeposition with the aqueous solution system, the stress in coating caused by hydrogen inclusions would produce blisters or cracks.
- (3) Most of the modification techniques for Ti/SnO₂-Sb electrodes have their own limitations. Therefore, developing Ti/Sb-SnO₂ electrodes with high catalytic efficiency and good binding strength still needs to be investigated.

Conflicts of Interest

The authors declare that they have no conflicts of interest.

Authors' Contributions

Fangcheng Cao and Jingyi Tan contributed equally to this paper.

Acknowledgments

The authors would like to acknowledge the funding from the projects supported by the National Natural Science Foundation of China (nos. 51701087, 51535003, and 12005094), the Natural Science Foundation of Hunan Province (no. 2020JJ5485), and the Research Foundation of Education Bureau of Hunan Province (no. 18C0450).

References

- [1] M. E. H. Bergmann, A. S. Kopalal, and T. Iourtchouk, "Electrochemical advanced oxidation processes, formation of halogenate and perhalogenate species: a critical review," *Critical Reviews in Environmental Science and Technology*, vol. 44, no. 4, pp. 348–390, 2014.
- [2] T. Duan, Q. Wen, Y. Chen, Y. Zhou, and Y. Duan, "Enhancing electrocatalytic performance of Sb-doped SnO₂ electrode by compositing nitrogen-doped graphene nanosheets," *Journal of Hazardous Materials*, vol. 280, pp. 304–314, 2014.
- [3] X. Zhong, B. Yang, X. Zhang, J. Jia, and G. Yi, "Effect of calcining temperature and time on the characteristics of Sb-doped SnO₂ nanoparticles synthesized by the sol-gel method," *Particuology*, vol. 10, no. 3, pp. 365–370, 2012.
- [4] C. Zhou, Y. Wang, J. Chen, L. Xu, H. Huang, and J. Niu, "High-efficiency electrochemical degradation of antiviral drug abacavir using a penetration flux porous Ti/SnO₂-Sb anode," *Chemosphere*, vol. 225, pp. 304–310, 2019.
- [5] D. Zhi, J. Qin, H. Zhou, J. Wang, and S. Yang, "Removal of tetracycline by electrochemical oxidation using a Ti/SnO₂-Sb anode: characterization, kinetics, and degradation pathway," *Journal of Applied Electrochemistry*, vol. 47, no. 12, pp. 1313–1322, 2017.
- [6] Y. Duan, Q. Wen, Y. Chen, T. Duan, and Y. Zhou, "Preparation and characterization of TiN-doped Ti/SnO₂-Sb electrode by dip coating for orange II decolorization," *Applied Surface Science*, vol. 320, pp. 746–755, 2014.
- [7] A. Chen, S. Xia, H. Pan et al., "A promising Ti/SnO₂ anodes modified by Nb/Sb co-doping," *Journal of Electroanalytical Chemistry*, vol. 824, pp. 169–174, 2018.
- [8] Y. Sun, S. Cheng, Z. Yu, L. Li, C. Li, and J. Yang, "Elucidating deactivation mechanisms of Pd-doped and un-doped Ti/SnO₂-Sb electrodes," *Journal of Alloys and Compounds*, vol. 834, p. 155184, 2020.
- [9] G. de O S Santos, V. M. Vasconcelos, R. S. da Silva, M. A. Rodrigo, K. I. B. Eguiluz, and G. R. Salazar-Banda, "New laser-based method for the synthesis of stable and active Ti/SnO₂-Sb anodes," *Electrochimica Acta*, vol. 332, p. 135478, 2020.
- [10] T. Duan, Y. Chen, Q. Wen, and Y. Duan, "Enhanced electrocatalytic activity of nano-TiN composited Ti/Sb-SnO₂ electrode fabricated by pulse electrodeposition for methylene blue decolorization," *RSC Advances*, vol. 4, no. 101, pp. 57463–57475, 2014.
- [11] T. Duan, Y. Chen, Q. Wen, and Y. Duan, "Novel composition graded Ti/Ru-Sb-SnO₂ electrode synthesized by selective electrodeposition and its application for electrocatalytic decolorization of dyes," *The Journal of Physical Chemistry C*, vol. 119, no. 14, pp. 7780–7790, 2015.
- [12] Y. Duan, Y. Chen, Q. Wen, and T. Duan, "Fabrication of dense spherical and rhombic Ti/Sb-SnO₂ electrodes with enhanced electrochemical activity by colloidal electrodeposition," *Journal of Electroanalytical Chemistry*, vol. 768, pp. 81–88, 2016.
- [13] Y. Sun, S. Cheng, Z. Mao, Z. Lin, X. Ren, and Z. Yu, "High electrochemical activity of a Ti/SnO₂-Sb electrode electrodeposited using deep eutectic solvent," *Chemosphere*, vol. 239, Article ID 124715, 2020.
- [14] W. Wu, Z.-H. Huang, and T.-T. Lim, "Enhanced electrochemical oxidation of phenol using a hydrophobic TiO₂-NTs/SnO₂-Sb-PTFE electrode prepared by pulse electrodeposition," *RSC Advances*, vol. 5, no. 41, pp. 32245–32255, 2015.
- [15] T. Wu, G. Zhao, Y. Lei, and P. Li, "Distinctive tin dioxide anode fabricated by pulse electrodeposition: high oxygen evolution potential and efficient electrochemical degradation of fluorobenzene," *The Journal of Physical Chemistry C*, vol. 115, no. 10, pp. 3888–3898, 2011.
- [16] P. Yao, X. Chen, H. Wu, and D. Wang, "Active Ti/SnO₂ anodes for pollutants oxidation prepared using chemical vapor deposition," *Surface and Coatings Technology*, vol. 202, no. 16, pp. 3850–3855, 2008.
- [17] J. I. Scott, R. F. Martinez-Gazoni, M. W. Allen, and R. J. Reeves, "Optical and electronic properties of high quality

- Sb-doped SnO₂ thin films grown by mist chemical vapor deposition,” *Journal of Applied Physics*, vol. 126, no. 13, Article ID 135702, 2019.
- [18] H. Liu, J. Chen, R. Hu et al., “Facile one-pot synthesis of self-assembled 3-D flower-like SnO₂ architectures and their electrochemical properties,” *Journal of Materials Science: Materials in Electronics*, vol. 27, no. 4, pp. 3968–3973, 2016.
- [19] J. Fan, M. Guerrero, A. Carretero-Genevri er et al., “Evaporation-induced self-assembly synthesis of Ni-doped mesoporous SnO₂ thin films with tunable room temperature magnetic properties,” *Journal of Materials Chemistry C*, vol. 5, no. 22, pp. 5517–5527, 2017.
- [20] P. Li, G. Zhao, M. Li, T. Cao, X. Cui, and D. Li, “Design and high efficient photoelectric-synergistic catalytic oxidation activity of 2D macroporous SnO₂/1D TiO₂ nanotubes,” *Applied Catalysis B: Environmental*, vol. 111, pp. 578–585, 2012.
- [21] J. Fan, G. Zhao, H. Zhao, S. Chai, and T. Cao, “Fabrication and application of mesoporous Sb-doped SnO₂ electrode with high specific surface in electrochemical degradation of ketoprofen,” *Electrochimica Acta*, vol. 94, pp. 21–29, 2013.
- [22] L. Wang, A. Palacios-Padr os, R. Kirchgeorg, A. Tighineanu, and P. Schmuki, “Enhanced photoelectrochemical water splitting efficiency of a hematite-ordered Sb:SnO₂ host-guest system,” *ChemSusChem*, vol. 7, no. 2, pp. 421–424, 2014.
- [23] V. Fauzia, M. N. Yusnidar, L. H. Lalasari, A. Subhan, and A. A. Umar, “High figure of merit transparent conducting Sb-doped SnO₂ thin films prepared via ultrasonic spray pyrolysis,” *Journal of Alloys and Compounds*, vol. 720, pp. 79–85, 2017.
- [24] Y. Bouznit and A. Henni, “Characterization of Sb doped SnO₂ films prepared by spray technique and their application to photocurrent generation,” *Materials Chemistry and Physics*, vol. 233, pp. 242–248, 2019.
- [25] A. Chen, X. Zhu, J. Xi, H. Qin, Z. Ji, and K. Zhu, “Effects of nickel doping on the preferred orientation and oxidation potential of Ti/Sb SnO₂ anodes prepared by spray pyrolysis,” *Journal of Alloys and Compounds*, vol. 684, pp. 137–142, 2016.
- [26] M. A. S anchez-Garc a, A. Maldonado, L. Casta eada, R. Silva-Gonz alez, and M. d. I. L. Olvera, “Characteristics of SnO,” *Materials Sciences and Applications*, vol. 3, no. 10, pp. 690–696, 2012.
- [27] P. Yao, “Effects of Sb doping level on the properties of Ti/SnO₂-Sb electrodes prepared using ultrasonic spray pyrolysis,” *Desalination*, vol. 267, no. 2-3, pp. 170–174, 2011.
- [28] H. Xu, Q. Zhang, W. Yan, and W. Chu, “A Composite Sb-doped SnO₂ Electrode based on the TiO₂ nanotubes prepared by hydrothermal synthesis,” *International Journal of Electrochemical Science*, vol. 6, no. 12, pp. 6639–6652, 2011.
- [29] H.-R. An, C. Kim, S.-T. Oh, and H.-J. Ahn, “Effect of sol-layers on Sb-doped SnO₂ thin films as solution-based transparent conductive oxides,” *Ceramics International*, vol. 40, no. 1, pp. 385–391, 2014.
- [30] L. Xu and Y. Lian, “A Ti/SnO₂-Sb nanorods anode for electrochemical degradation of CI Acid Red 73,” *Journal of The Electrochemical Society*, vol. 163, no. 14, p. H1144, 2016.
- [31] L. Yang, J. Liu, L. Huang et al., “Fabrication of nano-structured stacked sphere SnO₂-Sb electrode with enhanced performance using a situ solvothermal synthesis method,” *Journal of The Electrochemical Society*, vol. 165, no. 5, p. E208, 2018.
- [32] J. Montero, C. Guill en, and J. Herrero, “Nanocrystalline antimony doped tin oxide (ATO) thin films: a thermal restructuring study,” *Surface and Coatings Technology*, vol. 211, pp. 37–40, 2012.
- [33] B. Yan, A. Chen, C. Shao, and K. Zhu, “Microrod structure and properties of Sb-doped Ti/SnO₂ anodes prepared by magnetron sputtering,” *Science Bulletin*, vol. 60, no. 24, pp. 2135–2139, 2015.
- [34] T. P. Wai, Y. Yin, X. Zhang, and Z. Li, “Preparation and characterization of rare earth-doped Ti/SnO₂-Sb-Mn electrodes for the electrocatalytic performance,” *Journal of Nanomaterials*, vol. 2020, 2020.
- [35] F.-L. Zhu, Y.-S. Meng, and X.-Y. Huang, “Electro-catalytic degradation properties of Ti/SnO₂-Sb electrodes doped with different rare earths,” *Rare Metals*, vol. 35, no. 5, pp. 412–418, 2016.
- [36] L. Li, Z. Huang, X. Fan et al., “Preparation and Characterization of a Pd modified Ti/SnO₂-Sb anode and its electrochemical degradation of Ni-EDTA,” *Electrochimica Acta*, vol. 231, pp. 354–362, 2017.
- [37] S. Y. Yang, Y. S. Choo, S. Kim, S. K. Lim, J. Lee, and H. Park, “Boosting the electrocatalytic activities of SnO₂ electrodes for remediation of aqueous pollutants by doping with various metals,” *Applied Catalysis B: Environmental*, vol. 111, pp. 317–325, 2012.
- [38] R. Berenguer, J. M. Sieben, C. Quijada, and E. Morall on, “Electrocatalytic degradation of phenol on Pt- and Ru-doped Ti/SnO₂-Sb anodes in an alkaline medium,” *Applied Catalysis B: Environmental*, vol. 199, pp. 394–404, 2016.
- [39] J. Liang, C. Geng, D. Li, L. Cui, and X. Wang, “Preparation and degradation phenol characterization of Ti/SnO₂-Sb-Mo electrode doped with different contents of molybdenum,” *Journal of Materials Science & Technology*, vol. 31, no. 5, pp. 473–478, 2015.
- [40] L. Xu, Y. Sun, L. Zhang, J. Zhang, and F. Wang, “Electrochemical oxidation of CI Acid Red 73 wastewater using Ti/SnO₂-Sb electrodes modified by carbon nanotube,” *Desalination and Water Treatment*, vol. 57, no. 19, pp. 8815–8825, 2016.
- [41] L. Zhang, L. Xu, J. He, and J. Zhang, “Preparation of Ti/SnO₂-Sb electrodes modified by carbon nanotube for anodic oxidation of dye wastewater and combination with nanofiltration,” *Electrochimica Acta*, vol. 117, pp. 192–201, 2014.
- [42] L. Pahlevani, M. R. Mozdianfar, and N. Fallah, “Electrochemical oxidation treatment of offshore produced water using modified Ti/Sb-SnO₂ anode by graphene oxide,” *Journal of Water Process Engineering*, vol. 35, Article ID 101204, 2020.
- [43] X. Li, H. Xu, W. Yan, and D. Shao, “Electrocatalytic degradation of aniline by Ti/Sb-SnO₂, Ti/Sb-SnO₂/Pb₃O₄ and Ti/Sb-SnO₂/PbO₂ anodes in different electrolytes,” *Journal of Electroanalytical Chemistry*, vol. 775, pp. 43–51, 2016.
- [44] Y. Jin, Y. Lv, C. Yang et al., “Fabrication of superhydrophobic Ti/SnO₂-Sb/ α -PbO₂/Fe- β -PbO₂-PTFE electrode and application in wastewater treatment,” *Journal of Electronic Materials*, vol. 49, no. 4, pp. 2411–2418, 2020.
- [45] D. Santos, M. Pacheco, A. Gomes, A. Lopes, and L. Ciriaco, “Preparation of Ti/Pt/SnO₂-Sb₂O₄ electrodes for anodic oxidation of pharmaceutical drugs,” *Journal of Applied Electrochemistry*, vol. 43, no. 4, pp. 407–416, 2013.
- [46] Q. Bi, W. Guan, Y. Gao, Y. Cui, S. Ma, and J. Xue, “Study of the mechanisms underlying the effects of composite intermediate layers on the performance of Ti/SnO₂-Sb-La electrodes,” *Electrochimica Acta*, vol. 306, pp. 667–679, 2019.
- [47] Q. Wang, T. Jin, Z. Hu, L. Zhou, and M. Zhou, “TiO₂-NTs/SnO₂-Sb anode for efficient electrocatalytic degradation of organic pollutants: effect of TiO₂-NTs architecture,” *Separation and Purification Technology*, vol. 102, pp. 180–186, 2013.
- [48] S. Asim, J. Yin, X. Yue et al., “Controlled fabrication of hierarchically porous Ti/Sb-SnO₂ anode from honeycomb to

- network structure with high electrocatalytic activity," *Rsc Advances*, vol. 5, no. 36, pp. 28803–28813, 2015.
- [49] J. Moir, N. Soheilnia, P. O'Brien et al., "Enhanced hematite water electrolysis using a 3D antimony-doped tin oxide electrode," *ACS Nano*, vol. 7, no. 5, pp. 4261–4274, 2013.
- [50] Y. Wang, H. Duan, Z. Pei, and L. Xu, "Hydrothermal synthesis of 3D hierarchically flower-like structure Ti/SnO₂-Sb electrode with long service life and high electrocatalytic performance," *Journal of Electroanalytical Chemistry*, vol. 855, Article ID 113635, 2019.

Research Article

Corrosion Behaviors of Microarc Oxidation Coating and Anodic Oxidation on 5083 Aluminum Alloy

Haiou Sun,¹ Liangcai Li,¹ Zhongyi Wang ,¹ Bin Liu ,^{1,2} Meng Wang,¹ and Yunliang Yu¹

¹College of Power and Energy Engineering, Harbin Engineering University, Harbin, China

²Corrosion and Protection Laboratory, Key Laboratory of Superlight Materials and Surface Technology, Harbin Engineering University, Ministry of Education, Harbin, China

Correspondence should be addressed to Zhongyi Wang; b205030024@126.com and Bin Liu; liubin@hrbeu.edu.cn

Received 28 March 2020; Revised 15 October 2020; Accepted 24 October 2020; Published 21 November 2020

Academic Editor: Jian Chen

Copyright © 2020 Haiou Sun et al. This is an open access article distributed under the Creative Commons Attribution License, which permits unrestricted use, distribution, and reproduction in any medium, provided the original work is properly cited.

The microarc oxidation (MAO) coating and anodic oxidation coating were prepared on 5083 aluminum alloy. The surface morphology, elemental composition, and electrochemical behavior of the two coatings were analyzed. The results proved that the corrosion resistance of the MAO coating is superior than that of the anodic oxidation coating. The protective ability of the coating deteriorated gradually with the increase in immersion time. The corrosion process is controlled by ion diffusion throughout the coatings.

1. Introduction

The air intake filter is generally equipped in front of the gas turbine to filter out the salt sprays contained in the intake airflow, and thus, the service life of the gas turbine could be effectively guaranteed and extended [1–5]. In order to meet the requirements of high efficiency and low resistance of the air intake filter, the cyclone filter usually serves as the first stage. The cyclone filter is generally exposed to the marine atmosphere and is susceptible to corrosion due to the salt spray particles of the marine environment [6–11]. In addition, to reduce the weight and the quality control cost of the cyclone filter and its components, the cyclone filter is generally made from aluminum alloy [6, 12]. The surface coating technology is an effective and economical way to enhance the anticorrosion resistance of the aluminum alloy substrate [13]. Therefore, the surface coating technology and the degradation behaviors of the cyclone separators in corrosive environment are the necessary guarantee for the safe operation of the cyclone separators. So the research and development of the surface coating technology for aluminum alloy has important significance.

Since the 1970s, a large amount of literatures concentrated on the cyclone separators have been published.

Tabakoff and Grant [14] proposed a purely empirical formula to describe the collisional motion between the particles and the wall. Kim and Lee [15] developed a two-phase flow model to investigate the sedimentation and turbulent diffusion effects of solid particles in the boundary layer. Brouwers [16] used the numerical and experimental method to investigate the separation efficiency of the rotational axial-flow separator. Zhang et al. [17] conducted an experimental research on an axial-flow multitube cyclone separator. The results indicated that the axial-flow multitube cyclone has a higher separation efficiency and lower resistance than the tangential inlet cyclone. However, aluminum and aluminum alloys are reported to corrode mainly in the forms of pitting, intergranular corrosion (IGC), and stress corrosion cracking (SCC), when they are exposed to the solutions containing chloride ions [18–23]. Al coating, i.e., microarc oxidation (MAO) and anodic oxidation coating, can significantly improve the anticorrosion resistance of the aluminum alloys. Wang et al. [24] investigated a ceramic coating deposited on Al matrix composite by MAO and found that surface hardness wear resistance of the composite can be significantly improved. Chen et al. [25] investigated the corrosion performance of MAO coatings on different regions of the friction stirred 6061 aluminum alloy plate and found that the

corrosion protection performance of the MAO coating can be improved by inducing the coarse and congregated Al-Fe-Si particles into fine and disperse distributed particles. Krishtal [26] found that the substantial improvement in corrosion resistance of the friction stir welds of 7075 aluminum alloy can be achieved by MAO treatment. Xin et al. [27] investigated the properties of alumina coatings prepared by the MAO process using direct current (DC) and unbalanced alternative current (AC) power supplies. The results showed that the coating deposited by AC possesses higher density, hardness, and corrosion resistance. Li et al. [28] investigated the microstructure for MAO coating on the 6061 aluminum alloy in the $\text{Na}_2\text{SiO}_3\text{-CH}_3\text{COONa-Na}_5\text{P}_3\text{O}_{10}$ electrolyte system. The results showed that the size of spark was exponentially related to thickness of coating, and the structure of the coating was in a three-dimensional network. Du et al. [29] developed a black MAO coating on 2A12 aluminum alloy and found that the coating has superior adhesion and corrosion resistance. This will provide further research direction for developing MAO black coating on aluminum and aluminum alloy. Nalivaiko et al. [30] investigated the preparation of aluminum hydroxide obtained by aluminum anodic oxidation. The coating formed on high purity alumina consists of 4 stages from $\text{Al(OH)}_3\text{-NH}_4\text{Cl-H}_2\text{O}$ to $\alpha\text{-Al}_2\text{O}_3$.

In this paper, alumina coatings on 5083 aluminum alloy were prepared by MAO and anodic oxidation, respectively. The microstructure, elemental composition, and the corrosion behaviors of the two coatings were investigated. At the end, the corrosion mechanism of the two coatings was discussed in brief.

2. Experimental

The cyclone filter used in this work is made of commercial 5083 aluminum alloy. The chemical compositions of the commercial 5083 aluminum alloy are shown in Table 1. Prior to the experiments, the specimen was cut in pieces with dimensions of $60 \times 55 \times 3$ mm. The geometrical schematic diagram of the cyclone filter is shown in Figure 1.

Microarc oxidation and anodic oxidation techniques were used to prepare the coatings surface on the experimental samples of the cyclone filter, and the surface sealing treatment of the microarc oxidation coating was performed with 5% saline solution. Samples of the cyclone filter with the microarc oxidation treatment and the anodic oxidation treatment are shown in Figure 2.

The electrochemical response of MAO coating, anodic oxidation coating, and 5083 aluminum alloy was obtained using IM6/IM6e electrochemical workstation (ZAHNER, Germany) in 3.5 wt.% NaCl solution. A classic three-electrode system is used, which composed of a saturated Ag/AgCl reference electrode, a platinum sheet with dimensions of $20 \times 20 \times 0.1$ mm, and 5083 aluminum alloy and coatings as a working electrode [31]. The potentiodynamic polarization curves were conducted by sweeping the potential from $-0.6 \text{ V}/_{\text{Ag/AgCl}}$ below open circuit potential (OCP) with a scanning rate of 0.333 mV/s . The electrochemical impedance spectroscopy (EIS) tests were

TABLE 1: Chemical compositions of the 5083 aluminum alloy (wt.%).

Cu	Si	Mg	Zn	Fe	Cr	Ti	Mn	Al
0.09	0.31	4.1	0.21	0.35	0.05	0.05	0.47	Bal.

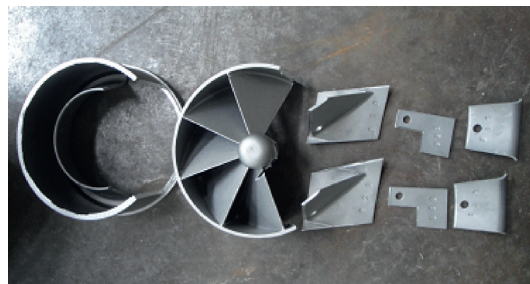


FIGURE 1: Test trial sample of cyclone separator.

performed at OCP with a sinusoidal potential perturbation of 10 mV in a frequency range from 10 kHz to 10 mHz. The tested solution was maintained at $25 \pm 1^\circ\text{C}$ in the air without stirring.

The salt spray test for MAO and anodic oxidation coating on 5083 aluminum alloy was conducted using machine DJS-EN61 according to the ISO 14993:2001 standard. The solution is 5 wt.% NaCl solution, pH of salt solution is 6.8, the temperature of the salt solution barrel is 35°C , and the sample place angle is 25° . The examination of the specimen was performed after 63 days of experiment. After the test, the samples were cleaned by flow water of temperature not higher than 35°C to remove the sample surface residual salt spray solution and then dried using hot air.

3. Result and Discussion

3.1. Surface Characterization of the Two Different Coatings. Figure 3 shows the surface morphologies of the MAO coating on 5083 aluminum alloy samples, revealing volcano-like morphologies with micropores of various sizes that can be observed on the surface. As is seen from Figure 3, the micropores are smaller in size with diameters of $2 \mu\text{m}$ and distributed uniformly. This is the characteristic of MAO coatings obtained by microsparks on the sample surface of alloys [25, 32]. Still some of the pores in the MAO are blocked. In Figure 3, the number of small white particles identified by EDS is Fe-rich particles. This is consistent with the finding of Chen [25]. In addition, no crack exists in Figure 3, which indicates that the MAO coating is very adhesive to 5083 aluminum alloy substrate [33].

The surface morphologies of anodic oxidation coating formed on 5083 aluminum alloy are shown in Figure 4. The anodic oxidation coating surface looks very dense, but there are a lot of cracks staggered on the surface. It could be seen that numerous wrinkles and cracks staggered on the surface. So, the corrosion properties would deteriorate due to these cracks.

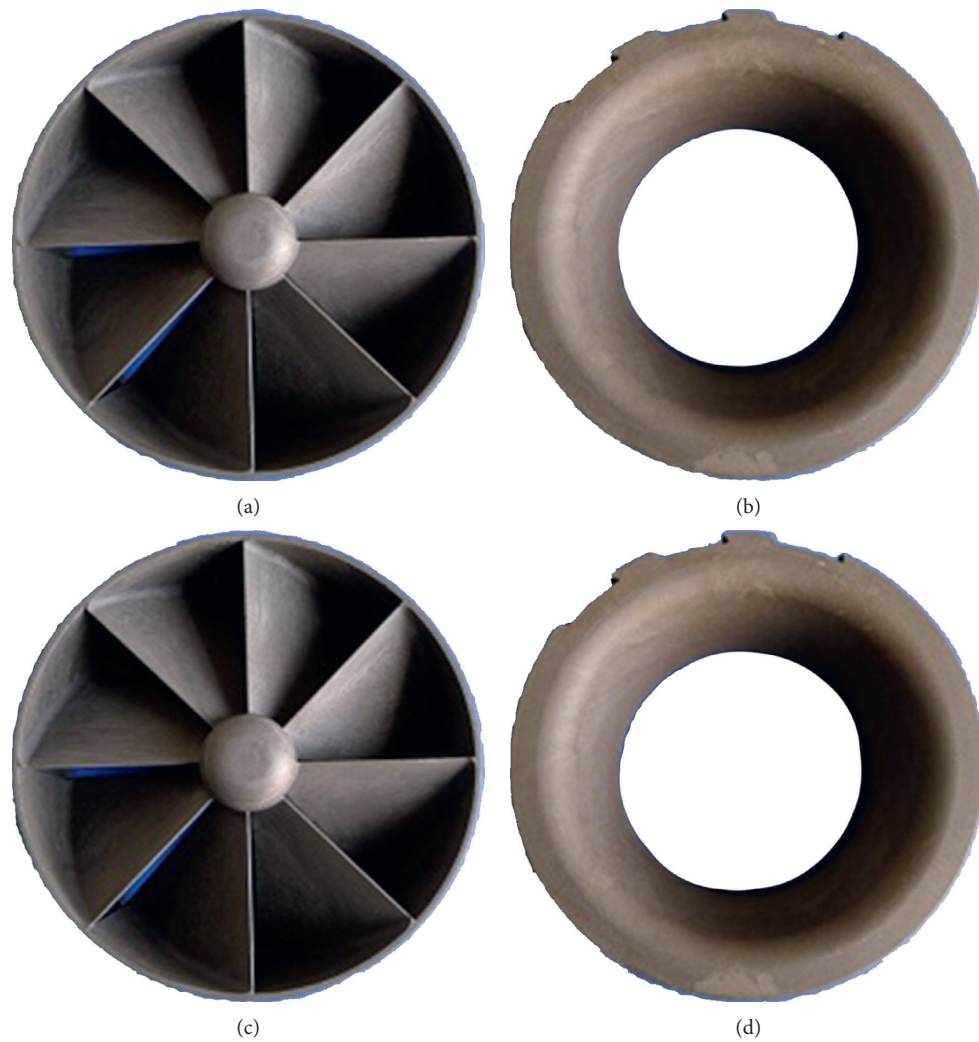


FIGURE 2: Marine cyclone separator structure sample by MAO and anodic oxidation: (a) MAO forward view; (b) MAO backward view; (c) anodic oxidation forward view; (d) anodic oxidation backward view.

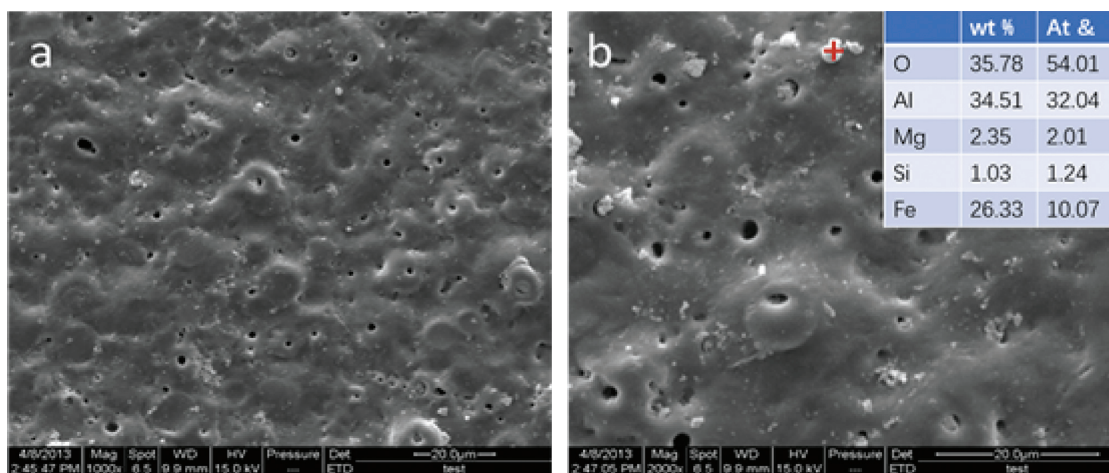


FIGURE 3: Surface morphologies of the MAO coatings.

3.2. *Potentiodynamic Polarization Curves.* The potentiodynamic polarization curves for MAO coating, anodic oxidation coating, and 5083 aluminum alloy in 3.5 wt.% NaCl

solution are shown in Figure 5. The curves indicated that the MAO coating and anodic oxidation coatings lead to the changes in the anodic current, pitting potential (E_{pit}), and

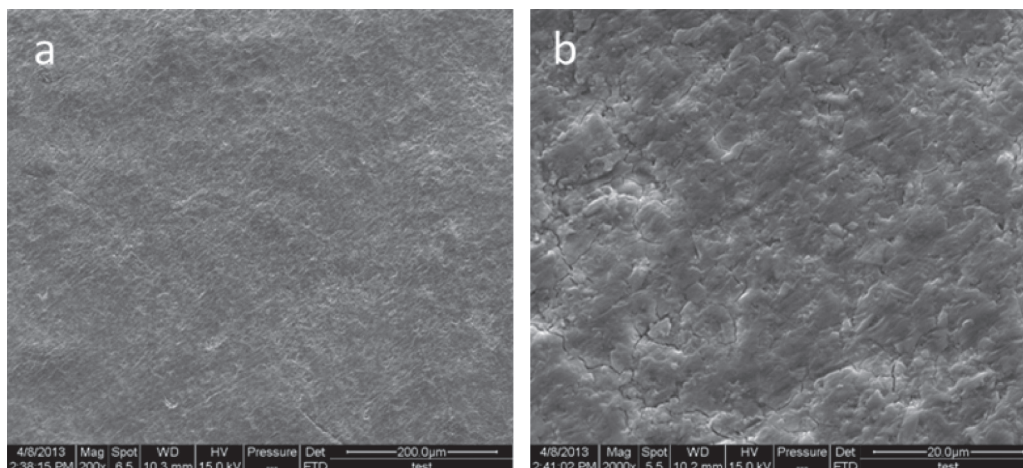


FIGURE 4: Surface morphologies of anodic oxidation coating.

corrosion rate. The potentiodynamic polarization curves indicated that the corrosion resistance of the MAO and anodic oxidation coatings can be significantly improved compared to the 5083 aluminum alloy matrix. It was obvious that MAO coating and anodic oxidation coating led to the positive shift in corrosion potential.

The corrosion potential (E_{corr}) of the 5083 aluminum alloy, anodic coating, and MAO coating is -694 ± 8 , -636 ± 12 , and -385 ± 11 mV/Ag/AgCl. Compared with the 5083 aluminum alloy, the corrosion potentials shifted nobly for the MAO and anodic oxidation coatings. The corrosion current density (i_{corr}) value of the 5083 aluminum alloy, anodic coating, and MAO coating is $3.33 \pm 0.11 \times 10^{-6}$, $7.33 \pm 0.24 \times 10^{-7}$, and $1.07 \pm 0.18 \times 10^{-9}$ A/cm², respectively. This suggests that the corrosion resistance for MAO coating is two orders higher than that for 5083 aluminum alloy. This indicates that both of the MAO and anodic oxidation coatings can reduce the corrosion rate of the 5083 aluminum alloy specimens in 3.5 wt.% NaCl solution [34–36].

3.3. Electrochemical Impedance Spectroscopy

3.3.1. MAO Coating. The Bode (Figure 6(a)) and Nyquist (Figure 6(b)) plots for MAO coating on 5083 aluminum alloy after immersion in 3.5 wt.% NaCl solution for 1 day are presented in Figure 6. The Nyquist plots exhibit two capacitive semicircles, suggesting the inductive behavior [34, 37]. Figure 7 presents the equivalent circuit used to simulate the EIS data, in which R_s is the resistance of the 3.5 wt.% NaCl solution and C_{dl} and R_{dl} are the capacitance and resistance of the adsorption layer, respectively. CPE and R_p are the capacitance and polarization resistance of the MAO coating, respectively. The use of a constant phase element (CPE) was used in place of capacitance because of the distribution of relaxation times resulting from heterogeneities at the electrode surface [31, 33, 38, 39]. The fitted parameters in the equivalent circuit in Figure 7 are given in Table 2.

The Bode (Figure 8(a)) and Nyquist (Figure 8(b)) plots for MAO coating on 5083 aluminum alloy after immersion

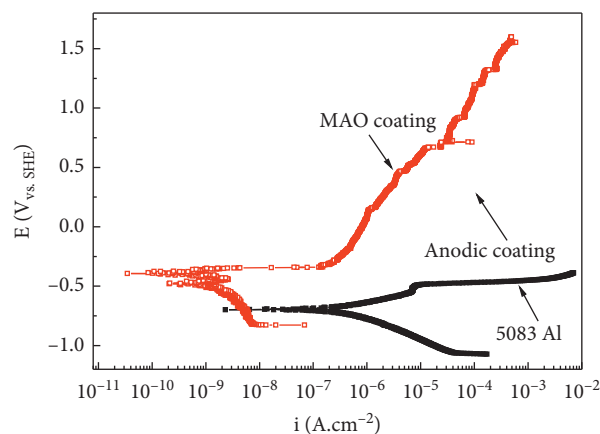


FIGURE 5: Potentiodynamic polarization curves for MAO coating, anodic oxidation coating, and 5083 aluminum alloy in 3.5 wt.% NaCl solution.

in 3.5 wt.% NaCl solution for 12 days are presented in Figure 8. The Nyquist plots exhibit a capacitive semicircle in high-frequency region and an inductive loop in low-frequency region [19]. The capacitive reactance arc corresponds to the process of ions passing through the MAO coating, and the inductive arc corresponds to the desorption process of the adsorbed intermediate products [40–42]. Figure 9 presents the equivalent circuit used to simulate the EIS data, in which CPE_f is the capacitance of the MAO coating, R_{pore} is the resistance of defects, C_{dl} is the double layer capacitance, R_p is the polarization resistance, L is the inductive resistance, and R_L is the inductive resistance, which is related to the active dissolution of MAO coating [43]. The fitted parameters in the equivalent circuit in Figure 9 are given in Table 3.

The Bode (a) and Nyquist (b) plots for MAO or 32 and 63 days are presented in Figure 10. The Nyquist plots exhibit a capacitive semicircle and a bias line at low-frequency region. The capacitive reactance arc corresponds to the process of ions passing through the MAO coating [43]. The bias line at low frequency corresponds to the diffusion process of Cl^-

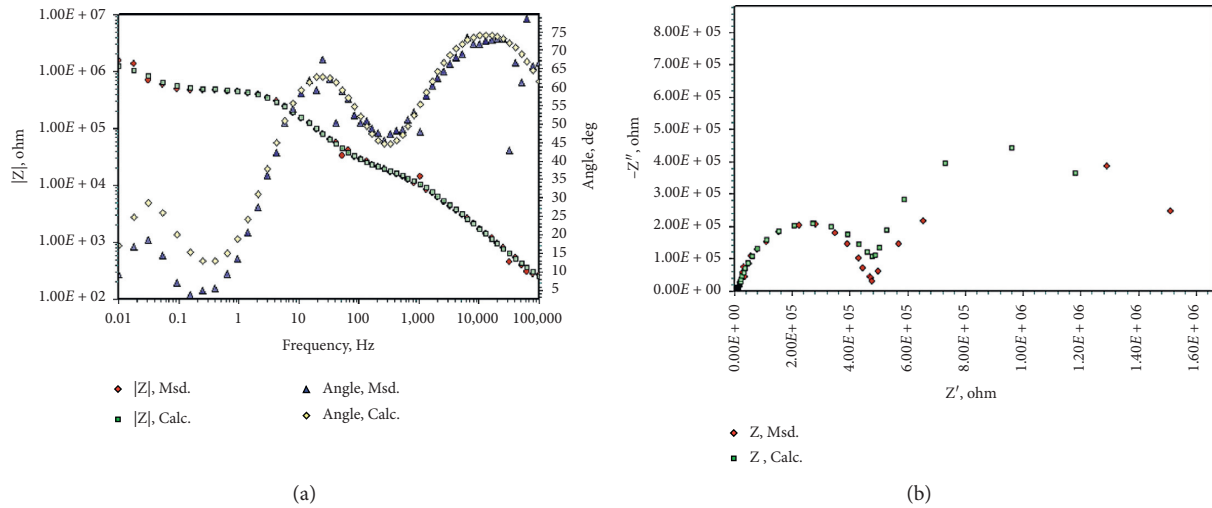


FIGURE 6: (a) Bode and (b) Nyquist curves of MAO coating after being immersed in 3.5 wt.% NaCl solution for 1 day.

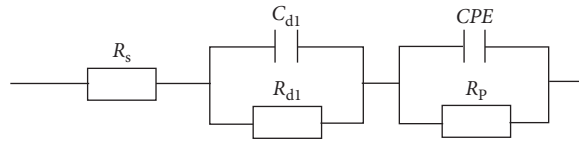


FIGURE 7: The equivalent circuit used to evaluate the EIS data presented in Figure 8.

TABLE 2: Fitting results of the equivalent circuit obtained by fitting the EIS data.

R_s ($\Omega \cdot \text{cm}^{-2}$)	R_{d1} ($\Omega \cdot \text{cm}^{-2}$)	C_{d1} ($\text{F} \cdot \text{cm}^{-2}$)	Y_0 ($\Omega^{-1} \text{s}^n \text{cm}^{-2}$)	n	R_p ($\Omega \cdot \text{cm}^{-2}$)
3.14	4.28×10^4	1.37×10^{-5}	2.91×10^{-5}	0.85	7.16×10^5

Note: Y_0 : CPE constant; n : CPE exponent.

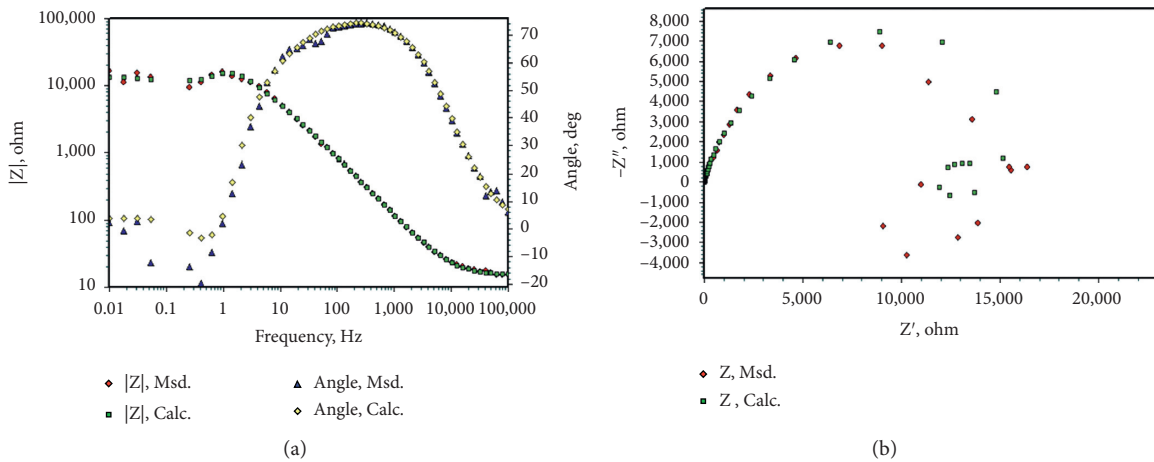


FIGURE 8: (a) Bode and (b) Nyquist curves of MAO coating after being immersed in 3.5 wt.% NaCl solution for 12 days.

through the MAO coating [44]. Figure 11 presents the equivalent circuit used to simulate the EIS data, in which W is the Warburg impedance. W was used to fit the data of MAO coating suggesting the responses induced by diffusion in paths of semi-infinite length [43, 44]. The fitted

parameters in the equivalent circuit in Figure 11 are given in Table 4.

From the EIS response, it can be inferred that three stages for MAO coating during the immersion time can be identified. In the first stage, the equivalent circuit in Figure 7

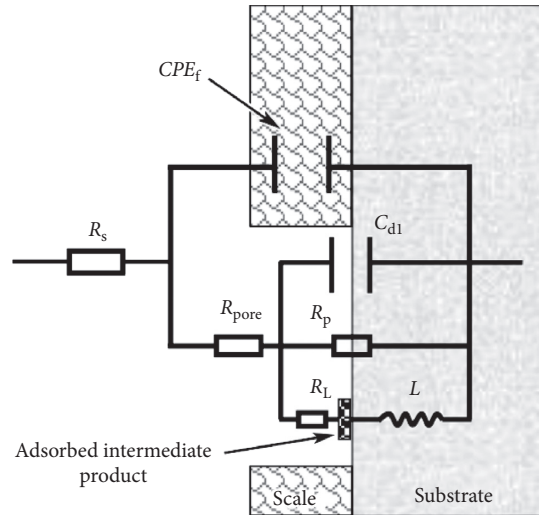


FIGURE 9: Equivalent circuit used to evaluate the EIS data presented in Figure 10 (Figure 9 is reproduced from [42] under the Creative Commons Attribution License/public domain).

TABLE 3: Fitting results of the equivalent circuit obtained by fitting the EIS data.

R_s ($\Omega \cdot \text{cm}^{-2}$)	Y_0 ($\Omega^{-1} \cdot \text{s}^n \cdot \text{cm}^{-2}$)	n	R_{pore} ($\Omega \cdot \text{cm}^{-2}$)	C_{dl} ($\text{F} \cdot \text{cm}^{-2}$)	R_p ($\Omega \cdot \text{cm}^{-2}$)	L ($\text{H} \cdot \text{cm}^{-2}$)	R_L ($\Omega \cdot \text{cm}^{-2}$)
7.42	5.19×10^{-4}	0.89	5.18×10^2	4.57×10^{-5}	7.21×10^5	3.21×10^2	4.50×10^4

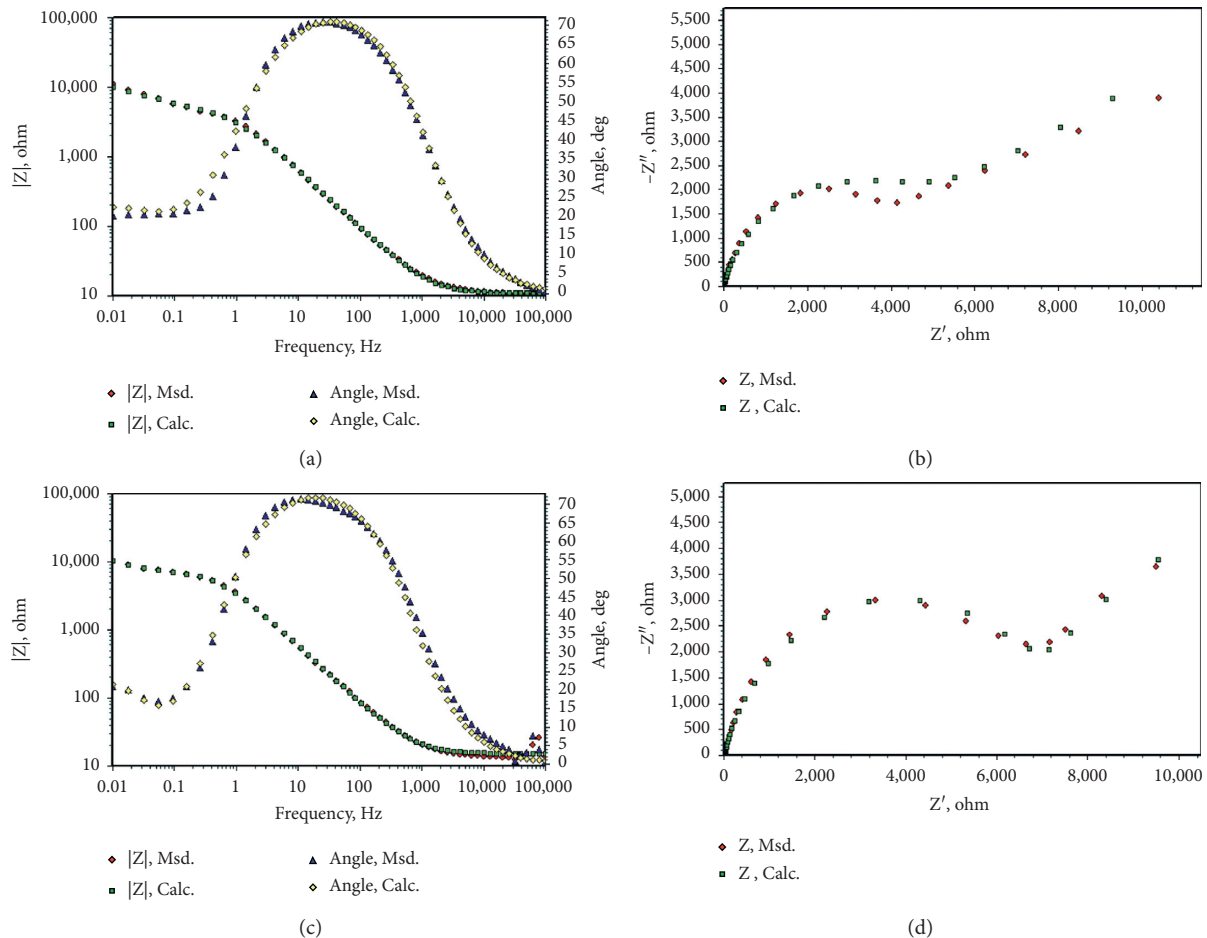


FIGURE 10: (a) Bode and (b) Nyquist curves of MAO coating after being immersed in 3.5 wt.% NaCl solution for 32 and 63 days.

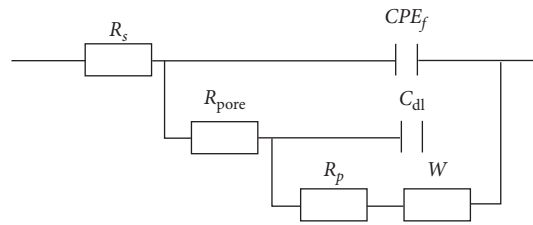
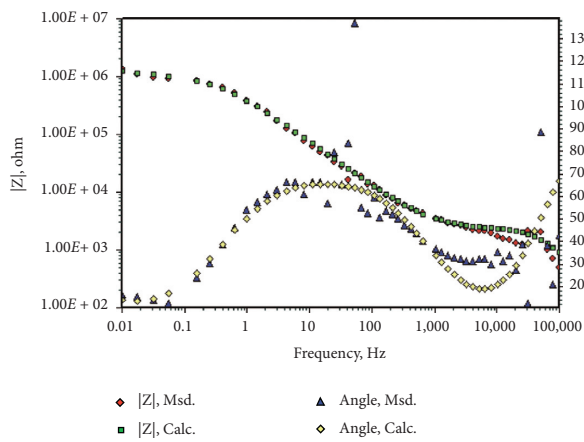


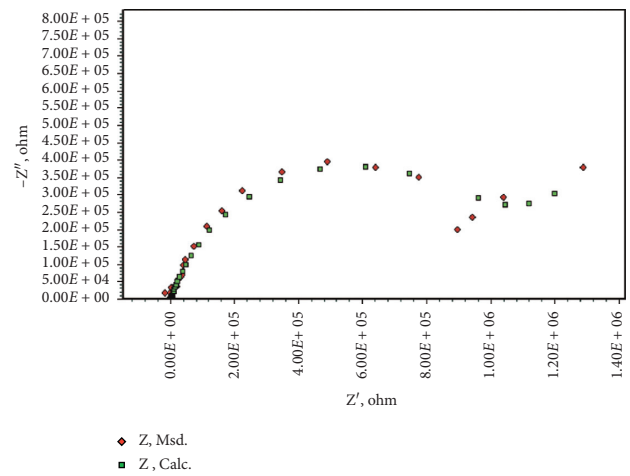
FIGURE 11: Equivalent circuit used to evaluate the EIS data presented in Figure 10.

TABLE 4: Fitting results of the equivalent circuit obtained by fitting the EIS data.

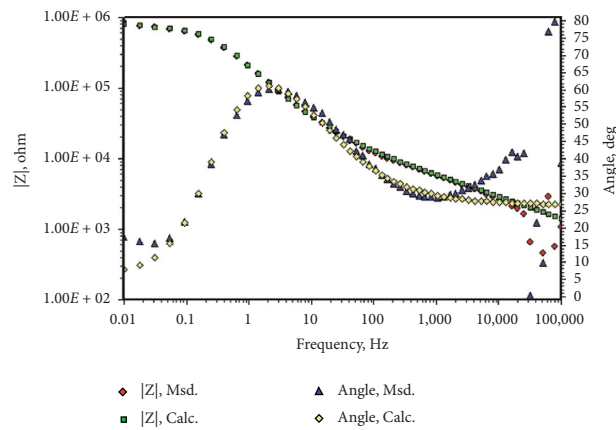
R_s ($\Omega \cdot \text{cm}^{-2}$)	Y_0 ($\Omega^{-1} \cdot \text{s}^n \cdot \text{cm}^{-2}$)	N	R_{pore} ($\Omega \cdot \text{cm}^{-2}$)	C_{dl} ($\text{F} \cdot \text{cm}^{-2}$)	R_p ($\Omega \cdot \text{cm}^{-2}$)	W ($\text{s}^{-0.5} \Omega \cdot \text{cm}^{-2}$)
6.13	2.16×10^{-5}	0.85	1.78×10^3	1.57×10^{-5}	7.16×10^5	3.21×10^{-2}



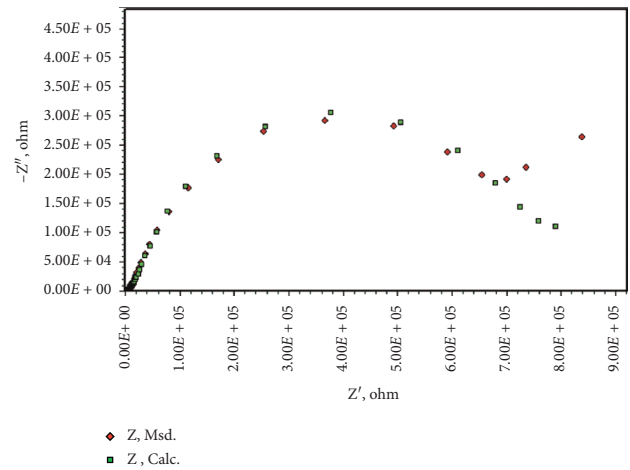
(a)



(b)



(c)



(d)

FIGURE 12: Continued.

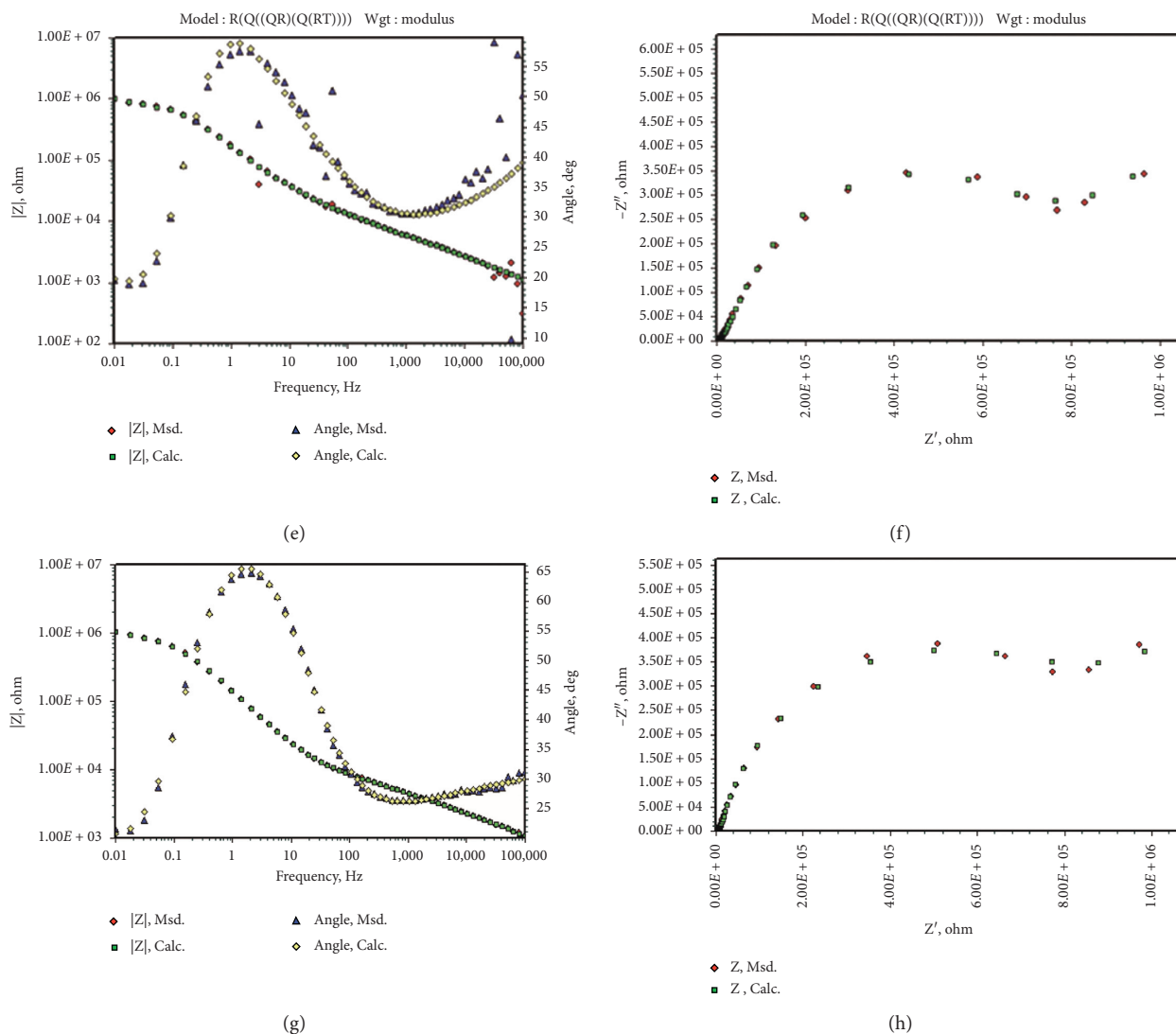


FIGURE 12: Bode and Nyquist curves of anodic oxidation coating after being immersed in 3.5 wt.% NaCl solution for (a, b) 1 day, (c, d) 12 days, (e, f) 32 days, and (g, h) 63 days.

indicates that the MAO has superior corrosion protection ability. In the second stage, identifying at increasing immersion time, the EIS presents desorption characteristics at low frequencies connecting to a capacitive semicircle at high frequencies (Figure 9). In this stage, local pitting corrosion in the MAO coating takes place stimulating Al matrix dissolution through corrosion pits [45]. After long immersion time, the chloride effectively induces local breakdown of the MAO coating, which is in agreement with the reported findings in the literature. The chloride ion may penetrate through the MAO coating and reach matrix/coating interface. As a result, an additional Warburg impedance at low frequency is employed.

3.3.2. Anodic Oxidation Coating. The EIS plots for anodic oxidation coating on 5083 aluminum alloy after immersion in 3.5 wt.% NaCl solution for 1, 12, 32, and 63 days are

presented in Figure 12. The Warburg impedance in Figure 11 is due to the existence of cracks (Figure 3(b)), which can act as the diffusion path for the corrosive ions. The equivalent circuit used to interpret the EIS data is shown in Figure 12. The fitted parameters obtained are given in Table 5. As is seen from Table 5, the value of R_p decreased with the increase in immersion time. It indicated that the protective performance of the anodic oxidation coating on 5083 aluminum alloy surface deteriorated and the risk of corrosion increased [45, 46].

3.4. Salt Spray Test. Figure 13 shows the surface morphologies of the two different coatings on 5083 aluminum alloy after the salt spray test for 63 days. The breakdown of the both coatings is not visible observed. As is seen from Figure 13, there are almost no signs of corrosion on the surface of MAO coating. However, there was slight corrosion on

TABLE 5: Fitting results of the equivalent circuit obtained by fitting the EIS data.

Time (days)	R_s ($\Omega\cdot\text{cm}^{-2}$)	Y_0 ($\Omega^{-1}\cdot\text{s}^n\cdot\text{cm}^{-2}$)	n	R_{pore} ($\Omega\cdot\text{cm}^{-2}$)	C_{dl} ($\text{F}\cdot\text{cm}^{-2}$)	R_p ($\Omega\cdot\text{cm}^{-2}$)	W ($\text{s}^{-0.5}\Omega\cdot\text{cm}^{-2}$)
1	4.32	7.57×10^{-5}	0.94	4.38×10^2	1.57×10^{-5}	9.81×10^5	3.89×10^{-2}
12	5.61	6.42×10^{-5}	0.92	4.05×10^2	2.44×10^{-5}	7.65×10^5	4.77×10^{-2}
32	6.35	7.70×10^{-5}	0.91	3.89×10^2	1.84×10^{-5}	7.03×10^5	6.25×10^{-2}
63	4.28	6.82×10^{-5}	0.89	3.45×10^2	2.06×10^{-5}	6.41×10^5	7.03×10^{-2}

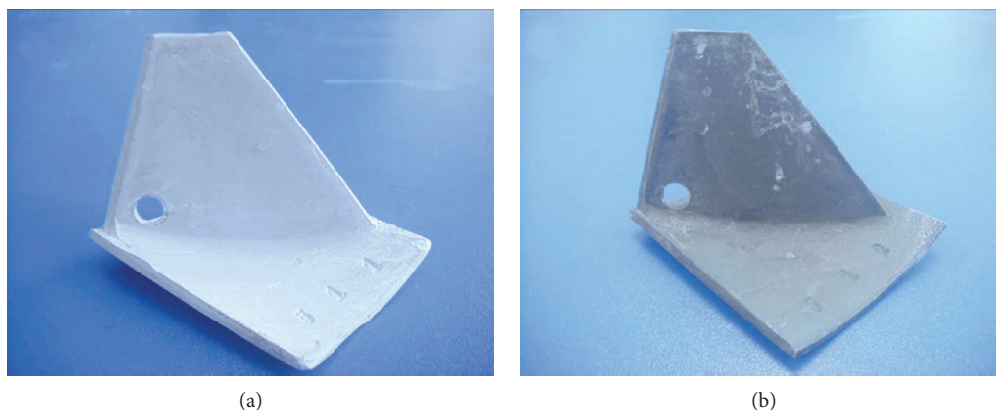


FIGURE 13: Surface morphology of the (a) MAO coating and (b) anodic oxidation coating after the salt spray test.

anodic oxidation coating. This is in good agreement with the electrochemical measurement.

4. Conclusions

The protective performance of the MAO is superior than that of the anodic oxidation coating. The 5083 aluminum alloy with MAO coating showed a good corrosion resistance at the initial stage. With the increase in immersion time, the pitting corrosion occurs in the MAO coating, and the protective ability of the coating deteriorated gradually. In contrast, the existence of the cracks in anodic oxidation coating can act as the diffusion path for the corrosive ions. The corrosion process is controlled by ion diffusion throughout the coatings.

Data Availability

The data used to support the findings of this study are available from the corresponding author upon request.

Conflicts of Interest

The authors declare that they have no conflicts of interest.

Acknowledgments

This research was funded by the National Natural Science Foundation of China (nos. 51679051 and 51701050), the Outstanding Youth Foundation of Heilongjiang Province

(YQ2019E015), and the National Science and Technology Major Project (2017-V-0002-0051).

References

- [1] X. Z. Xie, "Air inlet treatment quality to influencing on the gas turbine," *Turbine Technology*, vol. 3, pp. 226–229, 2007.
- [2] R. Kurz and K. Brun, "Degradation in gas turbine systems," in *Proceedings of the ASME Turbo Expo 2000: Power for Land, Sea, and Air*, Munich, Germany, May 2000.
- [3] S. C. Fu, G. G. Sun, and C. Z. Gao, "Research and application status of guide vanes uniflow cyclone," *Journal of Filtration & Separation*, vol. 18, no. 2, pp. 11–14, 2008.
- [4] L. Shuyan, L. Ying, L. Fuqing, H. Hongbin, and Y. Weige, "Experimental research on the filtering efficiency for a new style of air filter," *Journal of Beijing Institute of Technology*, vol. 19, no. 2, pp. 171–175, 2000.
- [5] J. P. Vander Walt and A. Nurick, "Erosion of dust-filtered helicopter turbine engine Part I: basic theoretical consideration," *Journal of Aircraft*, vol. 32, no. 1, pp. 105–111, 1995.
- [6] Z. Liu, Z. Xu, and C. Zhang, "A study of the corrosion-resistant characteristics of the blades of a compressor and their protective coatings," *Journal Of Engineering for Thermal Energy and Power*, vol. 22, no. 5, pp. 490–494, 2007.
- [7] W. J. Huo and H. G. Sun, "Corrosion and precaution for blades of aero-engine compressor in the navy air arm," *Aviation Engineering & Maintenance*, vol. 6, pp. 39–41, 2002.
- [8] H. O. Sun, H. T. Zheng, and S. L. Liu, "Numerical simulation of resistance characteristics of multilayer gauze stage in moisture separator," *Journal of Harbin Engineering University*, vol. 21, no. 8, pp. 10–12, 2000.

- [9] T. Zong, D. M. Hu, and J. Li, "Numerical simulation of cyclonic separator in circulating fluidized bed boiler with CFD," *Journal of Shanghai University of Electric Power*, vol. 3, 2011.
- [10] A. P. Tarabine, V. A. Schurovasky, A. I. Bodrov, and J.-P. Stalder, "An analysis of axial compressor fouling and a cleaning method of their blading," in *Proceedings of the ASME 1996 International Gas Turbine and Aeroengine Congress and Exhibition*, Birmingham, UK, June 1996.
- [11] W. D. Griffiths and F. Boysan, "Computational fluid dynamics (CFD) and empirical modelling of the performance of a number of cyclone samplers," *Journal of Aerosol Science*, vol. 27, no. 2, pp. 281–304, 1996.
- [12] Z. Xu, "The coating preparation of turbine compressor vane in the ship and the research of anti-corrosion and wear-resistant properties," Master's thesis, Harbin Engineering University, Harbin, China, 2006.
- [13] Z.-P. Shi, Z.-B. Wang, J.-Q. Wang et al., "Effect of Ni interlayer on cavitation erosion resistance of NiTi cladding by tungsten inert gas (TIG) surfacing process," *Acta Metallurgica Sinica (English Letters)*, vol. 33, no. 3, pp. 415–424, 2020.
- [14] G. Grant and W. Tabakoff, "Erosion prediction in turbo machinery from environmental solid articles," *Journal of Aircraft*, vol. 12, pp. 471–478, 1975.
- [15] W. S. Kim and J. W. Lee, "Collection efficiency model based on boundary-layer characteristics for cyclones," *AIChE Journal*, vol. 43, no. 10, pp. 2446–2455, 1997.
- [16] J. J. H. Brouwers, "Particle collection efficiency of the rotational particle separator," *Powder Technology*, vol. 92, no. 2, pp. 89–99, 1997.
- [17] Y. Z. Zhang, H. G. Hu, and Z. Y. Liu, "Experimental research on the axial multi-stage cyclone separator," *Industrial Boiler*, vol. 4, 1997.
- [18] M. Esmaily, N. Mortazavi, W. Osikowicz et al., "Corrosion behaviour of friction stir-welded AA6005-T6 using a bobbin tool," *Corrosion Science*, vol. 111, pp. 98–109, 2016.
- [19] Y. X. Qiao, Y. Zhou, S. J. Chen, and Q. N. Song, "Effect of bobbin tool friction stir welding on microstructure and corrosion behavior of 6061-T6 aluminum alloy joint in 3.5% NaCl solution," *Acta Metallurgica Sinica*, vol. 52, no. 11, pp. 1395–1402, 2016.
- [20] L. Lokas and V. Alar, "The effect of temperature on corrosion behavior of AA5083 in brackish water and seawater," *Materials and Corrosion*, vol. 70, no. 10, pp. 1817–1825, 2019.
- [21] K. A. Yasakau, M. L. Zheludkevich, S. V. Lamaka, and M. G. S. Ferreira, "Role of intermetallic phases in localized corrosion of AA5083," *Electrochimica Acta*, vol. 52, no. 27, pp. 7651–7659, 2007.
- [22] Z. Peng, Q. Pan, S. Cai, J. Li, and W. Liang, "Effect of different aging processes on the corrosion behavior of new Al-Cu-Li-Zr-Sc alloys," *Materials and Corrosion*, vol. 70, no. 12, pp. 2266–2277, 2019.
- [23] F. Sun, X. Li, L. Lu, X. Cheng, C. Dong, and J. Gao, "Corrosion behavior of 5052 and 6061 aluminum alloys in deep ocean environment of south China sea," *Acta Metallurgica Sinica*, vol. 49, no. 10, pp. 1219–1226, 2013.
- [24] Y. K. Wang, L. Sheng, R. Z. Xiong, and B. S. Li, "Study of ceramic coatings formed by microarc oxidation on Al matrix composite surface," *Surface Engineering*, vol. 15, no. 2, pp. 112–114, 1999.
- [25] M.-A. Chen, Y.-C. Ou, Y.-H. Fu, Z.-H. Li, J.-M. Li, and S.-D. Liu, "Effect of friction stirred Al-Fe-Si particles in 6061 aluminum alloy on structure and corrosion performance of MAO coating," *Surface and Coatings Technology*, vol. 304, pp. 85–97, 2016.
- [26] M. M. Krishtal, "Effect of structure of Aluminum-Silicon alloys on the process of formation and characteristics of oxide layer in microarc oxidizing," *Metal Science and Heat Treatment*, vol. 46, no. 9, pp. 378–384, 2004.
- [27] S. Xin, L. Song, R. Zhao, and X. Hu, "Influence of cathodic current on composition, structure and properties of Al₂O₃ coatings on aluminum alloy prepared by micro-arc oxidation process," *Thin Solid Films*, vol. 515, no. 1, pp. 326–332, 2006.
- [28] X. Y. Li, X. G. Li, Y. Li et al., "Growth mechanism of micro-arc oxidation film on 6061 aluminum alloy," *Materials Research Express*, vol. 6, no. 6, Article ID 066404, 2019.
- [29] C. Du, H. Zhao, Z. Dai, Z. Tian, J. Wang, and Z. Wang, "The preparation and properties of black coating by micro arc oxidation on 2A12 aluminum alloy," *Materials Letters*, vol. 236, pp. 723–726, 2019.
- [30] A. Y. Nalivaiko, D. Y. Ozherelkov, V. I. Pak, S. S. Kirov, A. N. Arnautov, and A. A. Gromov, "Preparation of aluminum hydroxide during the synthesis of high purity alumina via aluminum anodic oxidation," *Metallurgical and Materials Transactions B*, vol. 51, no. 3, pp. 1154–1161, 2020.
- [31] Z. B. Wang, H. X. Hu, Y. G. Zheng, W. Ke, and Y. X. Qiao, "Comparison of the corrosion behavior of pure titanium and its alloys in fluoride-containing sulfuric acid," *Corrosion Science*, vol. 103, pp. 50–65, 2016.
- [32] R. F. Zhang, W. H. Chang, L. F. Jiang et al., "Formation of microcracks during micro-arc oxidation in a phytic acid-containing solution on two-phase AZ91HP," *Journal of Materials Engineering and Performance*, vol. 25, no. 4, pp. 1304–1316, 2016.
- [33] Y. X. Qiao, J. Huang, D. Huang et al., "Effects of laser scanning speed on microstructure, microhardness and corrosion behavior of laser cladding Ni45 coatings," *Journal of Chemistry*, vol. 2020, p. 11, Article ID 1438473, 2020.
- [34] L. M. Zhang, M. C. Yan, S. D. Zhang et al., "Significantly enhanced resistance to SRB corrosion via Fe-based amorphous coating designed with high dose corrosion-resistant and antibacterial elements," *Corrosion Science*, vol. 164, p. 9, Article ID 108305, 2020.
- [35] S. Hong, Y. Wu, J. Wu et al., "Microstructure and cavitation erosion behavior of HVOF sprayed ceramic-metal composite coatings for application in hydro-turbines," *Renewable Energy*, vol. 164, pp. 1089–1099, 2021.
- [36] Y. X. Qiao, Z. H. Tian, X. Cai et al., "Cavitation erosion behaviors of a nickel-free high-nitrogen stainless steel," *Tribology Letters*, vol. 67, no. 1, pp. 1–9, 2019.
- [37] A. Carnot, I. Frateur, S. Zanna, B. Tribollet, I. Dubois-Brugger, and P. Marcus, "Corrosion mechanisms of steel concrete moulds in contact with a demoulding agent studied by EIS and XPS," *Corrosion Science*, vol. 45, no. 11, pp. 2513–2524, 2003.
- [38] C. Jeyaprabha, S. Sathiyarayanan, and G. Venkatachari, "Influence of halide ions on the adsorption of diphenylamine on iron in 0.5M H₂SO₄ solutions," *Electrochimica Acta*, vol. 51, no. 19, pp. 4080–4088, 2006.
- [39] Y. Qiao, D. Xu, S. Wang et al., "Effect of hydrogen charging on microstructural evolution and corrosion behavior of Ti-4Al-2V-1Mo-1Fe alloy," *Journal of Materials Science & Technology*, vol. 60, pp. 168–176, 2021.
- [40] C. F. Chen, M. X. Lu, G. X. Zhao, Z. Q. Bai, M. L. Yan, and Y. Q. Yang, "Effects of temperature, Cl concentration and Cr on electrode reactions of CO₂ N80 steel," *Acta Metallurgica Sinica*, vol. 39, no. 8, pp. 848–854, 2003.
- [41] M. Keddad, O. R. Mottos, and H. Takenouti, "Reaction model for iron dissolution studied by electrode impedance: I .

- experimental results and reaction model,” *Journal of The Electrochemical Society*, vol. 128, no. 2, pp. 257–266, 1981.
- [42] Y. D. Li, Q. Li, X. Tang, and Y. Li, “Reconstruction and characterization of galvanic corrosion behavior of X80 pipeline steel welded joints,” *Acta Metallurgica Sinica*, vol. 55, no. 6, pp. 801–810, 2019.
- [43] L. Calabrese, A. Capri, F. Fabiano, L. Bonaccorsi, C. Borsellino, and E. Proverbio, “Electrochemical behaviour in synthetic saliva of silane coated Ni/Cu/Ni Nd-Fe-B magnet for dentistry applications,” *Materials and Corrosion*, vol. 67, no. 5, pp. 484–494, 2016.
- [44] P. Salehikahrizangi, K. Raeissi, F. Karimzadeh, L. Calabrese, S. Patane, and E. Proverbio, “Erosion-corrosion behavior of highly hydrophobic hierarchical nickel coatings,” *Colloids and Surfaces A: Physicochemical and Engineering Aspects*, vol. 558, pp. 446–454, 2018.
- [45] S. Mao, H. Yang, Z. Song, J. Li, H. Ying, and K. Sun, “Corrosion behaviour of sintered NdFeB deposited with an aluminium coating,” *Corrosion Science*, vol. 53, no. 5, pp. 1887–1894, 2011.
- [46] S. Cui, J. Han, Y. Du, and W. Li, “Corrosion resistance and wear resistance of plasma electrolytic oxidation coatings on metal matrix composites,” *Surface and Coatings Technology*, vol. 201, no. 9-11, pp. 5306–5309, 2007.

Research Article

Preparation of Microfiber Grating for Real-Time Sensing of *Escherichia Coli* Concentration

Qingyan Qiu, Min Dai , Caidong Luo, Ying Mu, Wei Du, Yu Li, Jun Luo, and Rong Li

Mianyang Center Hospital, Mianyang 621000, China

Correspondence should be addressed to Min Dai; heatedspring@sohu.com

Received 6 May 2020; Revised 3 August 2020; Accepted 9 November 2020; Published 21 November 2020

Academic Editor: Yuxin Wang; ywan943@163.com

Copyright © 2020 Qingyan Qiu et al. This is an open access article distributed under the Creative Commons Attribution License, which permits unrestricted use, distribution, and reproduction in any medium, provided the original work is properly cited.

Various diseases are spread by means of contaminated water or food, and the detection of pathogenic bacteria has great significance for securing a proper healthy environment for human beings. In this article, microfiber gratings (MFGs) were fabricated by using a high-frequency CO₂ laser. The number of periods is 30, and the length of the period is 600 μm. A type of biosensor is proposed in this study. Results showed that the biosensor was strongly sensitive to the concentration of *Escherichia coli* and a maximum sensitivity of 1.15 nm/107 CFU was achieved. The mechanism of real-time sensing of prepared MFG was also proposed, which could be due to relationship between dip wavelength shift and the concentration of detected bacteria. The prepared MFGs do not need any coating, and the proposed biosensor has a great potential for application in fields of medical treatment, biology, and farming.

1. Introduction

For several decades, detection of pathogenic bacteria has great significance in securing a proper healthy environment for human beings due to various diseases spread through contaminated water or food. *Escherichia coli* (*E. coli*) is an easy indicator for fecal coliform contamination [1]. The nonpathogenic population of *E. coli* mainly inhabits in the intestinal tract of most mammalian species including humans [2], which often causes severe intestinal and extraintestinal diseases in areas such as bloodstream, the urinary tract, and meninges [3–5]. Various techniques are developed for the detection of *E. coli* including culture methods, fluorescence, and microscopy [6]. However, most of the traditional detection methods are time-consuming and may take up to a whole week, resulting in a limitation to the extensive and real application for real-time sensing [7, 8]. Thus, sensitive, rapid, and accurate detection methods are urgently required.

Due to their unique properties such as enhanced evanescent fields, tight light confinement, and large waveguide dispersion, microfibers have attracted extensive interests since Tong's first demonstration in 2003 [9, 10]. Microfibers

and related structures were intensively investigated for various sensor applications, such as temperature sensor [11–14], RI (refractive index) refractometer [15–18], and gas sensor [19–21]. A biosensor based on conventional fused fiber coupler was proposed by Tazawa et al. in 2007 [22]. It has been known that the transmission spectrum of a microfiber is strongly affected by the RI of the surrounding medium because of evanescent field generated on the fiber surface at the fused region. Hence, a higher sensitivity can be obtained by properly decreasing the diameter of a microfiber. Microfiber structure fabricated by Liao et al. [23] as a RI sensor has a sensitivity of 2735 nm/RIU (refractive index unit, RIU). In the article, we fabricated a type of biosensor for the detection of *E. coli* concentration based on microfiber gratings (MFGs), which has a great potential application for real-time monitoring of the growth of *E. coli*.

2. Experimental Methods

2.1. Microfiber Preparation. Figure 1(a) shows the microfiber fabrication diagram. Telecom single-mode fibers (SMF28, Corning) were put carefully into the taper drawing system, and then, a low-loss microfiber was fabricated by

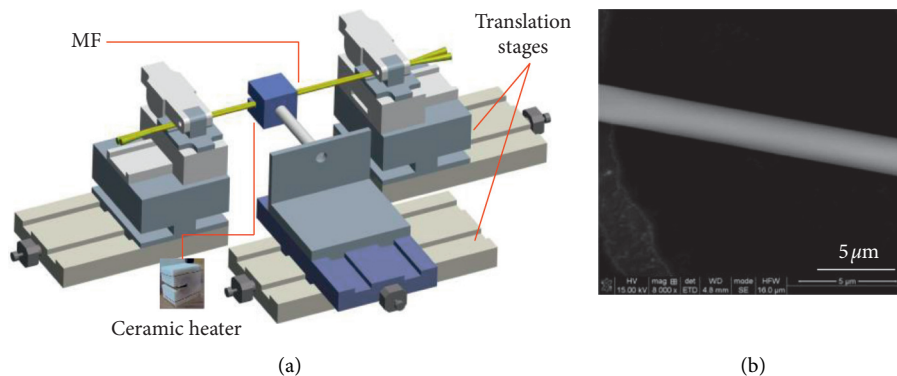


FIGURE 1: (a) Microfiber fabrication setup; (b) the SEM image of the waist region of prepared microfiber. The diameter of each fused microfiber is about $2\ \mu\text{m}$.

using the heating brushing technique [24]. Figure 1(b) is a scanning electron microscope (SEM) image of the waist region of the prepared microfiber, which indicates that the diameter of the microfiber is about $2\ \mu\text{m}$.

2.2. Sensor Fabrication. MFGs were fabricated by using a high-frequency CO_2 laser. The number of periods is 30, and the length of the period is $600\ \mu\text{m}$. The transmission spectrum of MFG displays resonant behavior due to periodic modulation of microfiber surface RI.

The free-standing MFG could be affected by environmental factors such as physical vibration and air flow due to its poor mechanical stability, which will produce large measurement errors and disturb sensing results.

In order to improve the mechanical stability of MFG and enhance the repeatability of the entire sensing system, packaged MFG in a surrounding structure using a low RI UV curable polymer (Thorlabs) is essential. Figure 2 shows the schematic diagram of the embedded MFG and experimental setup. A microscope slide was firstly covered with two small slides in parallel to create an open-top channel. Then, two blocks of thin slides were used to seal the two ends of the channel and to support the MFG sample in place. Then, the fabricated MFG was placed into the channel, and the entire coupler was suspended in the sensing environment. Several drops of UV curable polymer were used to fix the MFG sample. The entire sensing sample was exposed under UV radiation (UV LED system, Thorlabs) for 60 seconds. At last, an uncovered section with length about 15 mm in the center of the channel was formed, which was to be used for the *E. coli* sensing experiment. A semiconductor laser diode (SLD, Throlab S5FC 1550P-A2) with a central wavelength of 1550 nm was used as the optical source. It was connected to the input port of the MFG. An optical spectrum analyzer (OSA) (Yokogawa, 6370C) was connected to the outputs of the MFG to record the output transmission spectra.

2.3. Biosensing Experiment. Culture medium without bacteria is a basic element in biosensing experiment, which is significant for the culture of bacteria. Culture medium was

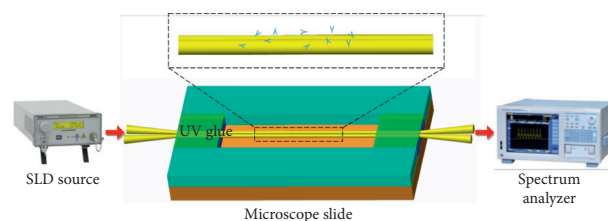


FIGURE 2: Schematic diagram of the embedded MFG and experimental setup.

preserved at -20°C and refrigerated at 4°C . Other preparation works were performed at room temperature and would last for about 5 minutes, during which the temperature of culture medium would rise. Organic contaminants adhered to the surface of the entire sensing sample, and cuvettes were removed by washing with pure ethyl alcohol.

3. Results and Discussion

In this experiment, temperature is a main factor for the reproduction behavior of the bacteria. Thus, the sensing process was divided into two stages. At the first stage, the culture medium had a low temperature and the reproduction of bacteria was slow. 3 ml culture medium with an initial bacterial concentration of 1×10^7 CFU/ml was dropped into the channel of the sensing sample. Measured spectral responses were recorded every 30 min. At the second stage, bacteria reproduced actively at room temperature, which was much faster than that in the first stage. The initial bacterial concentration was 1.9×10^7 CFU/ml. Measured spectral responses were recorded every 5 min. Distinguishing the two stages will contribute to the data analyzation.

For the first stage, the initial bacterial concentration was 1×10^7 CFU/ml. Measured spectral responses were recorded every 30 min. Figure 3(a) illustrates the measured spectral responses during the first 4 hours, and Figure 3(b) shows the dip wavelength shift corresponding to the spectral responses. The dip wavelength showed a blueshift from 1554.68 nm to 1550.06 nm with the increase of time, with an average blueshift speed of about 0.018 nm/min, which could be due

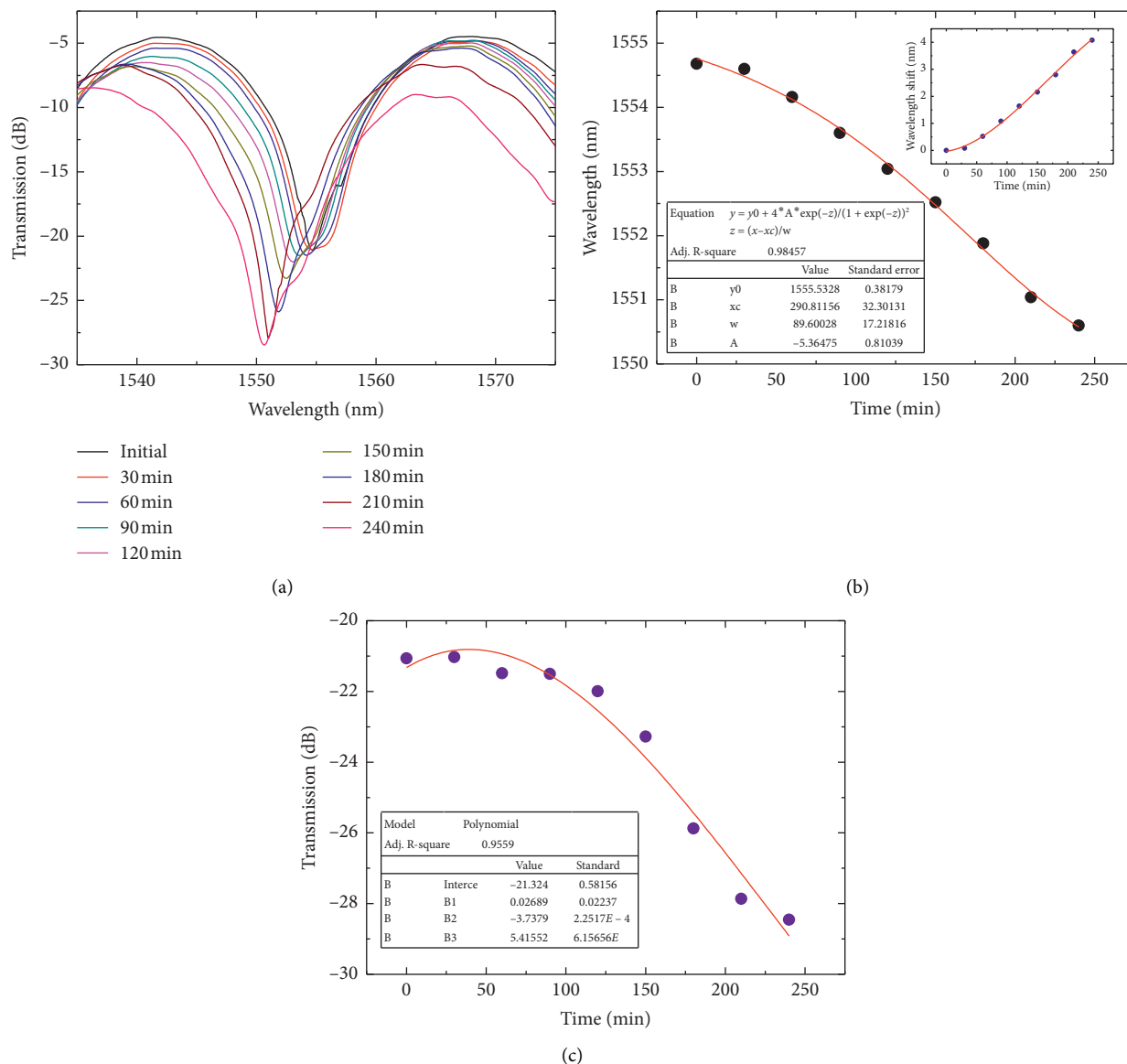


FIGURE 3: (a) Measured spectral responses during the first 4 hours, which was recorded every 30 min; the wavelength shift (b) and transmission loss (c) during the first 4 hours, which were caused by the change of the bacterial concentration.

to the slow reproduction of bacteria in the culture medium at low temperature. Figure 3(c) indicates the transmission varies with the increase of measuring time. The transmission increased a little bit from -21.065 dB to -21.031 dB during the first 30 min, which could be due to the low concentration of bacteria in the culture medium at low temperature. The number of bacteria decreased during the first 30 min. Then, the transmission decreased from -21.0318 dB to -28.402 dB with further increase of time, which could be due to the slow reproduction of *E. coli*. The number of *E. coli* gradually increased.

For the second stage, the temperature of the tested sample was the room temperature. The initial bacterial concentration was 1.9×10^7 CFU/ml. Measured spectral responses were recorded every 5 min. Figure 4(a) illustrates the wavelength shift corresponding to the spectral responses

during the half-hour; and measured wavelength shift and transmission loss with the increase of time are given in Figures 4(b) and 4(c). Results indicate that the dip wavelength has a linear blueshift from 1550.6 nm to 1535.36 nm with the increase of time, with a blueshift speed of about 0.5 nm/min, much higher than that at the first stage (0.018 nm/min). The fast reproduction rate of *E. coli* at the room temperature is the main reason for the fast blueshift speed at the second stage. The transmission decreased from -28.4289 dB to -38.9895 dB. The decrease in speed of the transmission at this stage is about 12 times in comparison with that in the first stage. This phenomenon can be explained by basic biology theories that the number of bacteria in culture medium increases drastically. Experimental results indicate that both the dip wavelength and transmission can be employed to monitor the concentration

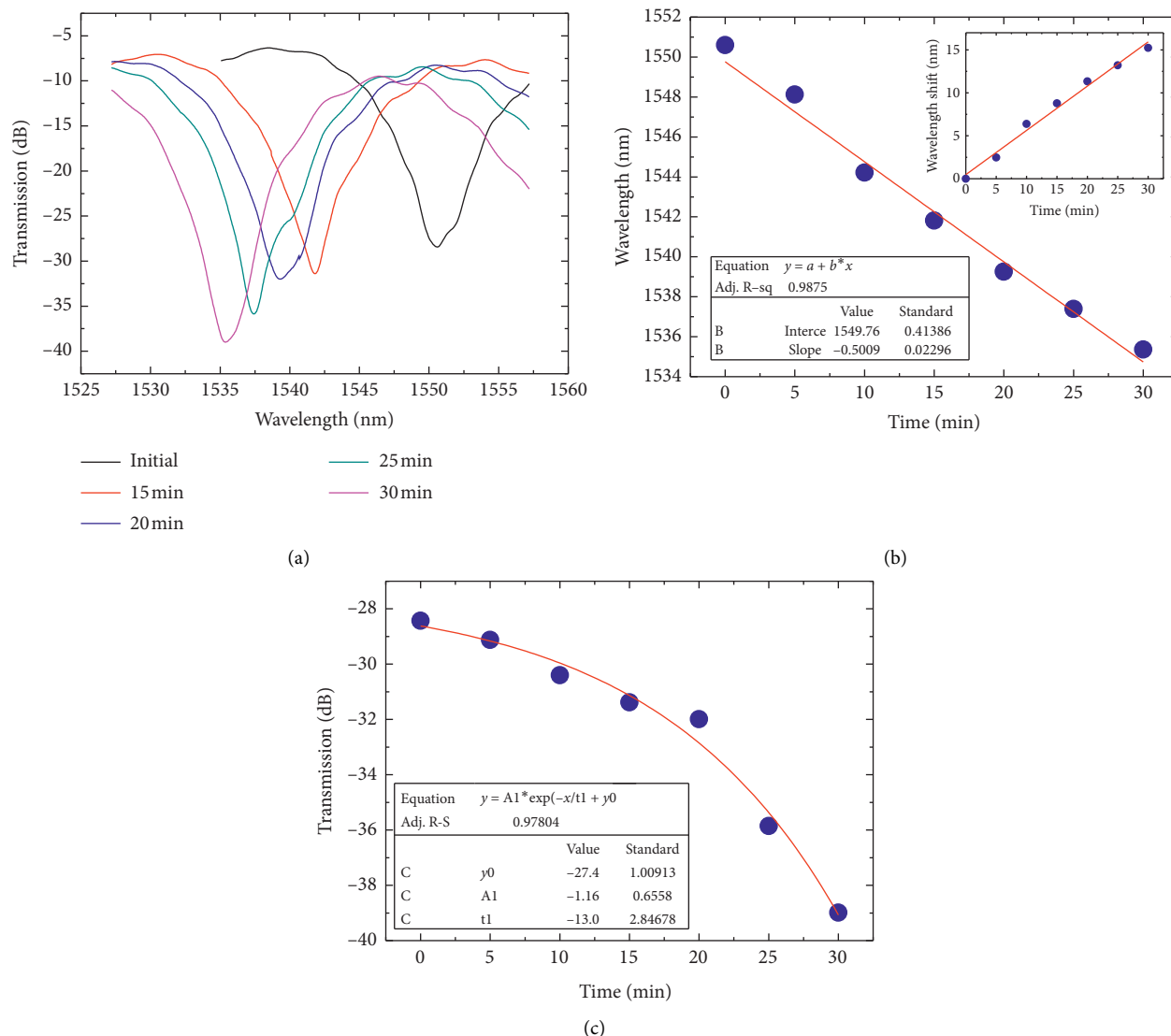


FIGURE 4: (a) Measured spectral responses after 4 hours, which was recorded every 5 min; the wavelength shift (b) and transmission loss (c) caused by the change of the bacterial concentration.

of *E. coli*. Compared with transmission loss, dip wavelength is a more sensitive factor (2.3 times).

In order to verify the relationship between bacterial concentration and dip wavelength shift, 5 ml culture medium with *E. coli* (the initial concentration is 0.047%, 1×10^7 CFU/ml) was dropped into the channel of the sensing sample and cuvette, respectively. The reproduction rates of *E. coli* are the same for the culture medium with the same volume at the same temperature. OD (optical density) of the culture medium was measured by using a spectrophotometer (Shimadzu, UV-2600). The average values of OD were adopted from three cuvettes in order to obtain a higher accuracy. Spectral responses and ODs were recorded every 30 min.

Time-dependent wavelength shift for real-time sensing is given in Figure 5(a). Resonance wavelength was recorded every 30 min, and the total measuring time was 270 min. The wavelength shift increased exponentially with the increase of

time. At the beginning of the sensing process (within 240 min), the wavelength shifts slowly due to the slow reproduction rate of *E. coli* at low temperature. While after 240 min, the wavelength shift dramatically increased, indicating a drastic reproduction of *E. coli* at room temperature. This result is consistent with result in Figures 3 and 4. Figure 5(b) illustrates the exponential relationship between OD and dip wavelength. The dip wavelength shows a blueshift from 1554.68 nm to 1515.26 nm with the increase of OD. OD is proportional to the concentration of *E. coli* in culture medium. It indicates that the concentration of *E. coli* can be obtained from the value of wavelength shift according to expressions in Figure 5.

The behavior of the prepared sensor for the detection of the concentration of *E. coli* is shown in Figure 6. It indicates that the detected signal increased monotonously with the increasing concentration of *E. coli*. An exponent fitting was applied to the sensitivity variation with respect to dip

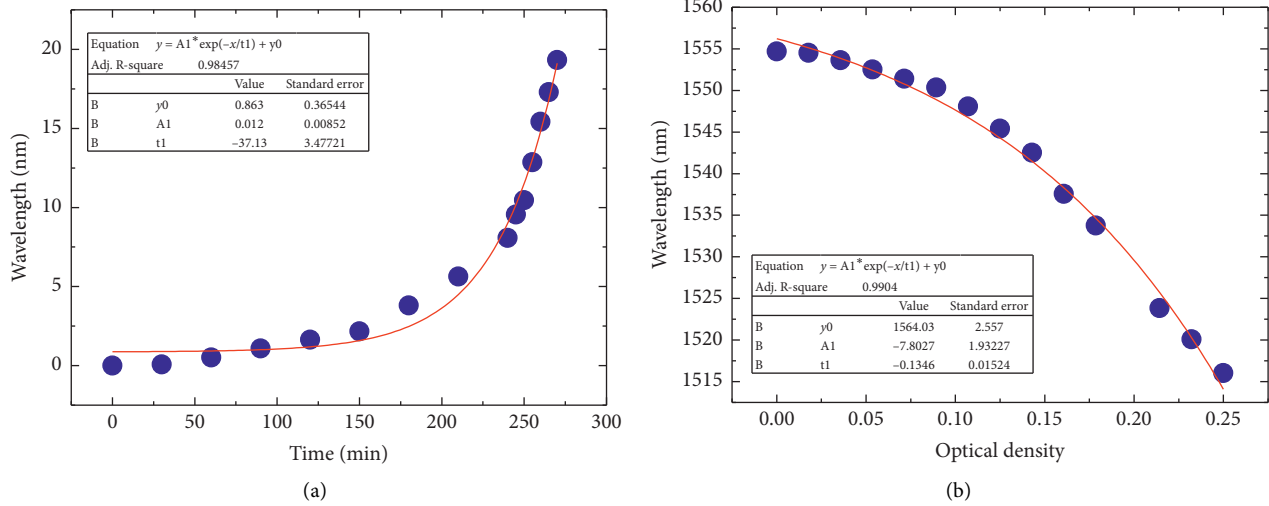


FIGURE 5: (a) Time-dependent wavelength shift and resonance wavelength was recorded every 30 min. (b) The relationship between dip wavelength and optical density.

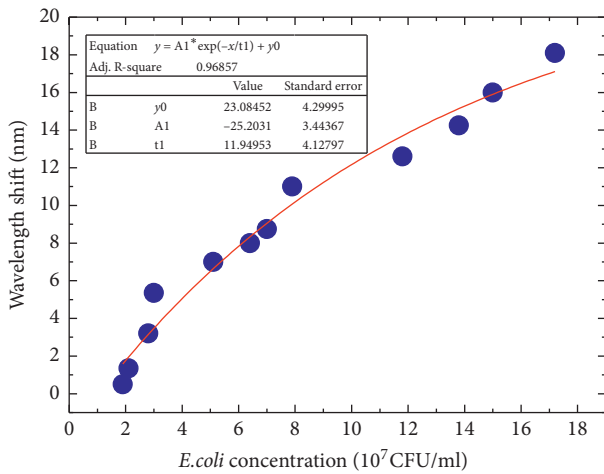


FIGURE 6: The behavior of prepared sensor for the detection of the *E. coli*. Experimental results were recorded after the culture medium was exposed at room temperature 1 h later.

wavelength shift in Figure 6. A maximum sensitivity of 1.15 nm/107 CFU was achieved by using the fabricated sensor. It implies that real-time sensing of concentration of *E. coli* can be achieved by using the MFG sample according to the relationship between dip wavelength shift and the concentration of detected bacteria.

Generally, the MFGs can allow power transfer between the guided modes when a certain resonant condition is satisfied, which leads to a series of transmission dips in the spectrum. The coupling of modes with high diffraction orders has been first demonstrated in conventional fibers. The MFGs can be used in simultaneous sensing application. The resonant condition of the MFGs can be expressed as

$$\lambda_{\text{res}} = \frac{(n_{\text{eff}1} - n_{\text{eff}2})\Lambda}{N}, \quad (1)$$

where λ_{res} is the resonant wavelength, Λ is the grating period, N is the diffraction order, and $n_{\text{eff}1}$ and $n_{\text{eff}2}$ are the effective indices for the lower- and higher-order guided modes, respectively. Based on Eq. (1), for the same resonant wavelength and the same coupled modes, the larger value of N has the longer grating period Λ . The variation of ambient refractive index (n_{ex}) can produce different changes to the dissimilar mode indices, which leads to a modification of the mode-index difference and induces the shift of the spectrum. By taking a small variation of n_{ex} from Eq. (1), the sensitivity of dip wavelength to refractive index can be expressed as

$$S = \frac{d\lambda}{dn} = \frac{\lambda \partial \Delta n / \partial n_{\text{ex}}}{(\Delta n - \lambda \partial \Delta n / \partial \lambda)}. \quad (2)$$

It is shown that the sensitivity is independent on either the diffraction order or the grating period, but it is dependent on the microfiber diameter and the operating wavelength.

4. Conclusion

Real-time sensing for the concentration of *E. coli* based on MFG structure is proposed and experimentally demonstrated in this article. The MFG sample was fabricated based on the taper drawing system by using the heating brushing technique. The performance of the sensor in culture medium with *E. coli* in the wavelength domain was evaluated. Results showed that compared with transmission loss, dip wavelength is more sensitive to the concentration of bacteria. The MFG-based sensor is capable of real-time sensing for the concentration of *E. coli*. A maximum sensitivity of 1.15 nm/107 CFU was achieved in our experiment. The detection mechanism could be due to the relationship between dip wavelength shift and the concentration of bacteria. The fabricated MFG structure does not need any coating. Considering the simple structure, compact size, low cost, and high sensitivity of the proposed MFG-based sensor, this

research offers a sensitive, rapid, and accurate solution for the detection of bacteria in advanced biology fields.

Data Availability

Data used to support the findings of this study are included within the article.

Conflicts of Interest

The authors declare that there are no conflicts of interest regarding the publication of this paper.

Acknowledgments


The authors thank Laser Fusion Research Center for providing the samples. This work was supported by the National Natural Science Foundation of China (NSFC) (Grant No. 61705205).

References

- [1] S. Bonacorsi and E. Bingen, "Molecular epidemiology of *Escherichia coli* causing neonatal meningitis," *International Journal of Medical Microbiology*, vol. 295, no. 6-7, pp. 373-381, 2005.
- [2] C. F. Marrs, L. Zhang, and B. Foxman, "Escherichia coli-mediated urinary tract infections: are there distinct uropathogenic *E. coli* (UPEC) pathotypes?" *Fems Microbiology Letters*, vol. 252, no. 2, pp. 183-190, 2005.
- [3] Y. H. Hui, R. Gorham, K. D. Murrell et al., *Foodborne Disease Handbook*, Marcel Dekker, New York City, NY, USA, 1994.
- [4] E. J. Klein, D. R. Boster, J. R. Stapp et al., "Diarrhea etiology in a children's hospital emergency department: a prospective cohort study," *Clinical Infectious Diseases*, vol. 43, no. 7, pp. 807-813, 2006.
- [5] J. R. Johnson, "Microbial virulence determinants and the pathogenesis of urinary tract infection," *Infectious Disease Clinics of North America*, vol. 17, no. 2, pp. 261-278, 2003.
- [6] A. K. Bej, M. H. Mahbubani, J. L. Dicesare, and R. M. Atlas, "Polymerase chain reaction-gene probe detection of microorganisms by using filter-concentrated samples," *Applied and Environmental Microbiology*, vol. 57, no. 12, pp. 3529-3534, 1991.
- [7] M. Kandpal, R. K. Gundampati, and M. Debnath, "Surface charge based rapid method for detection of microbial contamination in drinking water and food products," *World Academy of Science Engineering & Technology*, vol. 58, 2009.
- [8] V. Dixit, J. C. Tewari, and B. S. Sharma, "Detection of *E. coli* in water using semi-conducting polymeric thin film sensor," *Sensors and Actuators B: Chemical*, vol. 120, no. 1, pp. 96-103, 2006.
- [9] L. Tong, R. R. Gattass, J. B. Ashcom et al., "Subwavelength-diameter silica wires for low-loss optical wave guiding," *Nature*, vol. 426, no. 6968, pp. 816-819, 2004.
- [10] L. Tong, J. Lou, and E. Mazur, "Single-mode guiding properties of subwavelength-diameter silica and silicon wire waveguides," *Optics Express*, vol. 12, no. 6, pp. 1025-1035, 2004.
- [11] J.-l. Kou, J. Feng, L. Ye, F. Xu, and Y.-Q. Lu, "Miniaturized fiber taper reflective interferometer for high temperature measurement," *Optics Express*, vol. 18, no. 13, pp. 14245-14250, 2010.
- [12] H. Yang, S. Wang, X. Wang, J. Wang, and Y. Liao, "Temperature sensing in seawater based on microfiber knot resonator," *Sensors*, vol. 14, no. 10, pp. 18515-18525, 2014.
- [13] I. Hernandez-Romano, D. Monzon-Hernandez, C. Moreno-Hernandez, D. Moreno-Hernandez, and J. Villatoro, "Highly sensitive temperature sensor based on a polymer-coated microfiber interferometer," *IEEE Photonics Technology Letters*, vol. 27, no. 24, pp. 2591-2594, 2015.
- [14] P. Wang, M. Ding, G. Bramilla et al., "High temperature performance of an optical microfiber coupler and its potential use as a sensor," *Electronics Letters*, vol. 5, no. 48, pp. 283-284, 2012.
- [15] J. Wo, G. Wang, Y. Cui et al., "Refractive index sensor using microfiber-based Mach-Zehnder interferometer," *Optics Letters*, vol. 37, no. 1, pp. 67-69, 2012.
- [16] W. B. Ji, H. H. Liu, S. C. Tjin, K. K. Chow, and A. Lim, "Ultrahigh sensitivity refractive index sensor based on optical microfiber," *IEEE Photonics Technology Letters*, vol. 24, no. 20, pp. 1872-1874, 2012.
- [17] Z. Xu, Q. Sun, B. Li et al., "Highly sensitive refractive index sensor based on cascaded microfiber knots with vernier effect," *Optics Express*, vol. 23, no. 5, pp. 6662-6672, 2015.
- [18] L. Bo, P. Wang, and Y. Semenova, G. Farrell, "High sensitivity fiber refractometer based on an optical microfiber coupler," *IEEE Photonics Technology Letters*, vol. 25, no. 3, pp. 228-230, 2013.
- [19] Y. Wu, B. Yao, A. Zhang et al., "Graphene-coated microfiber Bragg grating for high-sensitivity gas sensing," *Optics Letters*, vol. 39, no. 5, pp. 1235-1237, 2014.
- [20] B. Yao, Y. Wu, Y. Cheng et al., "All-optical Mach-Zehnder interferometric NH₃ gas sensor based on graphene/microfiber hybrid waveguide," *Sensors and Actuators B: Chemical*, vol. 194, pp. 142-148, 2014.
- [21] C.-B. Yu, Y. Wu, X.-L. Liu et al., "Graphene oxide deposited microfiber knot resonator for gas sensing," *Optical Materials Express*, vol. 6, no. 3, pp. 727-733, 2016.
- [22] H. Tazawa, T. Kanie, and M. Katayama, "Fiber-optic coupler based refractive index sensor and its application to biosensing," *Applied Physics Letters*, vol. 91, no. 11, p. 677, 2007.
- [23] C. R. Liao, D. N. Wang, X. He, and M. W. Yang, "Twisted optical microfibers for refractive index sensing," *IEEE Photonics Technology Letters*, vol. 23, no. 13, pp. 848-850, 2011.
- [24] G. Bramilla, V. Finazzi, and D. J. Richardson, "Ultra-low-loss optical fiber nanotapers," *Optics Express*, vol. 12, no. 10, pp. 2258-2263, 2004.

Research Article

Effects of Laser Scanning Speed on Microstructure, Microhardness, and Corrosion Behavior of Laser Cladding Ni45 Coatings

Yanxin Qiao ¹, Jie Huang,¹ Ding Huang,¹ Jian Chen,¹ Wen Liu,¹ Zhengbin Wang ²,
and Zheng Zhibin³

¹School of Materials Science and Engineering, Jiangsu University of Science and Technology, Zhenjiang 212003, China

²CAS Key Laboratory of Nuclear Materials and Safety Assessment, Institute of Metal Research, Chinese Academy of Sciences, Shenyang 110016, China

³Guangdong Key Laboratory for Technology and Application of Metal Toughening, Guangzhou Institute of Materials and Processing, Guangzhou 510650, China

Correspondence should be addressed to Yanxin Qiao; yxqiao@just.edu.cn and Zhengbin Wang; zawang12s@imr.ac.cn

Received 30 January 2020; Revised 15 June 2020; Accepted 9 July 2020; Published 3 August 2020

Academic Editor: Mohamed Azaroual

Copyright © 2020 Yanxin Qiao et al. This is an open access article distributed under the Creative Commons Attribution License, which permits unrestricted use, distribution, and reproduction in any medium, provided the original work is properly cited.

The effects of laser scanning speed on the microstructure, microhardness, and corrosion behavior of Ni45 coatings were investigated by using optical microscopy (OM), scanning electron microscopy (SEM), X-ray diffraction (XRD), microhardness, and electrochemical measurements. The results showed that increasing laser scanning speed promotes the transformation from planar crystals to dendrites and refines the grains concurrently. The γ -(Ni, Fe), FeNi₃, and M₂₃(C,B)₆ are identified as the primary phase composition in the Ni45 coatings regardless of the laser scanning speed. Thereinto, the formation and growth of M₂₃(C,B)₆ precipitates can be inhibited with increasing laser scanning speed due to the higher cooling rate, which affects the microhardness distribution and corrosion resistance of the coating. On the one hand, the microhardness of the whole coating presents a downtrend with increasing laser scanning speed due to the reduction of M₂₃(C,B)₆ phase. On the other hand, the corrosion resistance in 0.5 M NaCl solution is improved to some extent at higher laser scanning speed because the less precipitation of M₂₃(C,B)₆ reduces the depletion of Cr around the precipitates. In contrast, all the coatings exhibit undifferentiated but poor corrosion resistance in the highly corrosive 0.5 M NaCl + 0.5 M H₂SO₄ solution.

1. Introduction

Cladding technologies are usually employed to modify the surface structure and properties of alloys [1, 2], among which laser cladding exhibits some promising advantages [3–5]. First, it is a simple, green, economic, and efficient process, which can make the surface coating have better corrosion resistance and wear resistance than the substrate [6, 7]. Secondly, a strong metallurgical bond can form between the coating and substrate [4, 8, 9], and the size of the heat-affected zone (HAZ) is usually small [4, 10, 11]. Lastly, it is relatively easy to control the process parameters and to be automated [4, 12, 13]. Liu et al. [5] developed a composite

coating by laser cladding on Ti-6Al-4V alloy with superior wear resistance. The results showed that the average microhardness and wear loss of the coating were twice larger and 10~30% lower than those of the substrate, respectively. Fesharaki et al. [14] reported better metallurgical bonding of Inconel 625 coating prepared by laser cladding than that developed by Tungsten Inert Gas Welding (TIG) cladding. Tanigawa et al. [15] found that the HAZ of laser cladding prepared Ni-Cr-Si-B alloy coating on C45 carbon steel can be shrunken by employing smaller particles.

Nickel-based superalloys are widely used in the laser cladding process due to their superior mechanical properties and wear resistance [16–18]. Chen et al. [3] found that the

microhardness of the Ni-Cr-B-Si composite coatings increased with increasing laser scanning speed (5, 10, 15, and 20 mm/s). Sun et al. [19] studied the effects of NbC on the wear properties of Ni45 coating and reported that the microhardness and wear resistance were significantly improved by the addition of NbC. However, these works are mainly focused on the hardness and wear resistance with very little attention on corrosion behavior. Keeping in mind that corrosion is usually one of the reasons for the reduction in the service life of nickel-based alloys, it is, therefore, worthwhile to evaluate the corrosion resistance of nickel-based alloy coatings prepared by laser cladding, especially to clarify the correlation between corrosion resistance and microstructure.

For this purpose, three laser cladded nickel-based alloy coatings on carbon steel substrate were prepared, adjusting the microstructure by controlling the laser scanning speed (4 mm/s, 6 mm/s, and 10 mm/s). The effects of laser scanning speed on the microstructure, microhardness, and corrosion behavior were investigated by optical microscopy (OM), scanning electron microscopy (SEM), X-ray diffraction (XRD), microhardness, and electrochemical measurements. The evolution of microhardness and corrosion behavior with laser scanning speed was explained in terms of microstructure.

2. Experimental Methods

2.1. Preparation of Ni45 Coatings. The substrate material used in this study was medium carbon steel AISI 1045 (0.42~0.50 wt.% C, 0.17~0.37 wt.% Si, 0.50~0.80 wt.% Mn, 0.25 wt.% Cr, ≤ 0.25 wt.% Cr, ≤ 0.30 wt.% Ni, ≤ 0.25 wt.% Cu, ≤ 0.035 wt.% P and Fe balance) with dimensions 110 mm \times 100 mm \times 10 mm. The surface of the substrate was ground with 150# sandpaper and cleaned with acetone. Ni45 powder (0.34 wt.% C, 2.0 wt.% B, 4.1 wt.% Si, 12.5 wt.% Cr, 6.6 wt.% Fe and Ni balance) obtained from Beijing AMC Powder Metallurgy Technology Co., Ltd. (Beijing, China), was employed as the cladding material, and its SEM morphology is shown in Figure 1. Before laser cladding, the alloy powder was baked in a vacuum environment (to remove moisture and avoid oxidation) and then ground in a mortar for at least 5 minutes to guarantee uniformity in powder mixing.

CO₂ laser with Siemens 820C computer numerical control (CNC) system was used in preparing the coating. The schematic of the laser cladding process employed in this work is shown in Figure 2, and the operating parameters are listed in Table 1. Before the experiment, the cladding powder and bonder were preplaced on the surface of AISI 1045 steel by a self-made powder paving device. After the laser cladding, the samples were cut into coupons with dimensions 10 mm \times 10 mm \times 5 mm. Then, the samples were cleaned and inlaid for subsequent microstructure observation and property testing.

2.2. Microstructure Observation and Microhardness Measurement. The crystal structures of the Ni45 coatings were investigated by an X-ray diffractometer (XRD, Bruker

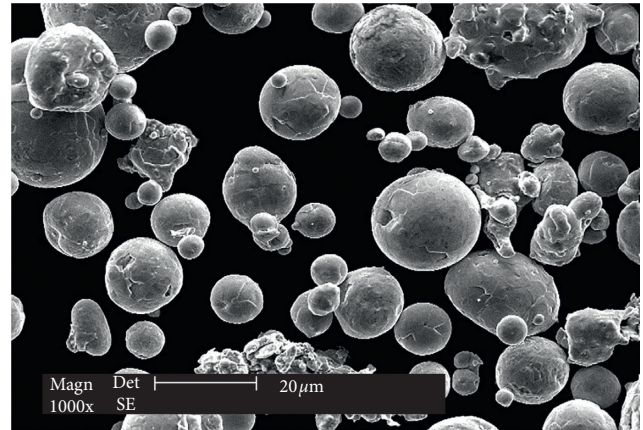


FIGURE 1: SEM morphology of Ni45 powders.

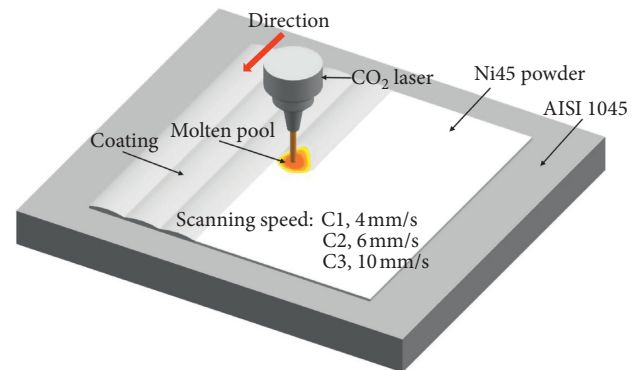


FIGURE 2: Schematic of the laser cladding process.

TABLE 1: Operating parameters of the laser cladding process.

Operating parameters	Values
Output power (W)	1600
Scanning speed (mm/s)	4 (C1), 6 (C2), 10 (C3)
Beam diameter (mm)	4
Overlapped width (mm)	2.5
The number of passes	8
Protective gas rate (L/min)	10
Carrier gas flow rate (L/min)	12

D8 Advance) with the diffraction angle (2θ) ranging from 10° to 90° and a Cu-K α radiation at 40 kV and 35 mA at a step size of 0.02° and a scan rate of 6°/min. The microstructures of the as-prepared coatings were characterized by an optical microscope (OM, KEYENCE-VHX-900E) and scanning electron microscope (SEM, XL30-FEG ESEM) with energy dispersive spectroscope (EDS, Oxford INCA) after the samples were mechanically polished and etched in the 3 wt.% HNO₃ solution. The microhardness distribution along the cross section of the Ni45 coatings was measured using HDX-1000 microhardness tester with a load of 300 g and a dwell time of 15 s.

2.3. Electrochemical Corrosion Test. The electrochemical corrosion behavior of the as-prepared coatings was assessed using CS350 electrochemical workstation (Wuhan Corrtest Instruments Corp., Ltd., Wuhan, China) in 0.5 M NaCl solution and 0.5 M NaCl + 0.05 M H₂SO₄ solution. All the electrochemical tests were conducted using a three-electrode electrochemical cell composed of a saturated calomel reference electrode (SCE), a platinum counter electrode, and a coated sample working electrode [20]. Preceding the electrochemical tests was the monitoring of the open circuit potential (OCP) for 1 h to achieve a relatively stable state. The electrochemical impedance spectroscopy (EIS) tests were performed at OCP with a sinusoidal potential perturbation of 10 mV in a frequency range from 10⁵ Hz to 10⁻² Hz. The potentiodynamic polarization curves were measured by sweeping the potential from -0.6 V_{SCE} to 2.0 V_{SCE} at a scanning rate of 0.5 mV/s and terminated when the current density of 50 mA/cm² was reached. The electrochemical tests were conducted at 25 ± 1°C in the air without stirring, and triplicate measurements were done to ensure repeatability.

3. Results and Discussion

3.1. Morphology Observation. Figure 3 shows the surface appearance of Ni45 coatings after laser cladding processes. The coating material was melted sufficiently, and continuous coatings were formed on the substrate. All coatings had a uniform geometric appearance, and the overlaps between adjacent passes were almost parallel to each other.

Figure 4 displays the OM of the transition layers between the coatings and substrate. All the interfaces were free of cracks and pores, indicating good bondings between the substrate and coatings. The thickness of the transition layer between the coating and HAZ decreased with increasing laser scanning speed, which resulted from the hindered element diffusion between the coatings and substrate at a shorter heating time during the laser cladding process [8, 21, 22]. Many columnar grains appeared around the transition layer, due to extreme undercooling at the bottom of the molten pool [23]. Meanwhile, the direction of columnar growth was basically perpendicular to the transition layer along the direction opposite to the thermal flow movement [8, 13, 23, 24]. These features of columnar grains and microstructures are basically independent of the laser scanning speed. The cross-section microstructures of the as-prepared Ni45 coatings were observed by SEM in back-scattered electron mode and are presented in Figure 5. As seen in Figures 5(d)–5(f), more and finer dendrites appeared as the laser scanning speed increased from 4 mm/s to 10 mm/s, demonstrating that the grains tend to grow into finer dendrites at higher laser scanning speed. Also, many precipitation phases were observed in the intergranular areas for all the coatings [25].

According to the solidification theory, the alloy solidification mode mainly includes planar, cellular, dendritic, and equiaxed growth, which depends on the ratio of the temperature gradient (G) to solidification rate (R), i.e., G/R [13, 21, 24, 26, 27]. The temperature gradient was the largest

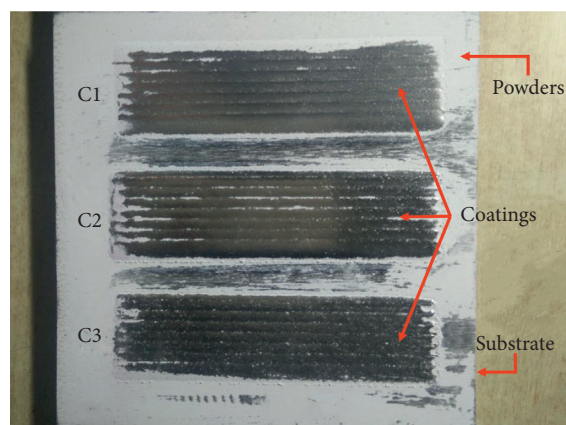


FIGURE 3: Surface appearance of Ni45 coatings after laser cladding processes.

at the beginning of the solidification process due to the low temperature of the substrate and the fact that the solidification rate was close to zero. Under this condition, the solid-liquid interface is stable, and a layer of planar front growth can form between coatings and substrates, just like the transition layer shown in Figure 3 [13, 21, 26, 27]. With the increase in distance from the bottom of the molten pool, the temperature gradient will decrease [26], and the solidification speed will increase [8, 24], resulting in a dramatic decline of G/R. As a result, the solid-liquid interface of the planar grain becomes unstable, promoting the transition of microstructure from plane crystals to cellular crystals [8, 21, 26]. With further movement of the solid-liquid interface far away from the bottom of the molten pool, the value of G/R becomes much smaller, resulting in the change of crystal growth mode from cellular to dendritic growth [26, 27], as shown in Figure 5. At the top of the molten pool, the dendrites transformed into equiaxed crystals due to the further decline of G/R caused by the heat released to the surrounding environment from multiple directions [21, 26, 27]. Accordingly, increasing the laser scanning speed will affect the microstructure evolution during the solidification process from two aspects. On the one hand, the value of G/R will decrease, which accelerates the transformation from planar crystals to cellular crystals and dendrites consequently [26, 28]. On the other hand, the grains nucleate abundantly due to the lower heat input and the more rapid solidification, resulting in the refinement of grains [13, 21, 22, 26, 29]. As a result, more and finer dendrites can be observed in the coatings prepared at higher laser scanning speed, as shown in Figure 5.

3.2. XRD and EDS Measurements. Figure 6 exhibits the XRD patterns of the as-prepared Ni45 coatings. The characteristic peaks correspond to the γ -(Ni, Fe), FeNi₃, and M₂₃(C,B)₆, respectively. Thereinto, the intensity of M₂₃(C,B)₆ peak showed the most noticeable difference among the three kinds of coatings, which decreased with the increase in laser scanning speed and even disappeared at 10 mm/s. Kesavan et al. [30] studied the microstructure characterization of a

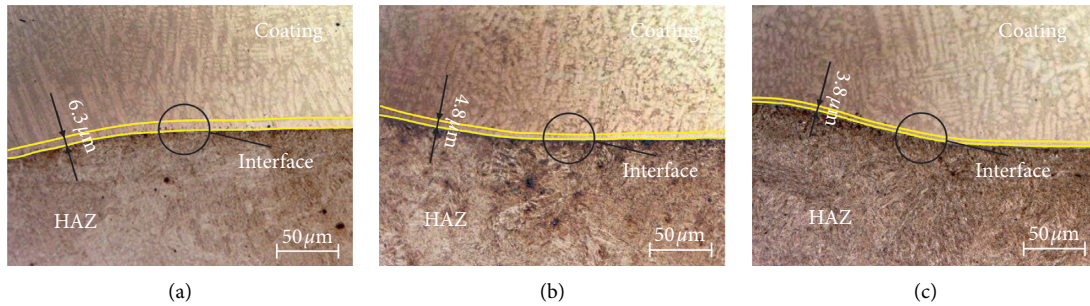


FIGURE 4: Optical microstructure of the interface between the substrate and the Ni45 coatings: (a) C1, (b) C2, and (c) C3.

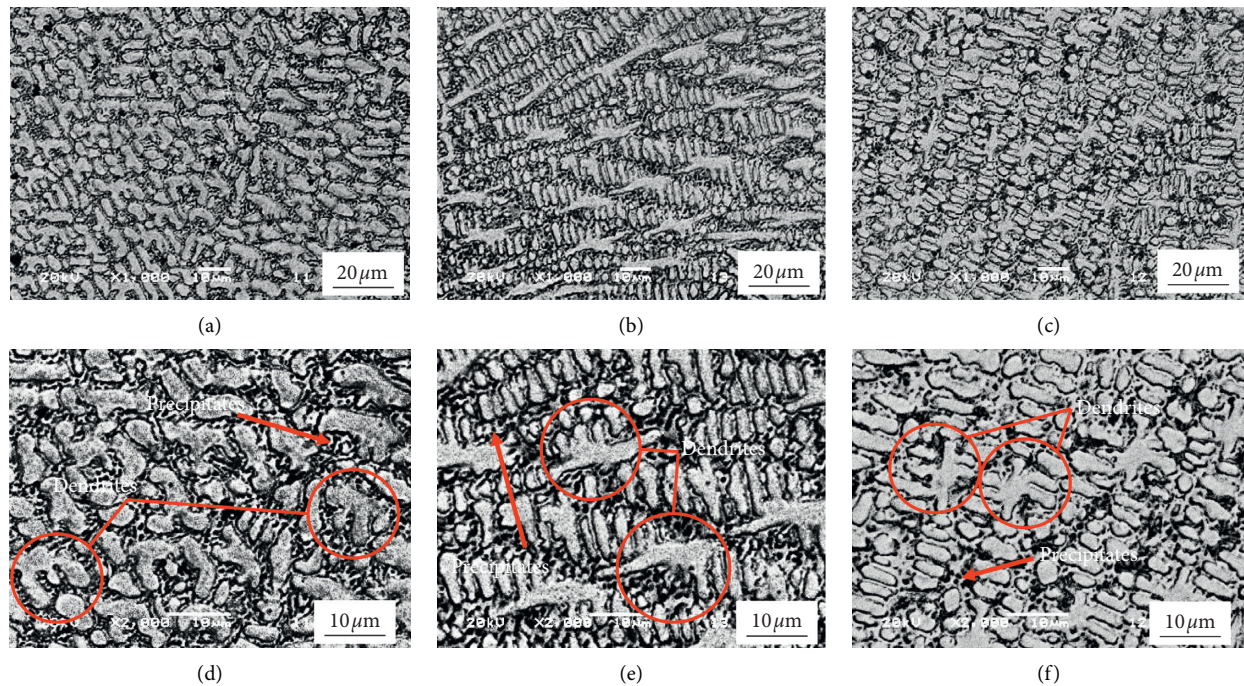


FIGURE 5: SEM images in backscattered electron mode of the cross-section microstructures of (a, d) C1, (b, e) C2, and (c, f) C3 coatings.

nickel-base hard-faced coating and reported that the microstructure of the deposits can be divided into dendrite and interdendritic regions. The dendrite region was composed of the γ -nickel phase, while the interdendritic region was composed of Cr-rich carbide and boride precipitates that are needle-, blocky-, floret-, and fine spherical-shaped. Liu et al. [31] investigated the microstructure of NiCoCrAlY coating deposited on cast iron using multilayer laser cladding. They described the dendrite in NiCoCrAlY alloy coating as the γ -(Fe,Ni) solid solution, and the phases in the interdendritic region as M_7C_3 and $M_{23}(C,B)_6$ carbides, where M represents Cr, Fe, or Ni.

It can be inferred that the dendrite region was composed of γ -phase, whereas the black particle phases in the interdendritic region were $M_{23}(C,B)_6$ precipitations. Meanwhile, the intensity of $M_{23}(C,B)_6$ peak was not noticeably observed in the XRD pattern of C2 and C3 coatings, which reflects that the volume fraction of

$M_{23}(C,B)_6$ precipitations decreased with increasing laser scanning speed [32]. This can be attributed to the high cooling rate induced by the high laser scanning speed [3, 28]. The inhibition of $M_{23}(C,B)_6$, together with the refined grain (Figure 5), could have effects on the microhardness and corrosion resistance of the Ni45 coatings [13, 30], which will be discussed in the following sections.

The elemental content of the dendrites in the C3 coating measured by EDS is listed in Figure 7. Only the contents of Fe, Cr, Ni, and Si were detected in the C3 coating because of the poor sensitivity of EDS in detecting light elements [13, 33]. Compared with the original Ni45 powders, the content of element Si, Cr, and Ni changed less after the laser cladding process, but a remarkable increase in the Fe content was observed. It indicates the element diffusion occurring between the substrate and the coating during the laser cladding process [34] and, therefore, demonstrating the formation of the transition layer discussed in Section 3.1.

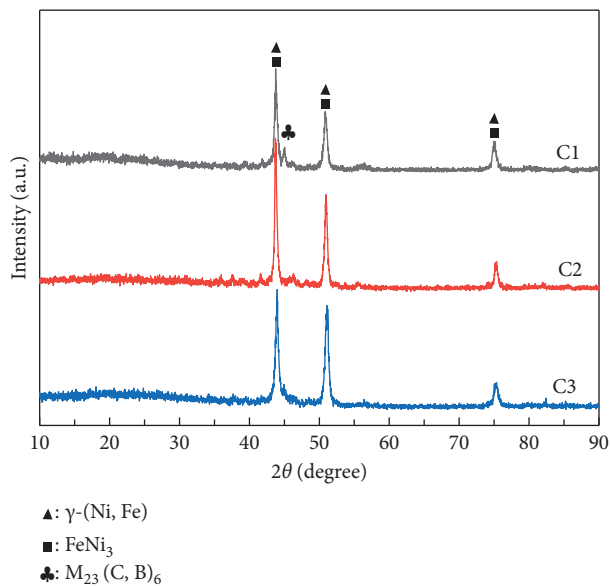


FIGURE 6: XRD patterns of as-prepared Ni45 coatings.

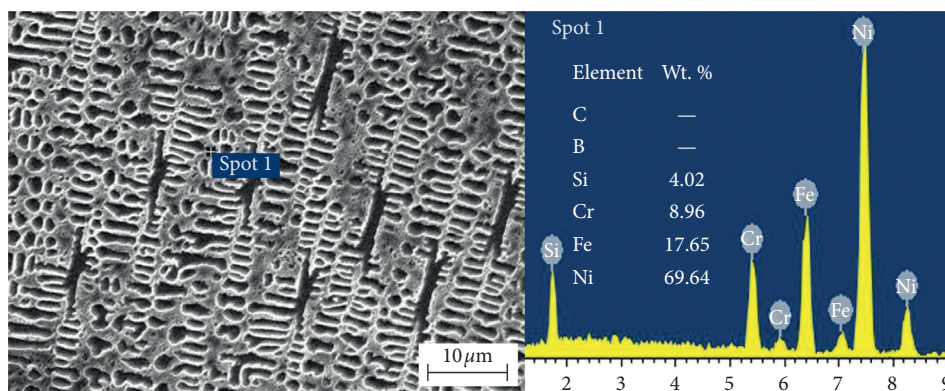


FIGURE 7: EDS analyses of the dendrites in C3 coating.

3.3. Microhardness Measurements. Figure 8 shows the microhardness distribution along the cross section of the as-prepared Ni45 coatings, in which the height and width of the rectangle represent the microhardness and the depth of different regions, respectively. The microhardness of the Ni45 coating ranges from 313.8 HV to 556.8 HV, which is significantly higher than that of the substrate. With increasing laser scanning speed, the microhardness of the coating decreased, while that of the substrate remained relatively unchanged. On the one hand, the higher laser scanning speed inhibited the formation and growth of borides and carbides, i.e., $\text{M}_{23}(\text{C, B})_6$ in Figure 6, which weakened the effect of precipitation strengthening [12, 13]. On the other hand, the grains were refined due to the higher cooling speed (Figure 5), leading to the improvement of microhardness [3, 13, 22]. Based on these two aspects, precipitation strengthening should be the dominant factor determining the microhardness of Ni45 coatings studied in this work [13]. Besides, the as-prepared coatings can be further divided into two parts based on the obvious step

change of coatings microhardness: the top and the bottom coatings. The microhardness of the top coatings was lower than that of the bottom when the laser scanning speed was 4 mm/s, while the relationship reversed at 6 mm/s and 10 mm/s. During the solidification process, the solidification phase transition occurred first at the bottom and then advanced to the top [28]. With continuous heating from the postsolidified metal droplets, the bottom microstructure grew coarsely [21, 23], whereas the top microstructure solidified rapidly and had no time to grow more coarsely due to the cooling effects of the external environments [21, 26]. Meanwhile, at low laser scanning speed (4 mm/s), there was enough time for the growth of carbides and borides, especially at the bottom, resulting in a higher microhardness of bottom coatings [3, 28]. The precipitation strengthening, in other words, should be the key factor determining the microhardness distribution inside the coating region at low scanning speed (4 mm/s). The higher the laser scanning speed, the fewer the amount of the precipitate of carbides and borides. As a result, the main

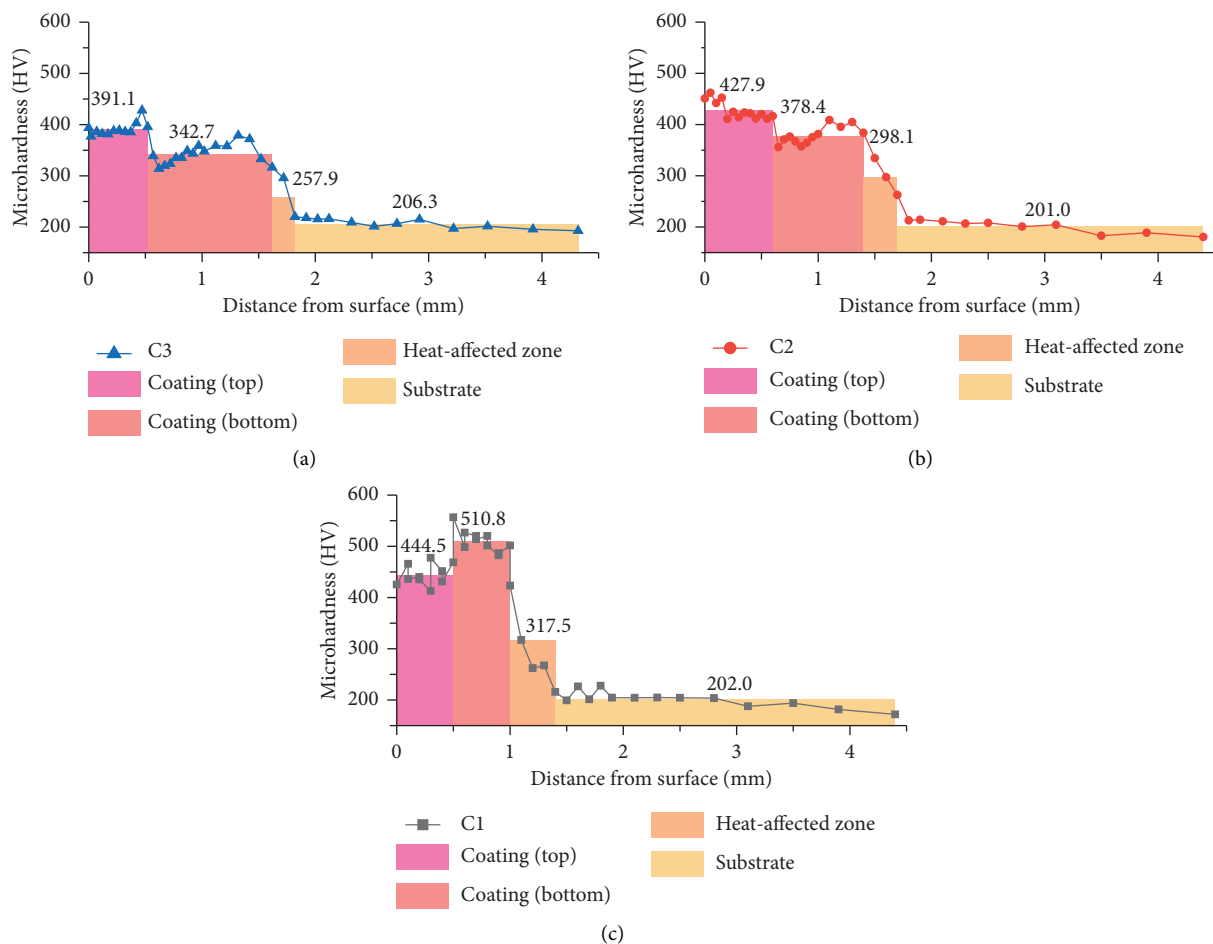


FIGURE 8: Microhardness distribution along the cross section of the as-prepared Ni45 coatings. The height and width of the colored rectangles represent the microhardness and the depth of different regions in the coatings.

strengthening mechanism influencing microhardness distribution could change from precipitation strengthening to grain refinement strengthening, leading to a higher microhardness of top coatings at high scanning speeds (6 mm/s and 10 mm/s).

In conclusion, whether the strengthening mechanism is precipitation strengthening or grain refinement strengthening, the coating microhardness can be improved effectively. For the whole coatings, the precipitation strengthening made more contribution to enhancing the microhardness of the coatings compared with the grain refinement strengthening. For hardness distribution inside the coating region, the controlling strengthening mechanism depended on the laser scanning speed. When the laser scanning speed was as low as 4 mm/s, the microhardness distribution was mainly influenced by the precipitation strengthening, whereas the grain refinement strengthening was the key factor determining the microhardness distribution as the laser scanning speed was increased to 6 mm/s and 10 mm/s.

3.4. Electrochemical Corrosion Behavior. The potentiodynamic polarization curves of the Ni45 coatings in 0.5 M NaCl and 0.5 M NaCl + 0.5 M H₂SO₄ solution are displayed

in Figure 9. The values of corrosion current density (i_{corr}) and corrosion potential (E_{corr}) based on Tafel extrapolation analysis are listed in Table 2. In both two solutions, the anodic current densities of all the coatings increased with the applied potential without exhibiting any active-to-passive transition. In 0.5 M NaCl solution, the corrosion potentials shifted nobly while the corrosion current densities decreased with the increase in laser scanning speed. It proves that the corrosion resistance of coatings in 0.5 M NaCl solution is improved by increasing the laser scanning speed [20, 28, 34, 35]. In contrast, lower corrosion potentials and higher corrosion current densities were observed for all coatings in 0.5 M NaCl + 0.5 M H₂SO₄ solution, implying a poor corrosion resistance in the more acidic environment. Moreover, the laser scanning speed seems to have no obvious effects on the corrosion resistance of Ni45 coatings in 0.5 M NaCl + 0.5 M H₂SO₄ solution, as shown in Figure 9(b) and Table 2.

Figure 10 depicts the Nyquist plots of the as-prepared Ni45 coatings in 0.5 M NaCl and 0.5 M NaCl + 0.5 M H₂SO₄ solutions. In 0.5 M NaCl solution (Figure 10(a)), one apparent unfinished capacitive impedance arc can be identified for all coatings. The radius of the capacitive impedance arc increased with the laser scanning speed, indicating the

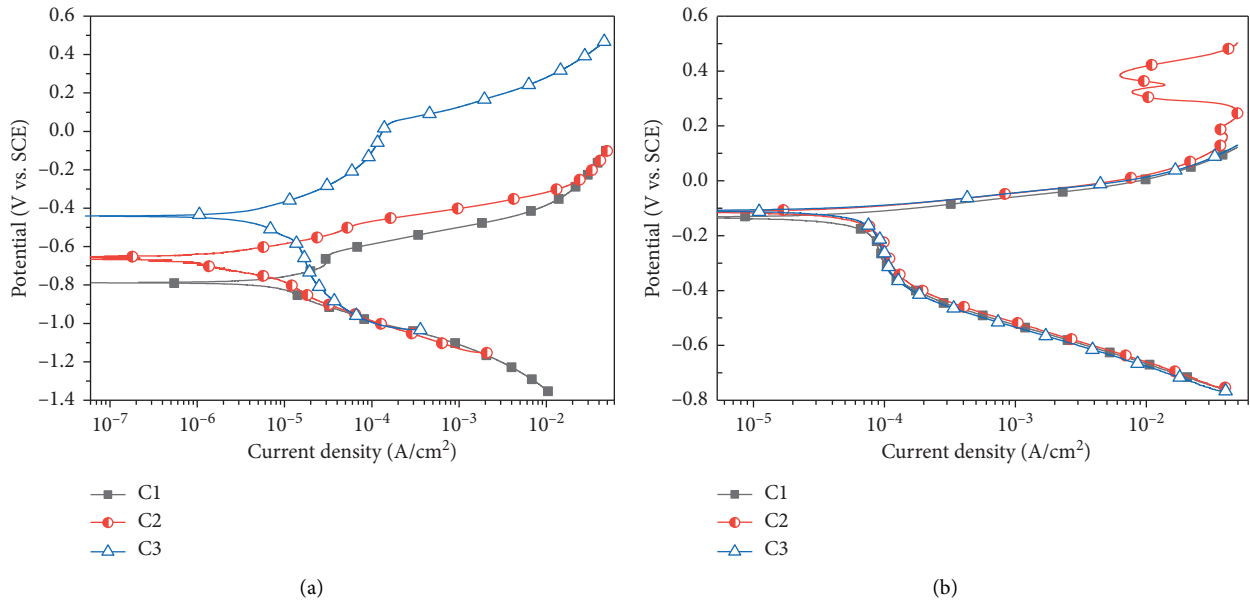


FIGURE 9: Potentiodynamic polarization curves of as-prepared Ni45 coatings in (a) 0.5 M NaCl and (b) 0.5 M NaCl + 0.5 M H₂SO₄ solutions.

TABLE 2: Corrosion current density (i_{corr}) and corrosion potential (E_{corr}) of as-prepared Ni45 coatings in 0.5 M NaCl and 0.5 M NaCl + 0.5 mol/L H₂SO₄ solutions.

Coatings	0.5 M NaCl		0.5 M NaCl + 0.5 M H ₂ SO ₄	
	E_{corr} (mV _{SCE})	i_{corr} ($\mu\text{A}\cdot\text{cm}^{-2}$)	E_{corr} (mV _{SCE})	i_{corr} ($\mu\text{A}\cdot\text{cm}^{-2}$)
C1	-786.7 ± 9.8	8.40 ± 0.21	-133.6 ± 2.7	68.01 ± 1.78
C2	-666 ± 8.3	5.62 ± 0.14	-113.2 ± 2.4	63.15 ± 1.58
C3	-441.2 ± 5.5	3.74 ± 0.11	-109.3 ± 2.3	56.97 ± 1.46

improvement in corrosion resistance [26, 28, 36–39]. However, the characteristics of Nyquist plots in 0.5 M NaCl + 0.5 M H₂SO₄ solution (Figure 10(b)) are different from those in 0.5 M NaCl solution (Figure 10(a)), which exhibited capacitive impedance arcs with smaller radius but fewer discrepancies among all three coatings, suggesting deteriorated but undifferentiated corrosion resistance. The EIS results are consistent with those of potentiodynamic polarization tests (Figure 9 and Table 2).

The above effects of laser scanning speed on corrosion resistance should be related to the microstructure evolution of Ni45 coatings. It has been reported that the formation of Cr-rich precipitated phases can cause Cr depletion in the matrix around these precipitates, deteriorating the corrosion resistance in these regions [40–43]. Lei et al. [26] studied the corrosion resistance properties of carbon fiber (CF) reinforced Ni-based composite coating by laser cladding. The results showed that the addition of CFs decreased the amount of M₇C₃ and M₂₃C₆ carbides, restraining the formation of Cr-depleted regions at the grain boundaries, thus improving the corrosion resistance of Ni-based alloy composite coatings. Accordingly, the schematic diagrams illustrating the corrosion mechanisms of Ni45 coatings in 0.5 M NaCl and 0.5 M NaCl + 0.5 M H₂SO₄ solutions are exhibited in Figures 11(a) and 11(b), respectively. In 0.5 M

NaCl solution (Figure 11(a)), the precipitate and coatings acted as the cathodes due to their nobler potential, while the Cr-depleted zone around the precipitates with lower potential acted as the anode [40, 42]. In this case, the Cr-depleted zone dissolved faster than the other zones because of the corrosion microcell, and some precipitates fell off from the matrix. When the laser scanning speed was low, there was relatively sufficient time for the reaction between Cr and C element, and more M₂₃(C,B)₆ formed and grew (Figure 6) leading to severer depletion of Cr around the precipitates. In contrast, less and even no M₂₃(C,B)₆ precipitates formed at higher laser scanning speeds owing to the faster cooling rate (Figure 6). As a result, the Cr-depleted zone and the corresponding corrosion microcell were diminished, which inhibited the corrosion process to some extent. Nonetheless, this inhibition effect of laser scanning speed on corrosion resistance did not exhibit tangible influence in the 0.5 M NaCl + 0.5 M H₂SO₄ solution, as shown in Figure 11(b). It is expected that both the anodic and cathodic reactions will accelerate in strong acidic solutions. In this case, all the regions on the surface, including the matrix, precipitates, and the Cr-depleted zones, dissolved rapidly, implying that the coating surface corroded uniformly layer by layer (Figure 11(b)). As a consequence, the effect of corrosion microcell on the local fall-off of precipitates was eliminated. Therefore, the laser scanning speed had less effect on the corrosion resistance of Ni45 coatings.

The mechanism shown in Figure 11(a) can be further verified by the variation trend of E_{corr} and i_{corr} with laser scanning speed (Figure 9 and Table 2), which is explained by the means of the mixed potential theory as illustrated in Figure 12 [44, 45]. According to the analyses in Figure 11, the effect of laser scanning speed on corrosion resistance was dominated by selective dissolution of Cr-depleted zone, which suggests that the anodic rather than the cathodic

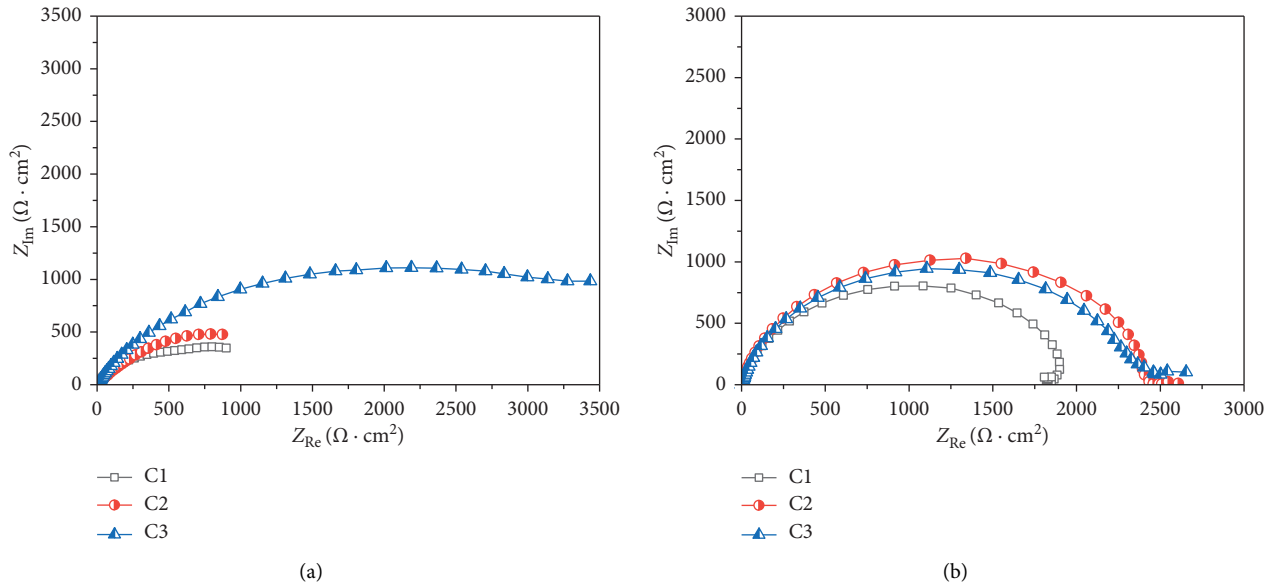


FIGURE 10: Nyquist plots of as-prepared Ni45 coatings in (a) 0.5 M NaCl and (b) 0.5 M NaCl + 0.5 M H₂SO₄ solutions.

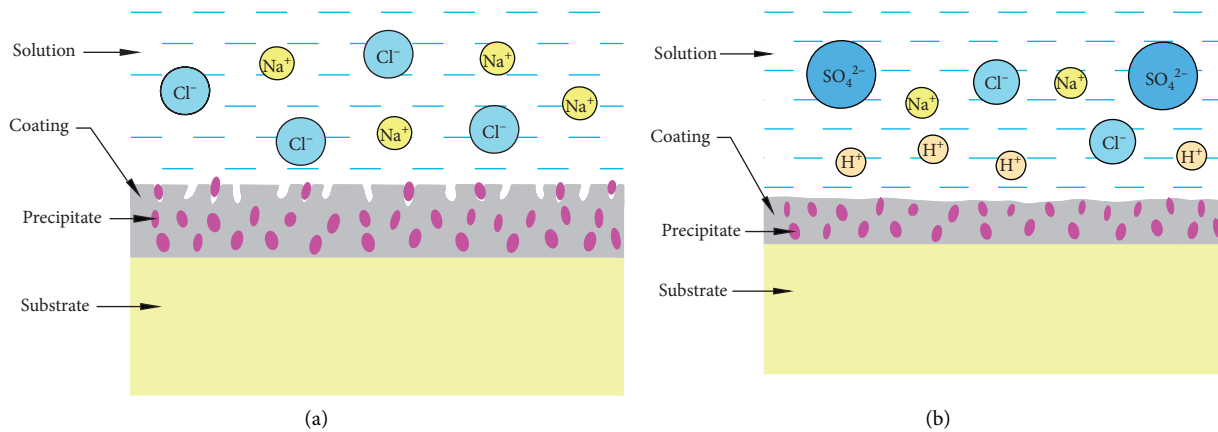


FIGURE 11: Schematic diagrams of the corrosion mechanisms for laser cladding process prepared Ni45 coatings in (a) 0.5 M NaCl and (b) 0.5 M NaCl + 0.5 M H₂SO₄ solutions.

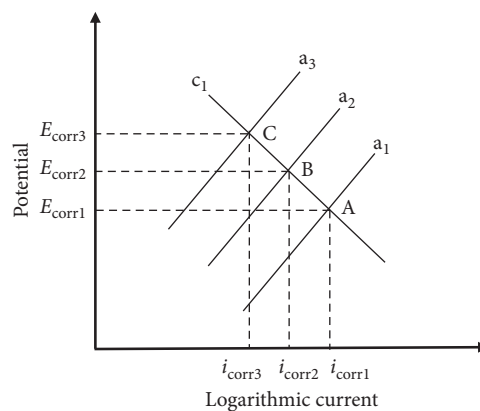


FIGURE 12: Schematic illustration of ideal polarization curves of C1 (point A, $E_{\text{corr}1}$ and $i_{\text{corr}1}$), C2 (point B, $E_{\text{corr}2}$ and $i_{\text{corr}2}$), and C3 (point C, $E_{\text{corr}3}$ and $i_{\text{corr}3}$) coatings in 0.5 M NaCl solution. The symbol c_1 represents the cathodic polarization curve of all the coatings, and the symbols a_1 , a_2 , and a_3 represent the anodic polarization curves of C1, C2, and C3 coatings, respectively.

reaction rate should differ at various laser scanning speeds. It correlates well with the fact that the difference in anodic curves was more noticeable compared with that in the cathodic curves in 0.5 mol/L NaCl solution as shown in Figure 9(a). Therefore, only one oblique line (c_1) is used to represent the unchanged cathodic curve, while three lines (a_1 , a_2 , and a_3) are used to represent the evolved anodic curves at various laser scanning speeds in Figure 12. The point A, the intersection of cathodic curve c_1 and anodic curve a_1 , is assumed to be the electrochemical corrosion state of C1 coating (laser scanning speed of 4 mm/s), at which the corrosion potential and corrosion current density are $E_{\text{corr}1}$ and $i_{\text{corr}1}$, respectively. On increasing the laser scanning speed to 6 mm/s (C2 coating) and 10 mm/s (C3 coating), less amount of $M_{23}(\text{C,B})_6$ precipitates formed and the Cr-depleted zones were diminished, consequently leading to inhibited anodic reactions. As a result, the anodic curve will move left along with the axis of current density, from a_1 to a_2 and a_3 , whose intersections are point B ($E_{\text{corr}2}$ and $i_{\text{corr}2}$) and point C ($E_{\text{corr}3}$ and $i_{\text{corr}3}$), respectively. Evidently, $E_{\text{corr}1} < E_{\text{corr}2} < E_{\text{corr}3}$, while $i_{\text{corr}1} > i_{\text{corr}2} > i_{\text{corr}3}$. The orders for corrosion potential and corrosion current density are identical to those identified in Table 2. Therefore, it should be reasonable to conclude that the improved corrosion resistance of Ni45 coatings in 0.5 M NaCl solution is attributed to the inhibited formation of $M_{23}(\text{C,B})_6$ precipitates at higher laser scanning speeds.

4. Conclusions

Ni45 coatings with good interface bonding have been prepared by the laser cladding process. The effects of laser scanning speed (4 mm/s, 6 mm/s, and 10 mm/s) on the microstructure, microhardness, and corrosion resistance of the as-prepared Ni45 coatings are clarified and explained:

- (1) The thickness of the transition layer between the coating and HAZ decreased the transformation from planar crystals to dendrites, and the grain refinements in the coatings were promoted. The formation and growth of $M_{23}(\text{C,B})_6$ precipitates in the coatings were inhibited with increasing laser scanning speed due to lower thermal input and faster cooling rate.
- (2) The microhardness of all the coatings presents a downward trend with the increase in laser scanning speed, which is attributed to the weakened precipitation strengthening resulting from the reduced amount of $M_{23}(\text{C,B})_6$ precipitates. Inside the coating, two distinct layers were identified with different microhardness. The position of the layer with the highest microhardness depended on the laser scanning speed. The competition between precipitation strengthening and grain refinement strengthening accounted for the microhardness distribution in the cross section of the coatings at various laser scanning speeds.
- (3) The laser scanning speed exhibited a promotion effect on the corrosion resistance of the as-prepared

Ni45 coatings in 0.5 M NaCl solution, whereas no effects could be identified in 0.5 M NaCl+0.5 M H_2SO_4 solution. The former is ascribed to the inhibited formation of Cr-depleted zones around the $M_{23}(\text{C,B})_6$ precipitates at higher laser scanning speeds. In contrast, this inhibition effect was invalid in the presence of 0.5 M H_2SO_4 because of the highly corrosive feature of the acid solution.

Data Availability

The data used to support the findings of this study are available from the corresponding author upon request.

Conflicts of Interest

The authors declare that they have no conflicts of interest.

Acknowledgments

The authors would like to express their gratitude for the financial support of the National Natural Science Foundation of China (Nos. 51801218, 51911530211, and 51905110) and the Natural Science Foundation of Jiangsu Province (Grant no. BK20191458).

References

- [1] Z. P. Shi, Z. B. Wang, F. G. Chen et al., "Cavitation erosion and corrosion behavior of NiTi cladding with Cu and Nb interlayers," *Journal of Materials Engineering and Performance*, vol. 29, no. 6, pp. 3840–3851, 2020.
- [2] Z.-P. Shi, Z.-B. Wang, J.-Q. Wang et al., "Effect of Ni interlayer on cavitation erosion resistance of NiTi cladding by Tungsten Inert Gas (TIG) surfacing process," *Acta Metallurgica Sinica*, vol. 33, no. 3, pp. 415–424, 2020.
- [3] J. L. Chen, J. Li, R. Song, L. L. Bai, J. Z. Shao, and C. C. Qu, "Effect of the scanning speed on microstructural evolution and wear behaviors of laser cladding NiCrBSi composite coatings," *Optics & Laser Technology*, vol. 72, pp. 86–99, 2015.
- [4] C. T. Kwok, H. C. Man, F. T. Cheng, and K. H. Lo, "Developments in laser-based surface engineering processes: with particular reference to protection against cavitation erosion," *Surface and Coatings Technology*, vol. 291, pp. 189–204, 2016.
- [5] X.-B. Liu, X.-J. Meng, H.-Q. Liu et al., "Development and characterization of laser clad high temperature self-lubricating wear resistant composite coatings on Ti-6Al-4V alloy," *Materials & Design*, vol. 55, pp. 404–409, 2014.
- [6] Z. Chen, H. Yan, P. Zhang, Z. Yu, Q. Lu, and J. Guo, "Microstructural evolution and wear behaviors of laser-clad Stellite 6/NbC/h-BN self-lubricating coatings," *Surface and Coatings Technology*, vol. 372, pp. 218–228, 2019.
- [7] Z. Zhang and R. Kovacevic, "Laser cladding of iron-based erosion resistant metal matrix composites," *Journal of Manufacturing Processes*, vol. 38, pp. 63–75, 2019.
- [8] X. Li, C. H. Zhang, S. Zhang et al., "Manufacturing of Ti_3SiC_2 lubricated Co-based alloy coatings using laser cladding technology," *Optics & Laser Technology*, vol. 114, pp. 209–215, 2019.
- [9] Q. Wu, W. Li, N. Zhong, W. Gang, and W. Haishan, "Microstructure and wear behavior of laser cladding VC-Cr₇C₃ ceramic coating on steel substrate," *Materials & Design*, vol. 49, pp. 10–18, 2013.

- [10] L. Meng, W. Zhao, K. Hou et al., "A comparison of microstructure and mechanical properties of laser cladding and laser-induction hybrid cladding coatings on full-scale rail," *Materials Science and Engineering: A*, vol. 748, pp. 1–15, 2019.
- [11] R. A. R. Rashid, S. Palanisamy, H. Attar, M. Bermingham, and M. S. Dargusch, "Metallurgical features of direct laser-deposited Ti6Al4V with trace boron," *Journal of Manufacturing Processes*, vol. 35, pp. 651–656, 2018.
- [12] G. Telasang, J. Dutta Majumdar, G. Padmanabham, M. Tak, and I. Manna, "Effect of laser parameters on microstructure and hardness of laser clad and tempered AISI H13 tool steel," *Surface and Coatings Technology*, vol. 258, pp. 1108–1118, 2014.
- [13] Y.-h. Cheng, R. Cui, H.-z. Wang, and Z.-t. Han, "Effect of processing parameters of laser on microstructure and properties of cladding 42CrMo steel," *The International Journal of Advanced Manufacturing Technology*, vol. 96, no. 5–8, pp. 1715–1724, 2018.
- [14] M. N. Fesharaki, R. Shoja-Razavi, H. A. Mansouri, and H. Jamali, "Microstructure investigation of Inconel 625 coating obtained by laser cladding and TIG cladding methods," *Surface & Coatings Technology*, vol. 353, pp. 25–31, 2018.
- [15] D. Tanigawa, N. Abe, M. Tsukamoto et al., "The effect of particle size on the heat affected zone during laser cladding of Ni-Cr-Si-B alloy on C45 carbon steel," *Optics and Lasers in Engineering*, vol. 101, pp. 23–27, 2018.
- [16] M. B. Henderson, D. Arrell, R. Larsson, M. Heobel, and G. Marchant, "Nickel based superalloy welding practices for industrial gas turbine applications," *Science and Technology of Welding and Joining*, vol. 9, no. 1, pp. 13–21, 2004.
- [17] S. Oukach, B. Pateyron, and L. Pawłowski, "Physical and chemical phenomena occurring between solid ceramics and liquid metals and alloys at laser and plasma composite coatings formation: a review," *Surface Science Reports*, vol. 74, no. 3, pp. 213–241, 2019.
- [18] C. Shi, J. Lei, S. Zhou, X. Dai, and L.-C. Zhang, "Microstructure and mechanical properties of carbon fibers strengthened Ni-based coatings by laser cladding: the effect of carbon fiber contents," *Journal of Alloys and Compounds*, vol. 744, pp. 146–155, 2018.
- [19] S. Sun, H. Fu, X. Ping et al., "Reinforcing behavior and microstructure evolution of NbC in laser clad Ni45 coating," *Applied Surface Science*, vol. 455, pp. 160–170, 2018.
- [20] Y. X. Qiao, Z. H. Tian, X. Cai et al., "Cavitation erosion behaviors of a nickel-free high-nitrogen stainless steel," *Tribology Letters*, vol. 67, no. 1, pp. 1–9, 2019.
- [21] K. Zhang, S. Wang, W. Liu, and X. Shang, "Characterization of stainless steel parts by laser metal deposition shaping," *Materials & Design*, vol. 55, pp. 104–119, 2014.
- [22] X. Jiao, J. Wang, C. Wang, Z. Gong, X. Pang, and S. M. Xiong, "Effect of laser scanning speed on microstructure and wear properties of T15M cladding coating fabricated by laser cladding technology," *Optics and Lasers in Engineering*, vol. 110, pp. 163–171, 2018.
- [23] X. Zhan, C. Qi, Z. Gao, D. Tian, and Z. Wang, "The influence of heat input on microstructure and porosity during laser cladding of Invar alloy," *Optics & Laser Technology*, vol. 113, pp. 453–461, 2019.
- [24] P. Tao, H. Li, B. Huang, Q. Hu, S. Gong, and Q. Xu, "The crystal growth, intercellular spacing and microsegregation of selective laser melted Inconel 718 superalloy," *Vacuum*, vol. 159, pp. 382–390, 2019.
- [25] K. Wang, D. Du, G. Liu, Z. Pu, B. Chang, and J. Ju, "Microstructure and mechanical properties of high chromium nickel-based superalloy fabricated by laser metal deposition," *Materials Science and Engineering: A*, vol. 780, Article ID 139185, 2020.
- [26] Y. X. Qiao, X. Cai, C. Ouyang, and Y. G. Zheng, "Effect of hydrogen on cavitation erosion behaviour of high strength steel," *International Journal of Electrochemical Science*, vol. 11, no. 12, pp. 10329–10346, 2016.
- [27] Z. Lei, N. Lu, and X. Yu, "Epitaxy and new stray grain formation mechanism during epitaxial laser melting deposition of Inconel 718 on directionally solidified nickel-based superalloys," *Journal of Manufacturing Processes*, vol. 42, pp. 11–19, 2019.
- [28] X. He, R. G. Song, and D. J. Kong, "Microstructures and properties of Ni/TiC/La₂O₃ reinforced Al based composite coatings by laser cladding," *Optics & Laser Technology*, vol. 117, pp. 18–27, 2019.
- [29] W. Gao, C. Chang, G. Li et al., "Study on the laser cladding of FeCrNi coating," *Optik*, vol. 178, pp. 950–957, 2019.
- [30] D. Kesavan and M. Kamaraj, "The microstructure and high temperature wear performance of a nickel base hardfaced coating," *Surface and Coatings Technology*, vol. 204, no. 24, pp. 4034–4043, 2010.
- [31] H. Liu, P. Chen, H. Yang et al., "Processing window and microstructure of NiCoCrAlY coating deposited on cast iron using multilayer laser cladding," *Journal of Spectroscopy*, vol. 2019, Article ID 9308294, 15 pages, 2019.
- [32] Y. Yang, J. B. Zhan, Z. Z. Sun et al., "Evolution of functional properties realized by increasing laser scanning speed for the selective laser melting fabricated NiTi alloy," *Journal of Alloys and Compounds*, vol. 804, pp. 220–229, 2019.
- [33] G. Q. Liu, X. L. Zhang, X. Y. Wang, and Y. X. Qiao, "Precipitation behavior of the topologically close-packed phase in the DD5 superalloy during long-term aging," *Scanning*, vol. 2020, Article ID 2569837, 6 pages, 2020.
- [34] H. Chen and D. Kong, "Effects of laser remelting speeds on microstructure, immersion corrosion, and electrochemical corrosion of arc-sprayed amorphous Al-Ti-Ni coatings," *Journal of Alloys and Compounds*, vol. 771, pp. 584–594, 2019.
- [35] M. Tavoosi and A. Barahimi, "Corrosion behavior of amorphous-nanocrystalline Fe-Ni-Cr electrodeposited coatings," *Surfaces and Interfaces*, vol. 8, pp. 103–111, 2017.
- [36] H. Shi, Y. X. Qiao, X. Cai et al., "Corrosion behavior of high-nitrogen stainless steel in NaCl solution," *International Journal of Electrochemical Science*, vol. 12, no. 12, pp. 11298–11308, 2017.
- [37] Q. N. Song, N. Xu, W. Gu et al., "Investigation on the corrosion and cavitation erosion behaviors of the cast and friction stir processed Ni-Al bronze in sulfide-containing chloride solution," *International Journal of Electrochemical Science*, vol. 12, no. 11, pp. 10616–10632, 2017.
- [38] Y. Qiao, J. Chen, H. Zhou et al., "Effect of solution treatment on cavitation erosion behavior of high-nitrogen austenitic stainless steel," *Wear*, vol. 424–425, pp. 70–77, 2019.
- [39] S. Sinhmar and D. K. Dwivedi, "Effect of weld thermal cycle on metallurgical and corrosion behavior of friction stir weld joint of AA2014 aluminium alloy," *Journal of Manufacturing Processes*, vol. 37, pp. 305–320, 2019.
- [40] Y. X. Qiao, D. K. Xu, S. Wang et al., "Effect of hydrogen charging on microstructural evolution and corrosion behavior of Ti-4Al-2V-1Mo-1Fe alloy," *Journal of Materials Science & Technology*, vol. 60, pp. 168–176, 2021.
- [41] E. Bettini, T. Eriksson, M. Boström, C. Leygraf, and J. Pan, "Influence of metal carbides on dissolution behavior of

- biomedical CoCrMo alloy: SEM, TEM and AFM studies,” *Electrochimica Acta*, vol. 56, no. 25, pp. 9413–9419, 2011.
- [42] Y. Yin, R. G. Faulkner, P. Moreton, I. Armson, and P. Coyle, “Grain boundary chromium depletion in austenitic alloys,” *Journal of Materials Science*, vol. 45, no. 21, pp. 5872–5882, 2010.
- [43] H.-J. Kim, S.-H. Jeon, S.-T. Kim et al., “Investigation of the sensitization and intergranular corrosion of tube-to-tubesheet welds of hyper duplex stainless steel using an electrochemical reactivation method,” *Corrosion Science*, vol. 87, pp. 60–70, 2014.
- [44] Y. X. Qiao, X. Cai, J. Cui, and H. B. Li, “Passivity and semiconducting behavior of a high nitrogen stainless steel in acidic NaCl solution,” *Advances in Materials Science and Engineering*, vol. 2016, Article ID 6065481, 9 pages, 2016.
- [45] Y. Zheng, S. Luo, and W. Ke, “Effect of passivity on electrochemical corrosion behavior of alloys during cavitation in aqueous solutions,” *Wear*, vol. 262, no. 11-12, pp. 1308–1314, 2007.

Research Article

A Simple Way to Achieve Self-Cleaning Surfaces with Unique Antifouling Property

Caizhen Yao ¹, Shizhen Xu ^{1,2}, Xiaodong Jiang,¹ Jiaxuan Chen,³ and Xiaodong Yuan ¹

¹Laser Fusion Research Center, CAEP, P.O. Box 919-988-5, Mianyang 621900, China

²School of Physical Electronics, University of Electronic Science and Technology of China, Chengdu 610054, China

³Harbin Institute of Technology, Harbin 150001, China

Correspondence should be addressed to Caizhen Yao; yaocaizhen2008@126.com and Xiaodong Yuan; yxd66my@163.com

Received 5 May 2020; Accepted 29 June 2020; Published 31 July 2020

Guest Editor: Zhen He

Copyright © 2020 Caizhen Yao et al. This is an open access article distributed under the Creative Commons Attribution License, which permits unrestricted use, distribution, and reproduction in any medium, provided the original work is properly cited.

Self-cleaning surfaces may have wide applications such as microfluidic devices, lab-on-a-chip, sensors, microreactors, air purification, and antimicrobial fields. In this article, by using a combination of femtosecond (fs) laser irradiation and fluorination technique, self-cleaning stainless steel surfaces with unique antifouling property were obtained. New insight is developed through a detailed analysis of the antifouling behavior of the self-cleaning surfaces. The surface free energy and its polar and disperse components were calculated by using the Owens–Wendt–Rabel–Kaelble (OWRK) method. X-ray photoelectron spectroscopy was employed to analyse the surface elemental compositions and functional groups. The antifouling property of the surface was recorded by using a high speed camera. Water sliding angles (SAs) were reduced by fluorination treatment, resulting in low adhesive superhydrophobic surfaces with the self-cleaning property. The influences of micro/nanostructures, fluorination, and their combination on the surface free energy were investigated. The interaction process between water droplets and pollutants (inorganic and organic particles) on the treated surface was explored. The antifouling property of an optimized specimen (CA = 162° and SA = 1°) was tested and compared with the untreated sample.

1. Introduction

Contaminants on surfaces may threaten the health of people and the quality of products. Cleaning methods, e.g., swiping, ultrasonic cleaning, illuminating, and water spraying have been used to maintain surface cleanliness, which consumes labor, energy, capital, and time. Recently, surface treatment with self-cleaning properties has generated worldwide interest [1, 2]. These surfaces are of great importance not only for the fundamental research but also for various practical applications. Antifouling paints/coatings are normally applied to metallic surfaces by using electrospinning [2, 3], spraying [4], vapor deposition [5], or electrochemical deposition [6]. These paints/coatings have good self-cleaning property. However, their disadvantages of low adhesion, poor temperature resistance, and discoloration due to weathering or mechanical damaging severely limit their application in extreme conditions. Inspired by lotus leaf,

self-cleaning property can be obtained by surface micro/nanostructuring. Water droplets pick up dirt particles and debris from a tilt surface and roll-off to realize self-cleaning [2, 7]. Metallic surfaces with self-cleaning property have huge potential applications in microfluidic devices, lab-on-a-chip, sensors, microreactors, air purification, and antimicrobial fields [8]. For example, as the interior surfaces, the washing process for pipelines of milk or petroleum can be greatly simplified. The exterior surfaces would be cleaned by rain water without using detergent, saving the maintenance, and labor costs [2]. Furthermore, ships' body can be better protected due to the low adhesion of biological pollutants [9].

Femtosecond (fs) laser technique has proved to be a promising method to produce micro/nanostructures on surfaces for its unique abilities and advantages, including the following. (1) This is a maskless technique with 0–3 dimensional micro/nanoscale structures being able to form

simultaneously [10]. (2) It can be applied to a variety of materials such as polymers [11–15], metals [10, 16–19], and semiconductors [7] in various environments (e.g., air [7, 12–14, 16–18], gaseous atmosphere [20], vacuum, and liquid environments [10]). (3) Precise micro/nanostructure can be realized by controlling laser parameters and/or environments to fine-tune the surface wettability and adhesive property [9, 21]. (4) It has minimum thermal effect so that the property of substrate can be preserved [22, 23]. Despite its infancy, the outstanding micro/nanostructure fabrication of femtosecond laser has been raised worldwide attention, including Wolter from Laser Zentrum Hannover e.V. [19], Jeon from KIST Korea [11], Guo from University of Rochester [24, 25], Hatzikiriakos from UBC Canada [16], Li from USTC China [10], Chen from Xi'an Jiaotong University [7, 13, 15, 26], and Zhong from Tsinghua University [17]. In his review article, Chen et al. [26] pointed out that laser microfabrication can realize special modulation ranging from superhydrophilic to superhydrophobic, allowing much more freedom to achieve complex multiple-wettability integration. Zhang et al. [7] adopted femtosecond laser irradiation technique to achieve the tunable adhesive superhydrophobic silicon surfaces and revealed that the adhesive forces of as-prepared surfaces can be tuned by varying the area ratio of superhydrophobic domain to hydrophobic domain. Jun et al. [11] generated microscale grooves on nanofibrous platforms using a femtosecond laser ablation process to develop engineered fibrous platforms with patterned hierarchical topographies. The fabricated platforms can regulate cellular adhesive morphology, proliferation, and distinct distribution of focal adhesion proteins. By tailoring the surface chemical composition and surface morphology, Moradi et al. [16] reported the effect of extreme surface wettability on platelet adhesion and activation in SS and Ti surfaces. Li et al. [10] reported the assembly of self-organized 3-dimensional porous metal micro/nanocages arrays on nickel surface by ethanol-assisted femtosecond laser irradiation. The underlying formation mechanism was also investigated. The 3D cage-like micro/nanostructures exhibit not only improved antireflection property but also enhanced hydrophobicity. However, the interaction behaviour and mechanism between water droplets and pollutants on self-cleaning surfaces were seldom reported.

In this paper, superhydrophobic surfaces were obtained by using one-step femtosecond laser irradiation. Its surface free energy was greatly reduced by a fluorination process to achieve excellent self-cleaning property. Surface morphologies, surface functional groups, surface free energy, static wettability, and dynamic wettability were characterized. The interaction behavior between water droplets and pollutants on self-cleaning stainless steel (SS) was investigated. The self-cleaning mechanism was also explored. This paper aims to bridge the gap between superhydrophobic surface and self-cleaning surface.

2. Experimental Process

2.1. Samples Preparation. Experiments were performed in a clean room at 23°C in ambient atmosphere. Mirror-like 304

SS coupons with a dimension of 20 mm × 20 mm × 2 mm were used as substrates. The schematic of experimental setting up can be referred to a previous study [27]. In brief, a commercial Ti:sapphire chirped-pulse amplification laser system (Spectra Physics) was used to generate a 35 fs horizontally linear polarized laser with a central wavelength of 800 nm. The beam has a Gaussian profile. A neutral density (ND) attenuator was used to adjust the pulse energy. Femtosecond laser pulses were focused to e^{-2} spot diameter of 300 μm by using a 150 mm focal length lens. Substrates were mounted perpendicular to the laser beam on a precision computer-controlled 3D translation stage. The laser repetition rate is 1 kHz. The pulse number per spot was controlled by the combination of an electric shutter and the speed of translation stage. Laser scan irradiation mode was employed to get large and uniform surface areas for anti-fouling property tests.

In order to evaluate the surface morphologies of samples over a range of experimental parameters, the influence of fluence ($F = 0.3, 0.5, 0.7, 1.0, 1.3, 1.5, 1.6, 1.9, 2.0$ J/cm², respectively) and pulse number per focal spot (PPS = 10, 20, 30, 100, 200, 300 pulses, respectively) were systematically investigated. After laser treatment, the fluorination process was performed to reduce surface free energy. Samples were cleaned by ultrasonic cleaning in water at 23°C for 10 min and then immersed into 1% fluoroalkylsilane (C₁₄H₁₉F₁₃O₃Si) solution for 30 min. The samples were immediately treated in a furnace at 135°C for 30 min. Mirror-like 304 SS coupons were fluorinated with the same procedure and tested for comparison purpose.

2.2. Characterization. Images of surface morphologies and microstructures were obtained by using a Phenom scanning electron microscope (SEM) with an accelerating voltage of 10 kV. Samples were sputter-coated with a 5 nm gold layer before observation. Contact angles (CAs) and surface free energy were characterized by using interface tension meter (Kruss K100). Owens-Wendt-Rabel-Kaelble (OWRK) method was employed to calculate surface free energy and its polar and disperse components. The disparity between water and hexadecane in the appearance of CA was due to the difference of surface tension. Hexadecane has a lower surface tension of $\gamma_{HD} = 26.7$ mN/m in comparison with that of water $\gamma_{H_2O} = 72.0$ mN/m. X-ray photoelectron spectroscopy (XPS) was used to test the surface elemental compositions and functional groups of specimens before and after fluorination. Al K α was used as X-ray source. A step-scan mode was used at the binding energy ranging from 0 to 1360 eV with an energy step size 1 eV. Water bouncing and rolling behaviors on specimens were recorded by using a high speed camera (Pro.1200 hs). The interaction between water droplets and pollutants on self-cleaning SS was also monitored.

3. Results and Discussion

3.1. Surface Morphology and Microstructure. Systematic investigation of femtosecond laser-induced micro/nanostructures

on 304SS was performed and a F-PPS model was built, which can be used to locate and fine-tune the laser settings to produce a specific surface microstructure in laser scan irradiation mode. As shown in Figure 1, two types of micro/nanostructures were observed: the laser-induced periodic surface structures (LIPSSs) on S1, S2, S3, and S4, and nodular structures on S5 and S6. LIPSSs on 304SS are located at F lower than 1 J/cm^2 . With increasing F , the nodular structures start to form. The two types of structures have different formation mechanism and different structure properties. This result is consistent with literatures [3, 11, 28], indicating that, at low fluences ($<1 \text{ J/cm}^2$), the ablation process is dominated by the optical penetration depth and, at high fluences ($\geq 1 \text{ J/cm}^2$), the electron heat diffusion length is the domination parameter. Interestingly, with increasing PPS from 5 pulses to 300 pulses at the same F , the structure types were kept almost the same. However, the dimensions of nodular structures increased dramatically, which may be due to the incubation effect [27, 29, 30]. Thus, in this F-PPS model, F determines the type of structures and PPS determines the dimensions of structures. This result is consistent with the numerical simulation results of Zhang et al. [31], who demonstrate that, according to the two-temperature model for multipulse laser irradiation, the lattice temperature will be much less affected if the time interval between two pulses is larger than the electron-lattice coupling time.

3.2. Surface Free Energy and Wettability Test. Surface free energy of a material is normally influenced by surface morphology and chemical composition. Their combined effects have been studied extensively. However, their respective influence on surface free energy and wettability of a material was seldom investigated, which is of great importance for the self-cleaning surface.

Table 1 and Figure 2 show the relations of surface free energies and CAs of specimens after femtosecond laser irradiation. The surface free energies vary significantly from $23.09 \pm 0.44 \text{ mN/m}$ to $60.12 \pm 0.17 \text{ mN/m}$ in comparison to the original 304SS ($42.22 \pm 1.98 \text{ mN/m}$). Tested surface free energy of S1 and S2 is lower than that of original 304SS, and it grows with increasing accumulated energy density. The water contact angle is slightly decreased with the increasing of surface free energy. S1 has a CA of about 152° , showing superhydrophobicity. S6 has a CA of about 9° , showing hydrophilicity. Similar results were reported by Pflöging et al. [32] on nanosecond laser irradiated titanium alloy. Low surface energy and decreased wettability may reduce the interaction between the metal surface and contaminants.

Table 2 and Figure 3 show the surface free energies are significantly reduced and CAs are greatly increased after fluorination. The surface free energy of fluorinated S1–S6 is much lower than that of 304SS (17.47 mN/m) with the same fluorination process. All specimens show near superhydrophobic property ($\sim 150^\circ$) while fluorinated 304SS has $\text{CA} = 103^\circ$. It can be concluded that proper micro/nanostructure fabrication and fluorination can be used to reduce surface free energy, and different micro/nanostructures have different fluorination effects.

According to the OWRK method, surface free energy is composed of disperse and polar components. Thus, a detailed analysis is performed on SS, S1, and S6 and their fluorinated samples FS, FS1, and FS6, to further understand the influence of fluorination on the free energy components. As shown in Table 3 and Figure 4, the values of polar component (P) and disperse component (D) of the three samples before fluorination follow the order of $P_{S1} < P_{SS} < P_{S6}$ and $D_{S1} < D_{SS} < D_{S6}$. P_{S1} and D_{S1} are significantly lower than those of original 304SS and S6. After fluorination, the polar component and disperse component of these samples were greatly reduced. Both P_{FS1} and P_{FS6} are so small that can be ignored in comparison with P_{FS} .

Polar component has significant effect on wettability. Polar molecules can enhance the wettability by interaction with dipole force and hydrogen bonds [32]. Thus, before fluorination, the water contact angle of untreated 304SS is smaller than that of S1 and larger than that of S6. S1 shows superhydrophobicity due to the reduction of polar component. After fluorination, FS1 and FS6 show superhydrophobicity due to the elimination of polar component. FS6 has a lower surface free energy in comparison with FS1, which may be due to its large specific surface area. The deposition of more hydrophobic functional groups during the fluorination process can reduce the surface free energy of FS6. The relatively large polar component on FS can be used to explain why the fluorinated untreated 304SS surface does not have superhydrophobicity.

3.3. Surface Functional Groups and Adhesive Property.

The dynamic wettability of original 304SS, superhydrophobic S1, and hydrophilic S6 samples was investigated by using high speed camera in Figure 5. A water droplet of $8 \mu\text{l}$ fell from the same height above the tested surface. S1 shows the absolute water repelling property, and S6 shows much higher wettability in comparison with the original 304SS due to the different types and dimensions of micro/nanostructures as shown in Figure 1.

S1 has a CA of 152° ; however, it shows adhesive property (Figure 6(a)), which is unfavorable for the formation of self-cleaning surface. A self-cleaning surface should have a high water repelling property and a low adhesive property to contribute the water droplet rolling process [33]. After treated by a fluorination process, the adhesive force is greatly reduced as shown in Figure 6(b). XPS analysis of S1 in Figure 7 and Table 4 indicates that this may be related to the formation of hydrophobic functional groups, e.g., -C-F, -C-F₂, and -C-F₃. The peak position of F_{1s} locates at 688.9 eV . The atomic percent of -C-F₂ increases to 26.94% after fluorination. During the fluorination process, metallic bonds and -OH will be replaced by hydrophobic groups. Hydrophobic groups have less adhesive force to water droplets, which contribute to the self-cleaning property.

3.4. Wettability Models. Figure 8 shows the wettability model of SS, S1, and S6 before and after fluorination. It has been reported that micro/nanobinary structures on solid surfaces can effectively enhance hydrophobicity of the

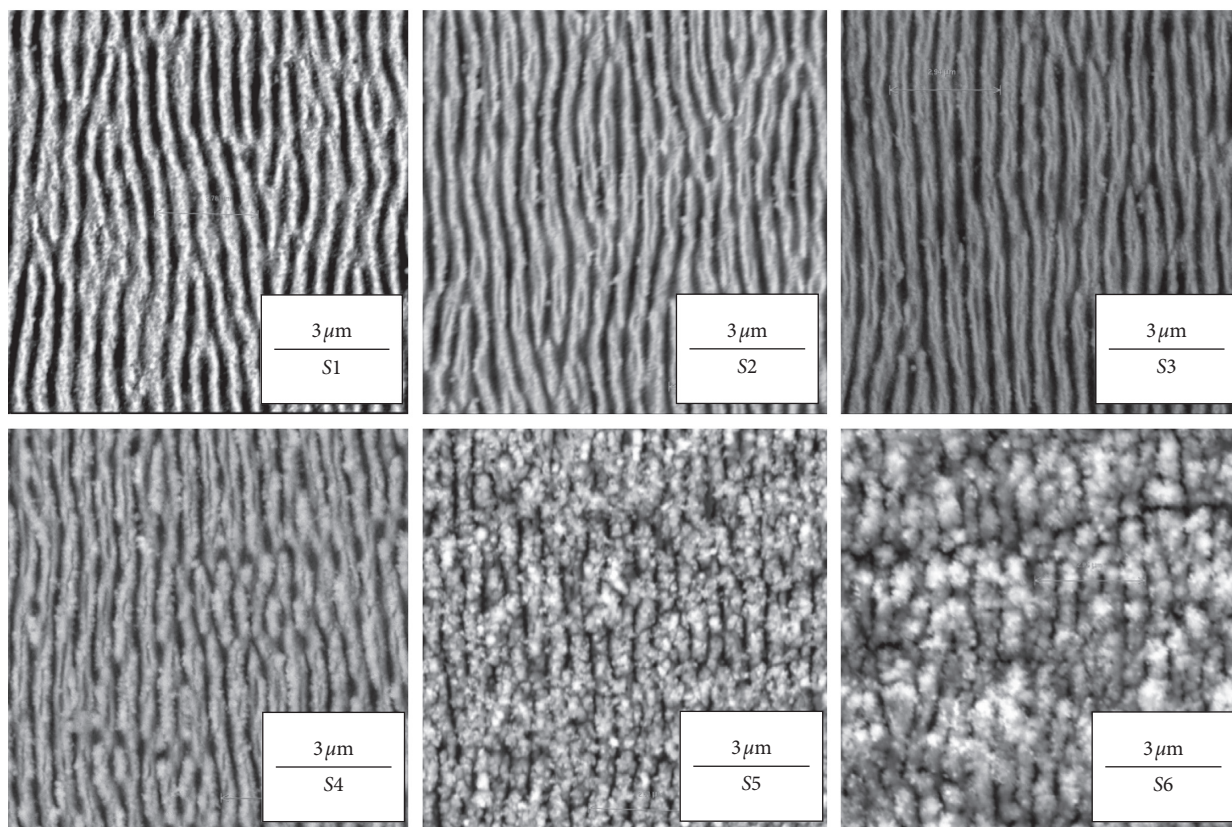
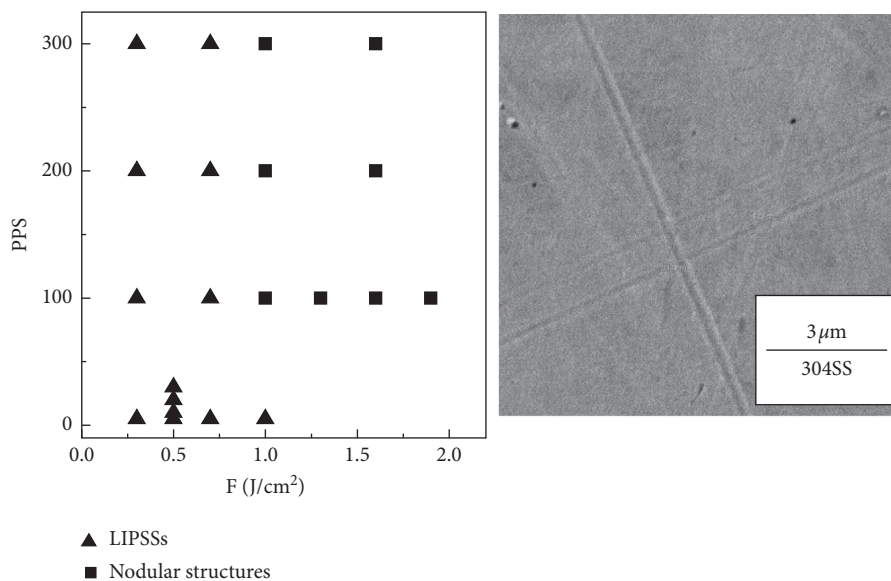


FIGURE 1: The influence of F and PPS on the evolution of surface morphology. PPS refers to the pulse number per focal spot and F refers to the pulse fluence. S1–S3 have the same $F = 0.5 \text{ J/cm}^2$ with increasing PPS = 5, 10, and 20 pulses, respectively, and S4–S6 have the same PPS = 100 pulses with increasing $F = 0.5, 1.5,$ and 2.0 J/cm^2 , respectively. Surface morphology of 304SS is also given for comparison purpose.

TABLE 1: Surface free energies and CAs of specimens after laser irradiation.

Samples	Surface free energy (mN/m)	Standard deviation	Water contact angle (°)	Standard deviation
304SS	42.22	1.98	83	0.41
S1	23.09	0.44	152	0.76
S2	33.20	0.17	145	0.72
S3	45.02	0.57	138	0.69
S4	50.00	0.50	127	0.69
S5	59.56	0.21	11	0.05
S6	60.12	0.17	9	0.04

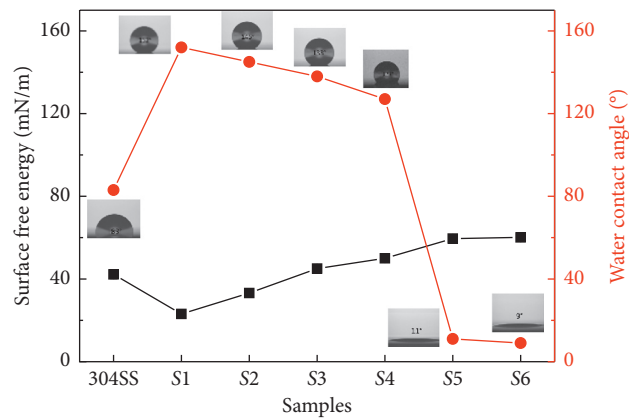


FIGURE 2: Comparison of surface free energies and water contact angles of specimens after femtosecond laser irradiation.

TABLE 2: Surface free energies and CAs of laser-treated specimens after fluorination.

Samples	Surface free energy (mN/m)	Standard deviation	Water contact angle (°)	Standard deviation
304SS	17.47	1.29	103	0.55
S1	5.15	0.09	162	0.81
S2	3.13	0.16	160	0.80
S3	1.96	0.42	144	0.72
S4	2.55	0.14	151	0.75
S5	0.94	0.05	146	0.73
S6	2.37	0.23	150	0.75

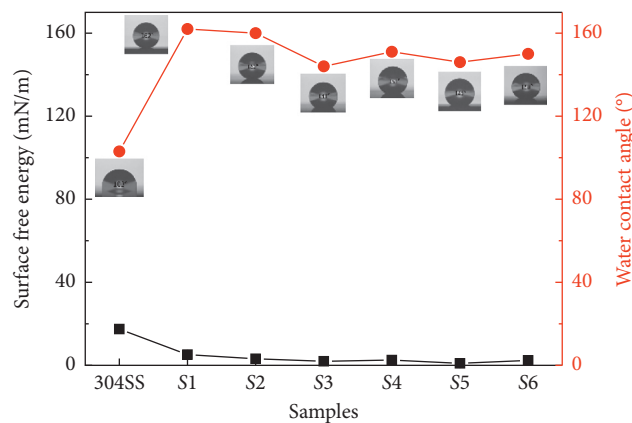


FIGURE 3: Surface free energies and CAs of laser-treated specimens after fluorination.

TABLE 3: Surface free energy and disperse and polar values before and after fluorination.

Samples	Surface free energy (mN/m)	Disperse components (mN/m)	Polar components (mN/m)
SS	42.22 ± 1.98	31.40 ± 0.28	10.82 ± 1.70
FS	17.47 ± 1.29	13.85 ± 0.46	3.62 ± 0.84
S1	23.09 ± 0.44	20.58 ± 0.36	2.51 ± 0.08
FS1	5.15 ± 0.09	5.00 ± 0.08	0.14 ± 0.01
S6	60.12 ± 0.17	45.96 ± 0.12	14.17 ± 0.05
FS6	2.37 ± 0.23	2.34 ± 0.21	0.03 ± 0.02

SS: untreated stainless steel, FS: fluorinated SS, FS1: fluorinated S1, and FS6: fluorinated S6.

surfaces [34, 35], giving the corroboration for the difference of hydrophobicity between the polished 304SS and laser treated surfaces. SS has a CA less than 90° due to the

existence of hydrophilic metallic bonds or hydroxyl groups. As shown in Figure 8(b), the superhydrophobicity of S1 comes from its microstructures (Figure 1) and can be

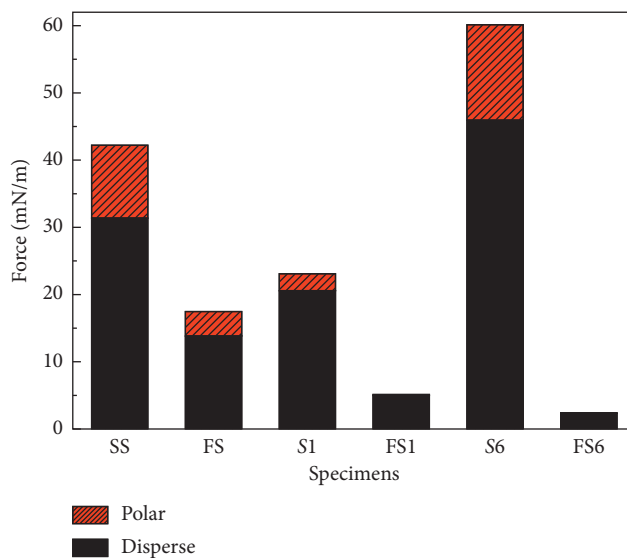


FIGURE 4: Disperse and polar components of surface free energy on specimens, showing both fluorination and micro/nanostructure are important for reducing surface free energy.

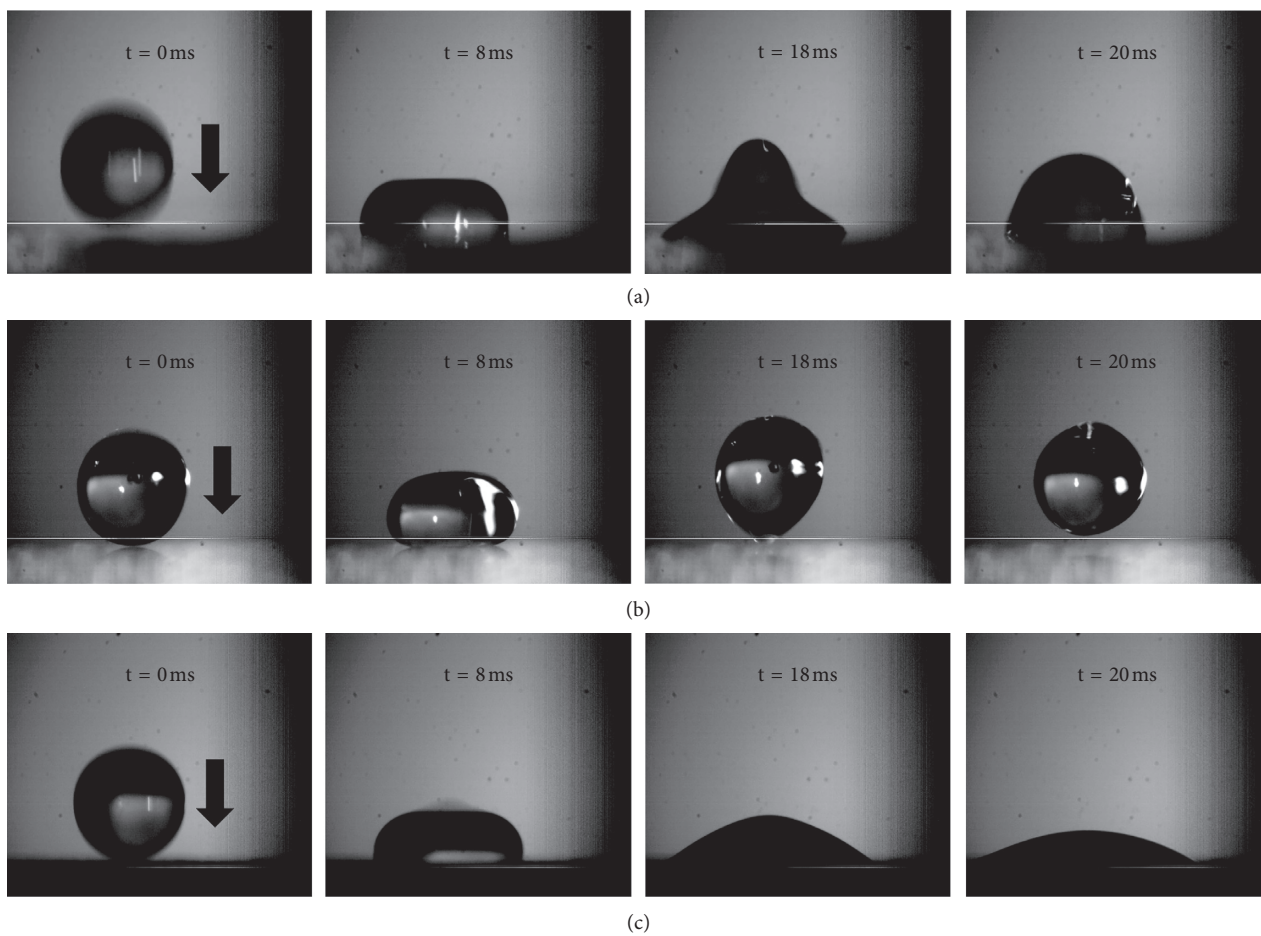


FIGURE 5: Dynamic behaviors of a falling water droplet on (a) original 304SS, (b) S1 with superhydrophobic property, and (c) S6 with hydrophilic property.

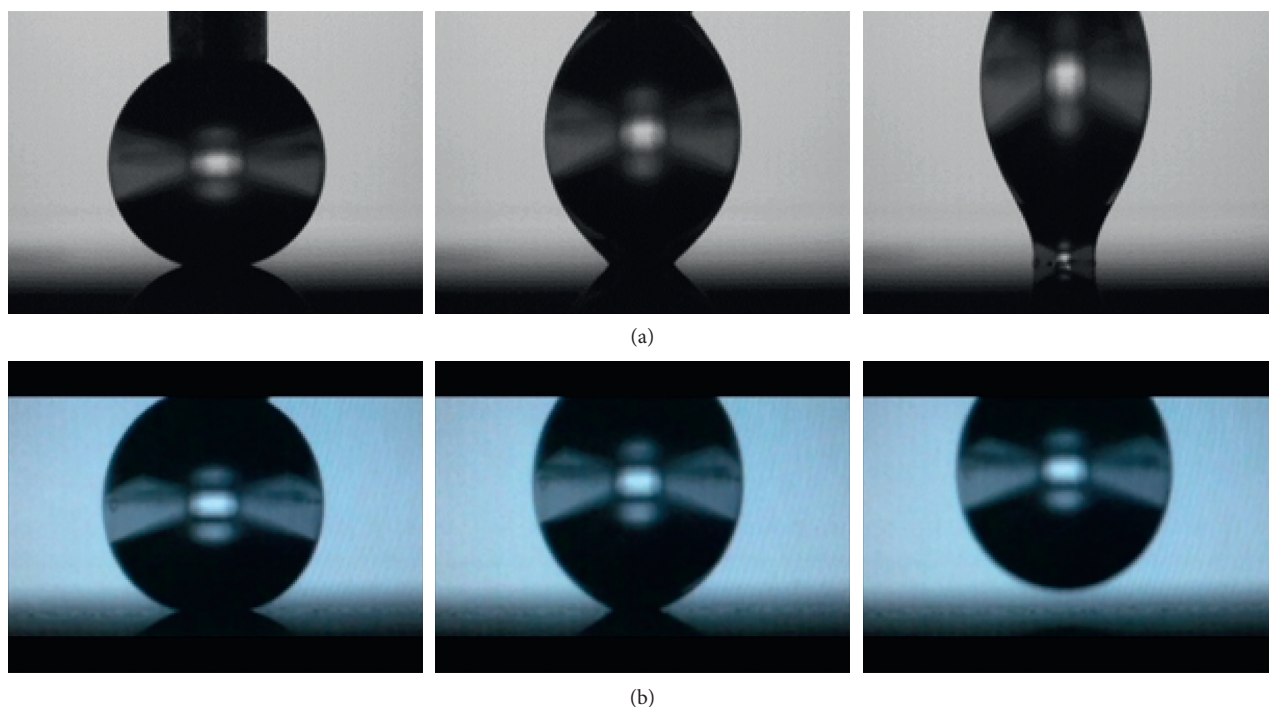


FIGURE 6: Adhesive property of S1: (a) before fluorination and (b) after fluorination.

explained by Cassie model [36]: when a water droplet is put on the surface of S1, the droplet will only contact with the protuberance of the LIPSSs, covered by hydrophilic metallic bonds or hydroxyl groups. Meanwhile, air bubbles are trapped in the bottom, greatly reducing the contact area between the water droplet and sample. The hydrophilic property of S6 may be attributed to the growing of microstructures. In this case, the sample has a large surface area covered by hydrophilic metallic bonds or hydroxyl groups. Water will take the place of air and infiltrate into the microstructures as shown in Figure 8(c).

The three samples are further fluorinated as shown in Figures 8(d)–8(f). During the fluorination process, hydrophilic metallic bonds or hydroxyl groups are replaced by hydrophobic functional groups, which, combined with the trapped air bubbles, could be the reason for the excellent superhydrophobicity of FS1 and FS6. This result is consistent with literature [37]. The process of fluorination relies on the reaction of fluoroalkyl silane with -OH groups, leading to significant decrease in surface energy of sample. Moreover, heating in a furnace at 135°C may help to eliminate the surface hydroxyl groups, which could also be a reason for the hydrophilic-to-hydrophobic transition of samples.

3.5. Antifouling Modes. The interaction between water droplet and pollutant particle is crucial for the self-cleaning property. The most important adhesive forces between the pollutants and surface are the van der Waals' and electrostatic forces. The cleaning process requires a repelling force larger than the adhesive force. Thus, the surface free energy of a specimen must be controlled as small as possible. In this research, the interaction behaviors between water droplets

and different types of particulate pollutants on self-cleaning SS were monitored and recorded. Three types of antifouling modes were built.

Figure 9(a) is a series of photos taken by using a high speed camera, showing the “rolling” process of a water droplet on a contaminated surface. The surface is tilted with an angle of 5° to perform the rolling process. The water droplet has a volume of 8 μL and provides a shear force to the contaminant (a SiO_2 particle indicated by the white arrow). When the shear force is large enough to overcome the adhesive force between the contaminant and surface, the water droplet will lift the contaminant up from the surface. Figure 9(b) is a schematic of the rolling cleaning process.

Figure 10(a) is a series of photos taken by a high speed camera, showing the “rebounding” process of a water droplet on a contaminated surface, which is tilted for 5°. SiO_2 particles are indicated by white arrows. A water droplet with a volume of 8 μL came out from a needle, spreading on the surface, collected the contaminant from the surface, and rebounded back to the air. Interestingly, the “rebounding” mode has a much higher cleaning efficiency than the rolling mode due to the large spreading area of the water droplet, which depends on the initial energy of the droplet and the status of the surface. Figure 10(b) is a schematic of the “rebounding” process.

Figure 11(a) is the photos showing the contaminant absorbing process by a water droplet on a surface. Contaminants are sponge particles. A water droplet of 4 μL is suspended on the tip of a needle. When it is close to the contaminant particle, the particle is absorbed into the droplet due to the high surface tension. The water droplet does not need to contact with the surface to make it clean,

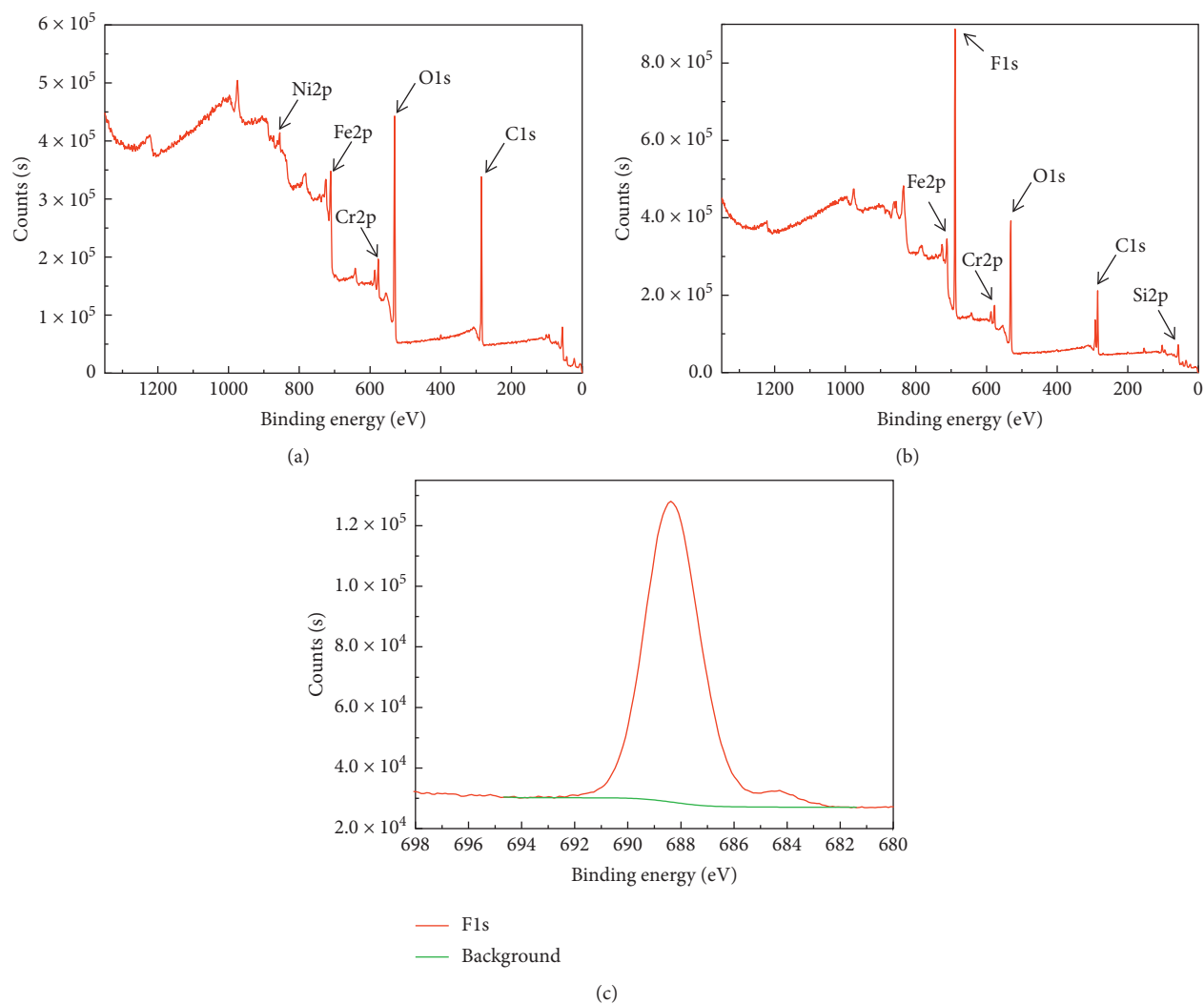


FIGURE 7: XPS diagrams of S1: (a) before fluorination, (b) after fluorination, and (c) F1s element.

TABLE 4: Surface elemental compositions and functional groups of S1 after fluorination (FS1).

Element	Functional group	Binding energy (eV)	Atomic (%)
C _{1s}	C—H	284.8	20.31
	C=O, C—F	287.8	2.29
	C—CO ₃ , CF ₂	290.8	7.96
	CF ₃	292.7	2.24
O _{1s}	Cr ₂ O ₃ , CrO ₃ , Fe ₂ O ₃ , Fe ₃ O ₄ , FeOOH	530.2	15.48
	OH	531.8	10.31
N _{1s}	N ₂ , NH ₃	400.0	0.62
	Metallic Fe	719.9	0.60
Fe _{2p}	Fe ³⁺	710.5	3.48
	FeOOH	711.5	4.04
Cr _{2p}	Cr ₂ O ₃	576.7	2.14
F _{1s}	CF ₂	688.9	26.94
Si _{2p}	Si—O	100.2	3.21

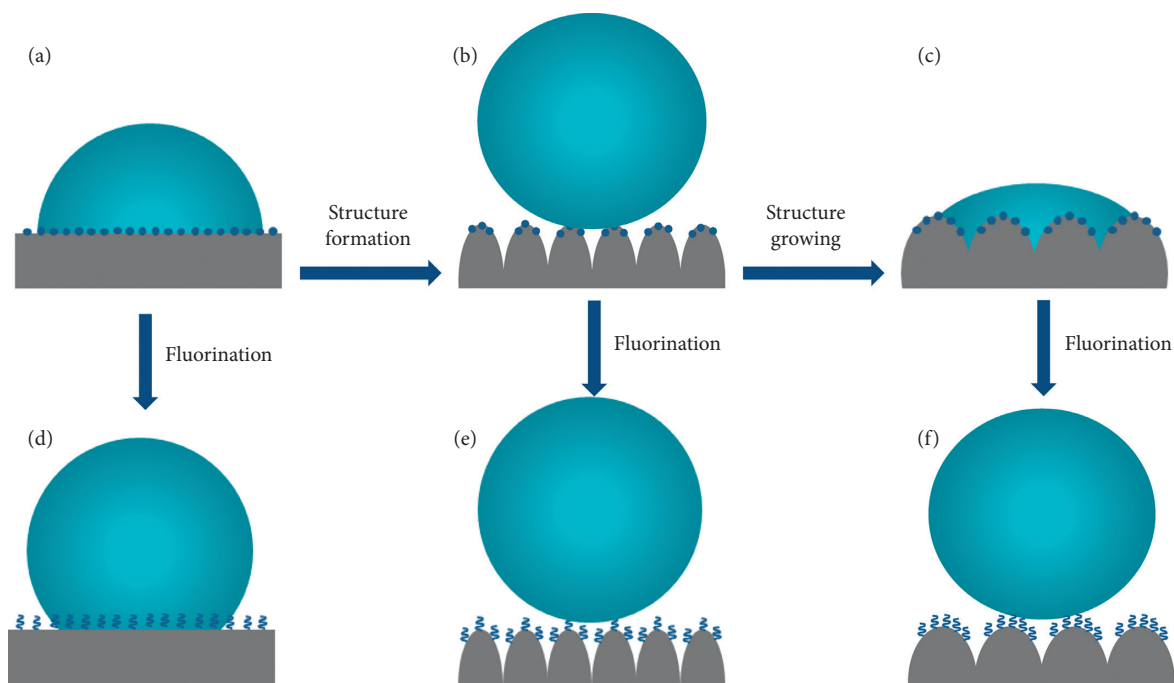


FIGURE 8: Wettability model of different specimens before and after fluorination. (a, d) SS, (b, e) S1, and (c, f) S6; ●: metallic bonds or hydroxyl groups and ㄿ: hydrophobic functional groups.

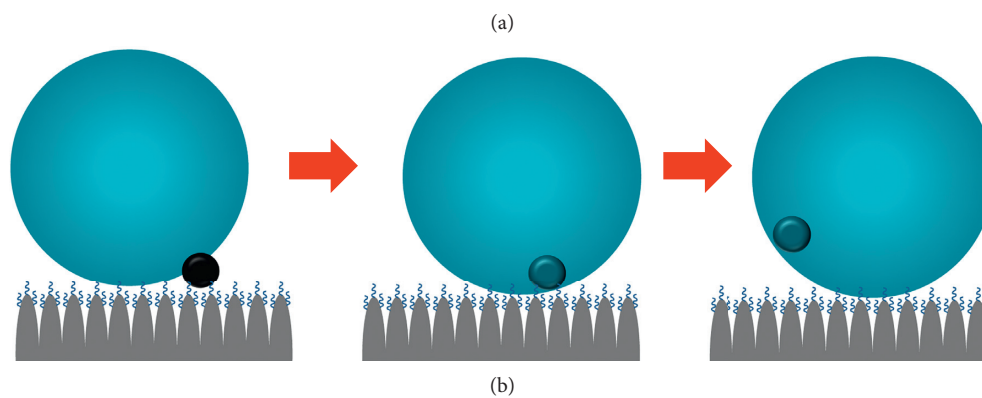
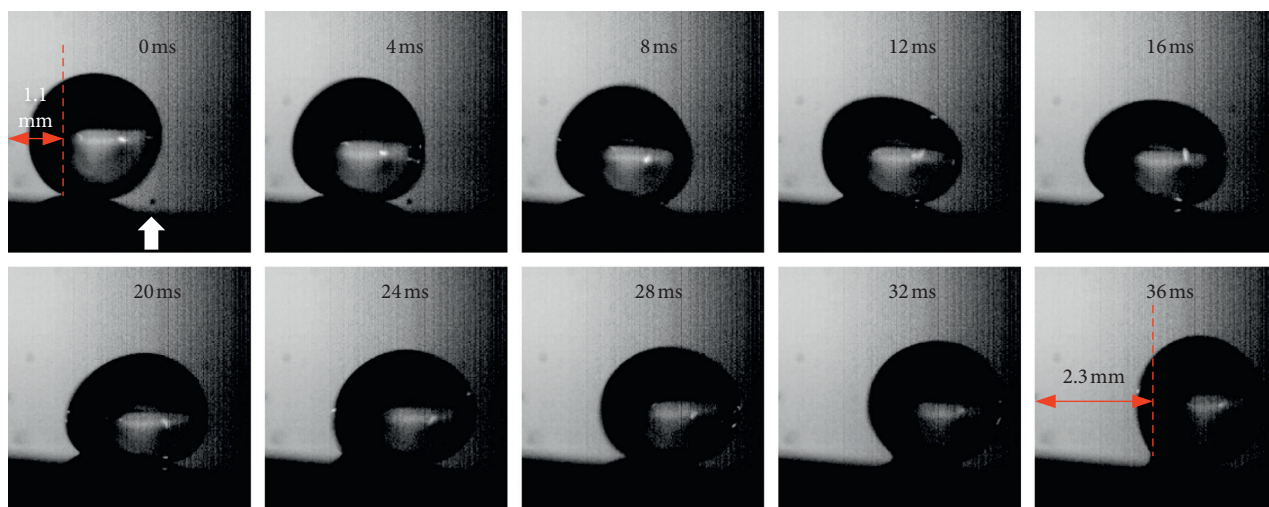
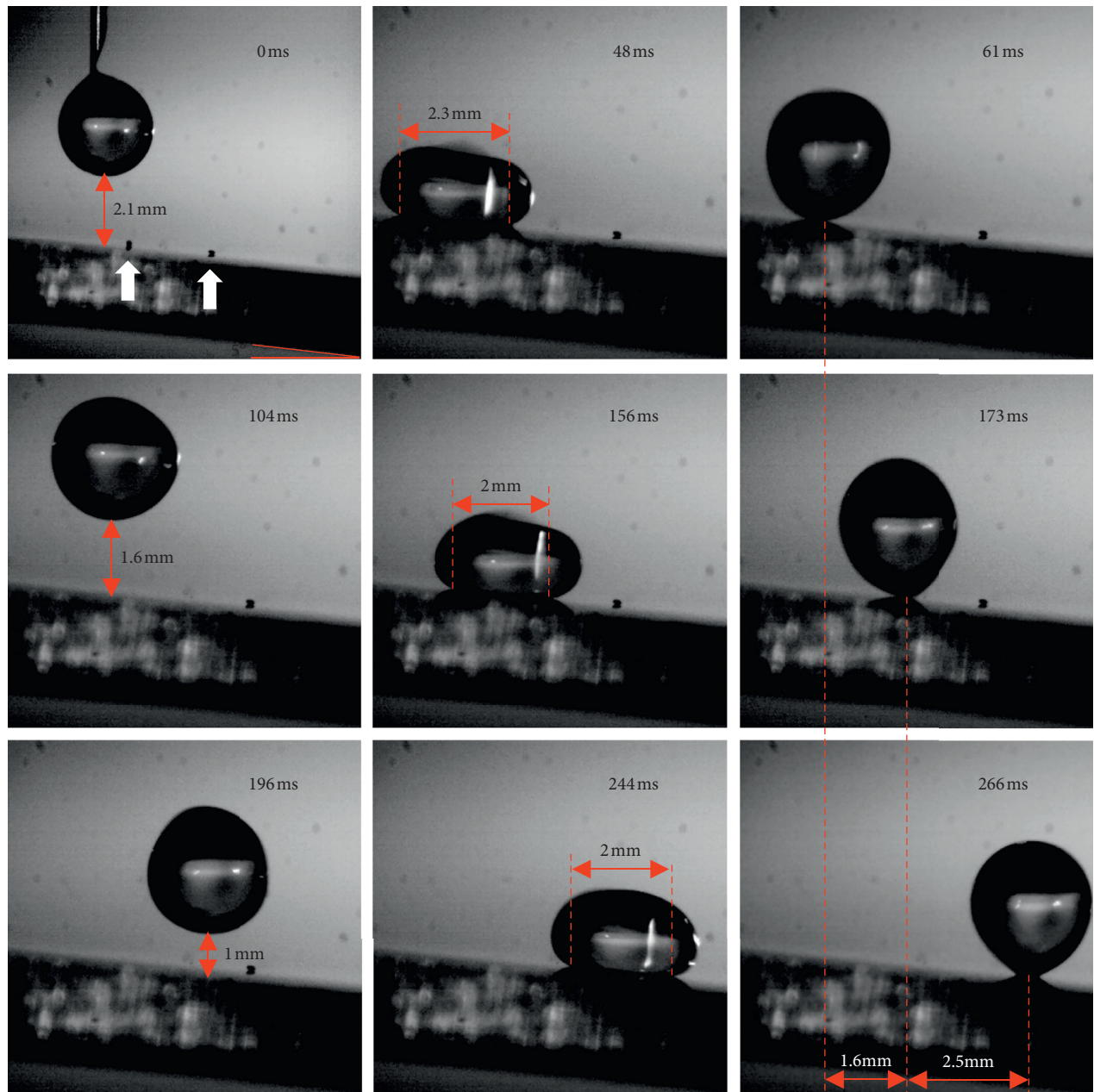
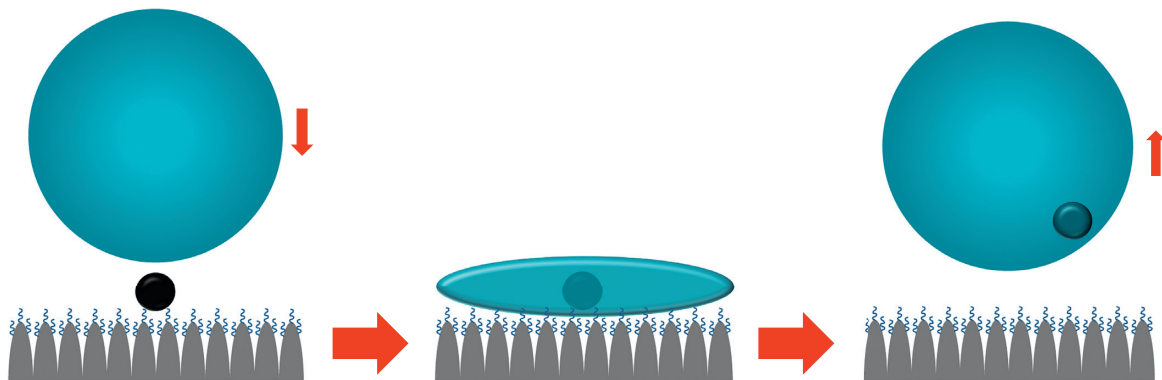


FIGURE 9: "Rolling" cleaning mode: (a) photos recorded by using a high speed camera and (b) schematic of antifouling process.



(a)



(b)

FIGURE 10: "Rebounding" cleaning mode: (a) high speed camera photos and (b) schematic of the particle removing process.

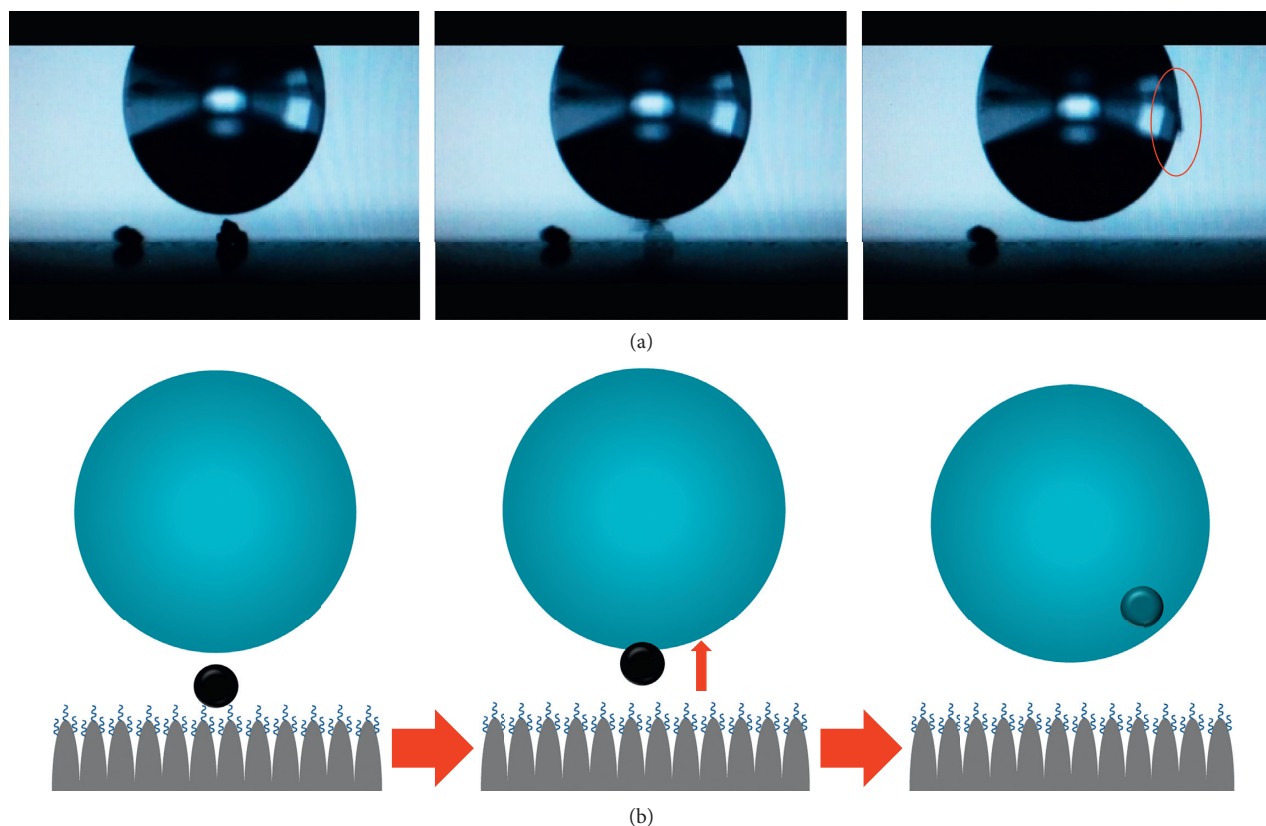


FIGURE 11: “Absorbing” cleaning mode: (a) photos taken by using a camera and (b) schematic of the “absorbing” particle removing process.

which can be regarded a damage-free cleaning process. Figure 11(b) is a schematic of the “absorbing” cleaning mode.

4. Conclusions

This article presents techniques to make self-cleaning stainless steel (SS) surface, including tailoring surface morphology by femtosecond laser irradiation and reducing surface free energy by fluorination. Results revealed that different micro/nanostructures including laser-induced periodic structures and nodular structures were obtained on 304SS. Fluorine-free surfaces with controllable water contact angles (CAs) from hydrophilic to superhydrophobic were obtained by using one-step femtosecond laser scan, which are desirable for microfluidic devices, lab-on-a-chip, sensor, and microreactor applications. Surface free energies of laser irradiated surfaces vary significantly from 23.1 ± 0.4 mN/m to 60.1 ± 0.2 mN/m comparing to the untreated 304SS (42.2 ± 2.0 mN/m); and the water contact angle roughly decreased with the increasing surface free energy. After fluorination treatment, the surface free energies of all specimens were reduced and CAs were much increased. All specimens showed near superhydrophobic property ($CA \sim 150^\circ$) except for the fluorinated 304SS (103°). The adhesive property of laser irradiated surface was reduced due to the formation of surface hydrophobic functional groups such as C-F, $-CF_2$, and $-CF_3$. A wettability model of specimens before and after fluorination was proposed, in which

the influence of micro/nanostructures, fluorination, and their combined effects on CAs were analysed. The interaction behaviors between water droplets and different types of particulate pollutants on self-cleaning SS were monitored and recorded. Three particulate cleaning modes, rolling, rebounding, and absorbing modes, have been suggested.

Data Availability

The data used to support the findings of this study are included within the article.

Conflicts of Interest

The authors declare that there are no conflicts of interest regarding the publication of this paper.

Acknowledgments

This work was supported by the National Natural Science Foundation of China (NSFC) (Grant nos.: 51701087 and 51535003) and Special Foundation for Young Scientists of LFRF.

References

- [1] M. Liu and L. Jiang, “Switchable adhesion on liquid/solid interfaces,” *Advanced Functional Materials*, vol. 20, no. 21, pp. 3753–3764, 2010.

- [2] I. Sas, R. E. Gorga, J. A. Joines, and K. A. Thoney, "Literature review on superhydrophobic self-cleaning surfaces produced by electrospinning," *Journal of Polymer Science Part B: Polymer Physics*, vol. 50, no. 12, pp. 824–845, 2012.
- [3] S. T. Yohe, J. D. Freedman, E. J. Falde, Y. L. Colson, and M. W. Grinstaff, "A mechanistic study of wetting superhydrophobic porous 3D meshes," *Advanced Functional Materials*, vol. 23, no. 29, pp. 3628–3637, 2013.
- [4] J. Li, Z. Jing, F. Zha, Y. Yang, Q. Wang, and Z. Lei, "Facile spray-coating process for the fabrication of tunable adhesive superhydrophobic surfaces with heterogeneous chemical compositions used for selective transportation of microdroplets with different volumes," *ACS Applied Materials & Interfaces*, vol. 6, no. 11, pp. 8868–8877, 2014.
- [5] K. Efimenko, J. Finlay, M. E. Callow, J. A. Callow, and J. Genzer, "Development and testing of hierarchically wrinkled coatings for marine antifouling," *ACS Applied Materials & Interfaces*, vol. 1, no. 5, pp. 1031–1040, 2009.
- [6] X. Yao, L. Xu, and L. Jiang, "Fabrication and characterization of superhydrophobic surfaces with dynamic stability," *Advanced Functional Materials*, vol. 20, no. 19, pp. 3343–3349, 2010.
- [7] D. Zhang, F. Chen, Q. Yang et al., "A simple way to achieve pattern-dependent tunable adhesion in superhydrophobic surfaces by a femtosecond laser," *ACS Applied Materials & Interfaces*, vol. 4, no. 9, pp. 4905–4912, 2012.
- [8] W. Wang, Y. Q. Liu, Y. Liu et al., "Direct laser writing of superhydrophobic pdms elastomers for controllable manipulation via marangoni effect," *Advanced Functional Materials*, vol. 27, 2017.
- [9] A. Y. Vorobyev and C. Guo, "Multifunctional surfaces produced by femtosecond laser pulses," *Journal Of Applied Physics*, vol. 117, p. 033103, 2015.
- [10] G. Li, J. Li, C. Zhang et al., "Large-area one-step assembly of three-dimensional porous metal micro/nanocages by ethanol-assisted femtosecond laser irradiation for enhanced antireflection and hydrophobicity," *ACS Applied Materials & Interfaces*, vol. 7, no. 1, pp. 383–390, 2015.
- [11] I. Jun, Y. W. Chung, Y. H. Heo et al., "Creating hierarchical topographies on fibrous platforms using femtosecond laser ablation for directing myoblasts behavior," *ACS Applied Materials & Interfaces*, vol. 8, 2016.
- [12] T. N. Banuprasad, T. V. Vinay, K. S. Cherumannil, S. Varghese, S. D. George, and S. N. Varanakkottu, "Fast transport of water droplets over a thermo-switchable surface using rewritable wettability gradient," *ACS Applied Materials & Interfaces*, vol. 9, 2017.
- [13] J. Yong, F. Chen, Q. Yang et al., "Rapid fabrication of large-area concave microlens arrays on PDMS by a femtosecond laser," *ACS Applied Materials & Interfaces*, vol. 5, no. 19, pp. 9382–9385, 2013.
- [14] C. De Marco, S. M. Eaton, R. Suriano et al., "Surface properties of femtosecond laser ablated PMMA," *ACS Applied Materials & Interfaces*, vol. 2, no. 8, pp. 2377–2384, 2010.
- [15] J. Yong, F. Chen, J. Huo et al., "Femtosecond laser induced underwater superaerophilic and supraerophobic PDMS sheets with through microholes for selective passage of air bubbles and further collection of underwater gas," *Nanoscale*, vol. 10, no. 8, pp. 3688–3696, 2018.
- [16] S. Moradi, N. Hadesfandiari, S. F. Toosi, J. N. Kizhakkedathu, and S. G. Hatzikiriakos, "Effect of extreme wettability on platelet adhesion on metallic implants: from superhydrophilicity to superhydrophobicity," *ACS Applied Materials & Interfaces*, vol. 8, no. 27, pp. 17631–17641, 2016.
- [17] J. Long, P. Fan, D. Gong et al., "Superhydrophobic surfaces fabricated by femtosecond laser with tunable water adhesion: from Lotus leaf to rose petal," *ACS Applied Materials & Interfaces*, vol. 7, no. 18, pp. 9858–9865, 2015.
- [18] S. Zouaghi, T. Six, S. Bellayer et al., "Antifouling biomimetic liquid-infused stainless steel: application to dairy industrial processing," *Acs Applied Materials & Interfaces*, vol. 9, 2017.
- [19] S. Schlie-Wolter, A. Deiwick, E. Fadeeva, G. Paasche, T. Lenarz, and B. N. Chichkov, "Topography and coating of platinum improve the electrochemical properties and neuronal guidance," *ACS Applied Materials & Interfaces*, vol. 5, no. 3, pp. 1070–1077, 2013.
- [20] Y. Li, D. X. Luong, J. Zhang et al., "Laser-induced graphene in controlled atmospheres: from superhydrophilic to superhydrophobic surfaces," *Advanced Materials*, vol. 29, 2017.
- [21] K. Yin, D. Chu, X. Dong, C. Wang, J.-A. Duan, and J. He, "Femtosecond laser induced robust periodic nanoripple structured mesh for highly efficient oil-water separation," *Nanoscale*, vol. 9, no. 37, pp. 14229–14235, 2017.
- [22] H. Shi, Z. Cui, W. Wang, B. Xu, D. Gong, and W. Zhang, "Blackening of magnesium alloy using femtosecond laser," *Applied Optics*, vol. 54, no. 25, pp. 7766–7772, 2015.
- [23] M. S. Ahsan and M. S. Lee, "Colorizing mechanism of brass surface by femtosecond laser induced microstructures," *Optik - International Journal for Light and Electron Optics*, vol. 124, no. 18, pp. 3631–3635, 2013.
- [24] T. Y. Hwang, A. Y. Vorobyev, and C. Guo, "Ultrafast dynamics of femtosecond laser-induced nanostructure formation on metals," *Applied Physics Letters*, vol. 95, no. 12, pp. 123111–123113, 2009.
- [25] A. Y. Vorobyev and C. Guo, "Direct femtosecond laser surface nano/microstructuring and its applications," *Laser & Photonics Reviews*, vol. 7, no. 3, pp. 385–407, 2013.
- [26] F. Chen, D. Zhang, Q. Yang et al., "Bioinspired wetting surface via laser microfabrication," *ACS Applied Materials & Interfaces*, vol. 5, no. 15, pp. 6777–6792, 2013.
- [27] C. Yao, S. Xu, Y. Ye et al., "The influence of femtosecond laser repetition rates and pulse numbers on the formation of micro/nano structures on stainless steel," *Journal of Alloys and Compounds*, vol. 722, pp. 235–241, 2017.
- [28] L. Li, V. Breedveld, and D. W. Hess, "Creation of superhydrophobic stainless steel surfaces by acid treatments and hydrophobic film deposition," *ACS Applied Materials & Interfaces*, vol. 4, no. 9, pp. 4549–4556, 2012.
- [29] K. M. T. Ahmmmed, E. J. Y. Ling, P. Servio, and A.-M. Kietzig, "Introducing a new optimization tool for femtosecond laser-induced surface texturing on titanium, stainless steel, aluminum and copper," *Optics and Lasers in Engineering*, vol. 66, pp. 258–268, 2015.
- [30] V. Oliveira, S. Ausset, and R. Vilar, "Surface micro/nanostructuring of titanium under stationary and non-stationary femtosecond laser irradiation," *Applied Surface Science*, vol. 255, no. 17, pp. 7556–7560, 2009.
- [31] Y. Zhang, L. Wang, and J. Gong, "Numerical simulation of femtosecond laser multi-pulse ablation of Ni-Ti alloy," *Acta Photonica Sinica*, vol. 45, p. 0514002, 2016.
- [32] W. Pfleging, R. Kumari, H. Besser, T. Scharnweber, and J. D. Majumdar, "Laser surface textured titanium alloy (Ti-6Al-4V): Part 1-surface characterization," *Applied Surface Science*, vol. 355, pp. 104–111, 2015.
- [33] L. Feng, S. Li, Y. Li et al., "Super-hydrophobic surfaces: from natural to artificial," *Advanced Materials*, vol. 14, no. 24, pp. 1857–1860, 2002.

- [34] B.-j. Li, M. Zhou, W. Zhang, G. Amoako, and C.-y. Gao, "Comparison of structures and hydrophobicity of femtosecond and nanosecond laser-etched surfaces on silicon," *Applied Surface Science*, vol. 263, pp. 45–49, 2012.
- [35] A. Steele, B. K. Nayak, A. Davis, M. C. Gupta, and E. Loth, "Linear abrasion of a titanium superhydrophobic surface prepared by ultrafast laser microtexturing," *Journal of Micromechanics and Microengineering*, vol. 23, no. 11, p. 115012, 2013.
- [36] L. Yao and J. He, "Recent progress in antireflection and self-cleaning technology—from surface engineering to functional surfaces," *Progress in Materials Science*, vol. 61, pp. 94–143, 2014.
- [37] B.-j. Li, H. Li, L.-j. Huang, N.-f. Ren, and X. Kong, "Femtosecond pulsed laser textured titanium surfaces with stable superhydrophilicity and superhydrophobicity," *Applied Surface Science*, vol. 389, pp. 585–593, 2016.

Research Article

A Low-Cost High-Temperature Sensor Based on Long-Period Fiber/Microfiber Gratings by Local Fictive Temperature Modification

Guorui Zhou,¹ Chuanhao Zhang ¹, Xiufang Xie,² Yi Wan,³ Caizhen Yao ¹, Jun Liu,² Longfei Niu,¹ Xinxiang Miao ¹, Hai Zhou,¹ Xiaodong Jiang,¹ Shizhen Xu ³, and Haibing Lv ¹

¹Laser Fusion Research Center, China Academy of Engineering Physics, Mianyang 621900, China

²Institute of Applied Electronics, China Academy of Engineering Physics, Mianyang 621900, China

³School of Physics, University of Electronic Science and Technology of China, Chengdu 610054, China

Correspondence should be addressed to Shizhen Xu; xusz@uestc.edu.cn and Haibing Lv; haibinglv@163.com

Received 2 March 2020; Accepted 12 May 2020; Published 11 June 2020

Guest Editor: Zhen He

Copyright © 2020 Guorui Zhou et al. This is an open access article distributed under the Creative Commons Attribution License, which permits unrestricted use, distribution, and reproduction in any medium, provided the original work is properly cited.

A high temperature-sensitive long-period fiber grating (LPFG) sensor fabricated by the local fictive temperature modification is proposed and demonstrated. High-frequency CO₂ laser pulses scan standard single-mode fiber (SMF), and the modification zones extended to the core of SMF. Experimental results demonstrate that the LPFG temperature sensors with 600 μm grating period and 32 period numbers offer the average sensitivity of 0.084 nm/C in the temperature range of room temperature (RM) to 875°C. The LPFGs fabricated here show exponential change in terms of the spectral wavelength shift versus changes in temperature. In addition, the maximum temperature sensitivity of 0.37 nm/C is achieved by employing long-period microfiber grating (LPMFG), fabricated by the microheater brushing technique and the local fictive temperature modification. LPMFG sensor exhibits better temperature characteristics due to a thinner diameter.

1. Introduction

Compared with conventional electronic sensors, fiber sensors have useful advantages such as their small volume, high sensitivity, fast response, resistance to electromagnetic field interference, and the potential for remote operation [1], which have attracted more and more attention in sensing fields, including monitoring temperature [2], refractive index [3], strain [4], and viruses [5]. The measurement of temperature has great significance in the application fields of industry, scientific research, and clinical medical. For decades, various temperature sensing methods based on optical fiber structure have been proposed and demonstrated, such as Fabry-Perot interferometers [6–8], Mach-Zehnder interferometers [9–11], Sagnac [12–14], fiber Bragg gratings [15–17], and long-period fiber gratings (LPFGs) [18–23].

LPFGs with a typical period of hundreds of micrometers provide a suitable method for a number of sensing and communication applications, due to its ease of fabrication, low insertion loss, and higher temperature sensitivity. Among the different techniques available to fabricate gratings, fictive temperature modification different from the traditional point-to-point technique is a novel method. The interest of the scientific community results from well establishment and ultra-short fabrication time besides enabling the fabrication gratings in any kind of fiber [24]. Fictive temperature modification is a powerful method for topography formation on fiber. Texture on the surface of fiber can be directly realized via the rapid timescales of heating and cooling of fiber by laser pulses with proper energy [25]. In this work, we demonstrate LPFG temperature sensors in the range of room temperature (RM) –875°C fabricated by the local fictive temperature modification via

high-frequency CO₂ laser pulses. Inexpensive standard single-mode fiber (SMF-28) is employed as material for long-period gratings fabrication, and the fabrication time of the temperature sensors proposed is less than 1 s. The experiments show that the temperature sensitivity of the proposed sensor could be effectively improved by fabricating the long-period microfiber gratings (LPMFGs). The maximum temperature sensitivity of the LPMFGs sensors with 32 period numbers and 600 μm grating period can reach 0.37 nm/C, which is 4 times higher than that of LPFG sensors, in the range of 30°C to 80°C.

2. Theoretical Analysis

The LPFGs can couple the core mode to the forward propagating cladding modes. The resonant wavelength is determined by the phase matching condition as follows:

$$\lambda_m = (n_{\text{eff}}^{\text{core}} - n_{\text{eff}}^{\text{clad},m})\Lambda, \quad (1)$$

where λ_m is the m th-order resonant wavelength at which light propagation in the core mode is coupled to the LP_{0m} cladding mode, $m = 1, 2, 3, 4, \dots$, $n_{\text{eff}}^{\text{core}}$; $n_{\text{eff}}^{\text{clad},m}$ and Λ represent effective refractive indices of core mode and the m th cladding mode and the grating period, respectively.

When the ambient temperature has changed, the effective refractive index of core and cladding will change. The LPFG material temperature expansion leads to the change in the grating period. The temperature sensitivity can be obtained by the chain-rule differentiation of equation (1) with respect to ambient temperature T . The dependence of resonance wavelength against temperature can be written as

$$\frac{d\lambda_m}{dT} = \frac{d(n_{\text{eff}}^{\text{core}} - n_{\text{eff}}^{\text{clad},m})}{dT} \cdot \Lambda + (n_{\text{eff}}^{\text{core}} - n_{\text{eff}}^{\text{clad},m}) \frac{d\Lambda}{dT}. \quad (2)$$

The first term on right hand side of equation (2) is contributed to relative thermal dependence of effective indices of the core and cladding. It defines dn^{core}/T and dn^{clad}/T as the core and cladding thermo-optic coefficients, respectively. For the proposed LPFGs sensors, the core and cladding with positive thermo-optic coefficients are considered.

3. Experiments and Results

Figure 1 illustrates the configuration of an experimental system used for fabricating LPFGs by local fictive temperature modification via high-frequency CO₂ laser pulses. Semiconductor laser diode (SLD, Thorlabs, S5FC1550P-A2) used as the light source with a center wavelength of 1550 nm was connected to SMF-28 as the input port of LPFGs, and the output port of the LPFGs was connected to the optical spectrum analyzer (OSA) (Yokogawa, 6370°C) to ensure successful fabrication of LPFGs. The fabrication of LPFGs by the local fictive temperature modification was performed in a two-step process. Firstly, SMF-28 fixed on two-dimensional translation stages was adjusted to the center of camera field of view using online monitoring system as a component of the local fabrication system. The local fabrication system

mainly consists of online monitoring system, two-dimensional translation stages, two-dimensional vibration mirrors, and a commercial CO₂ laser with a Gaussian beam and maximum output power of 100W operated at 1 kHz with a 25% duty factor. Secondly, 32 periods and the grating period of 600 μm patterns of LPFGs were designed by controlling software in order to obtain the required parameters. Based on equation (1), the grating period was selected to be $\Lambda = 600 \mu\text{m}$ so as to work on the effective wavelength region of the SLD source used in the experiment. The SMF-28 samples were moved to focus rectangular CO₂ laser irradiation zones. The laser beam was scanned by two-dimensional vibration mirrors, and the laser raster scanning was used to produce hexagonally or orthogonal modification zones according to the designed pattern to form LPFGs in this step. Due to the strong performance of two-dimensional vibration mirrors, the fabrication time of LPFGs was less 1 s.

Figure 2 shows morphologies of the fabricated LPFGs by the local fictive temperature modification. The surface of morphology of LPFGs was obtained by Leica optical microscope with polarization function (Leica, DM2500). The grating period and the period number were 600 μm and 32, respectively. The fabricated LPFGs appeared very uniform, and the saddle-shaped grooves were carved by CO₂ laser pulses along the fiber axis, as shown in Figure 2. The modification zones of refractive index extended to the core of SMF-28 gradually to form the modulation of input light.

The free-standing fabricated LPFGs could be affected by environmental factors including physical vibration and bending due to its high sensitivity characteristics. Simply equipped LPFGs is essential using a low RI UV curable polymer (Thorlabs) to avoid disturbance in experimental processes influencing sensing results. In brief, two sides of a microscope slide were covered with two regular slides in parallel to create a sensing region. Then, other two smaller slides were fixed in the center of two regular slides to support the LPFGs sample in place. UV curable polymer used to fix the samples was exposed under UV radiation (UV LED system, Thorlabs) for 30 s.

The schematic diagram of the temperature sensing experimental setup is illustrated in Figure 3. SLD source and the OSA used were the same as the ones for LPFG fabrication. The transmission spectra of the LPFGs were measured at different temperatures for the grating region ranging from RM to 875°C. The high temperature environment was provided by the microheater (NTT-AT, CMH7019) driven by a tunable DC power supply. The grating region of LPFGs was inserted into the center of the slot of the microheater whose length was enough to cover the entire grating region. The temperature environment increased by increasing the current of the power supply from 0 to 3.5 A with intervals of 0.1 A. Every temperature environment was kept constant for 10 minutes to ensure a stable temperature distribution in the microheater.

The transmission spectra were recorded at different temperatures. The relationship between the current and the temperature in the microheater was provided by the manufacturer of the heater.

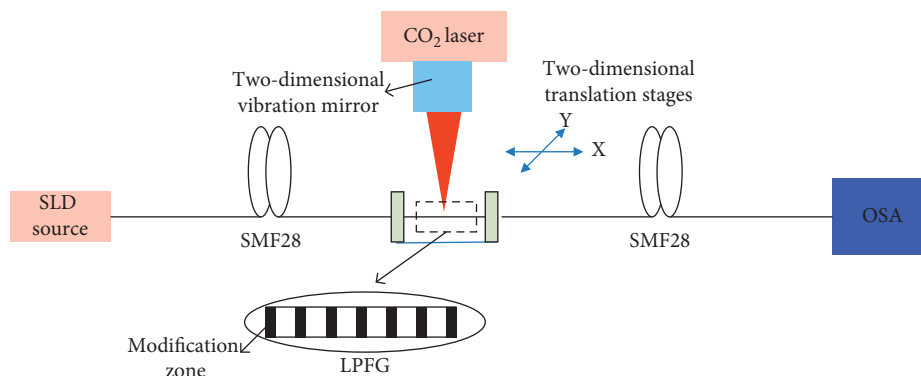


FIGURE 1: The fabrication setup of LPFGs by local fictive temperature modification via CO₂ laser.

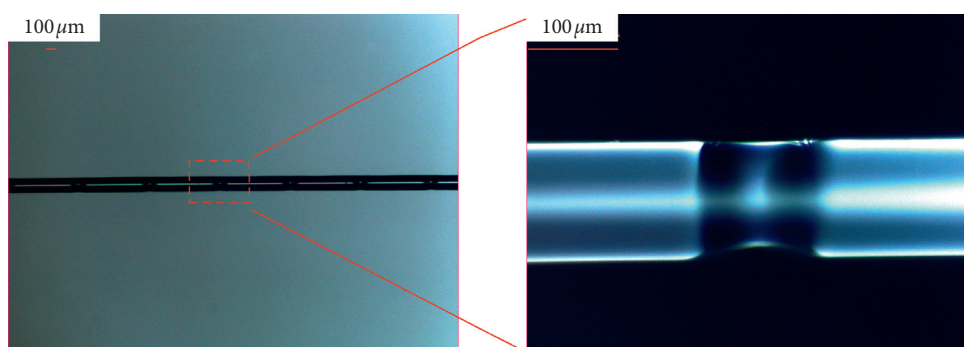


FIGURE 2: The surface morphologies of the fabricated LPFGs.

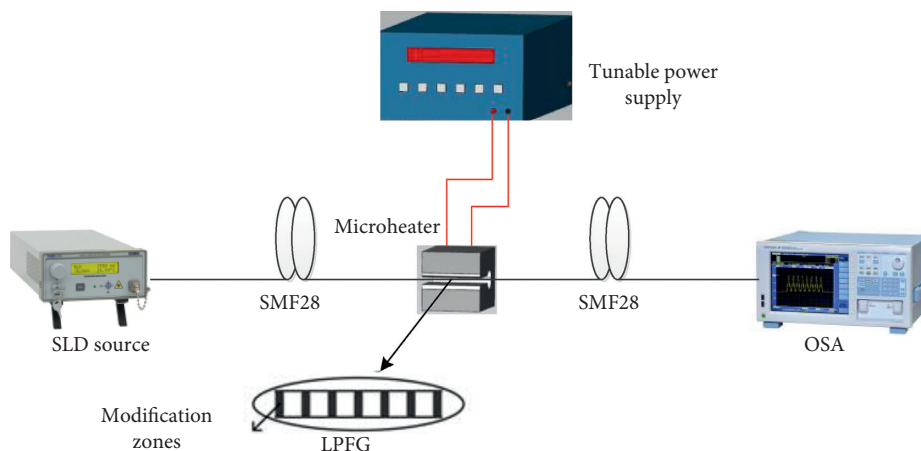


FIGURE 3: The schematic diagram of the temperature sensing experimental setup.

Figure 4(a) illustrates measured spectral responses at different temperatures ranging from RM to 875°C with intervals of 125°C. When the temperature environment increased, the selected dip wavelength of the spectrum experienced a redshift with the measured temperature range. These shifts correspond to a temperature-induced spectral shift of about 71.36 nm during the entire measurement process. To obtain the exact relationship between temperature environments and dip wavelength shift, a finer temperature variation experiment was adopted. Figure 4(b)

shows the relationship between temperature environment and dip wavelength shift over the temperature ranging from RM to 875°C by heating the LPFG sensors in 25°C steps. The average sensitivity 0.084 nm/C was achieved. The solid line in the figure was the exponential fit of the experimental results, which indicated that LPFG sensors have exhibited a higher sensitivity in the higher temperature range. Moreover, the performance of our LPFG temperature sensor in the cooling process has also been investigated, as shown in Figure 4(b). From the figure, it is clear that they have almost

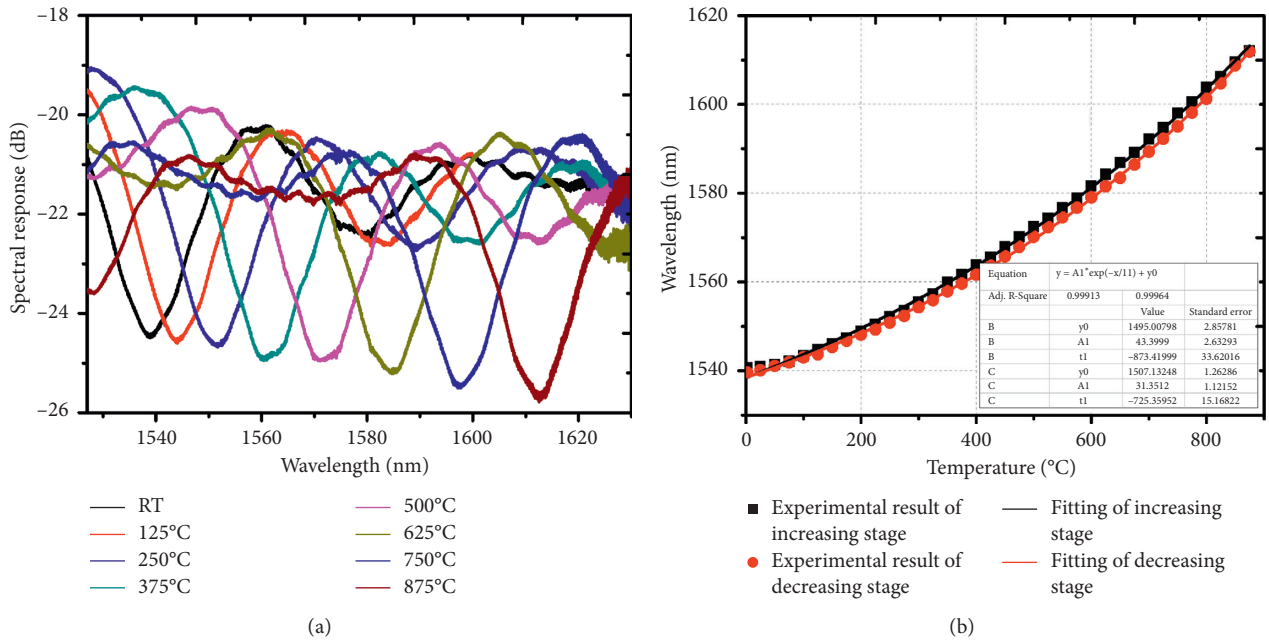


FIGURE 4: (a) Measured spectral responses at different temperatures ranging from RT to 875°C with intervals of 125°C; (b) the relationship between corresponding dip wavelength shifts and the temperature.

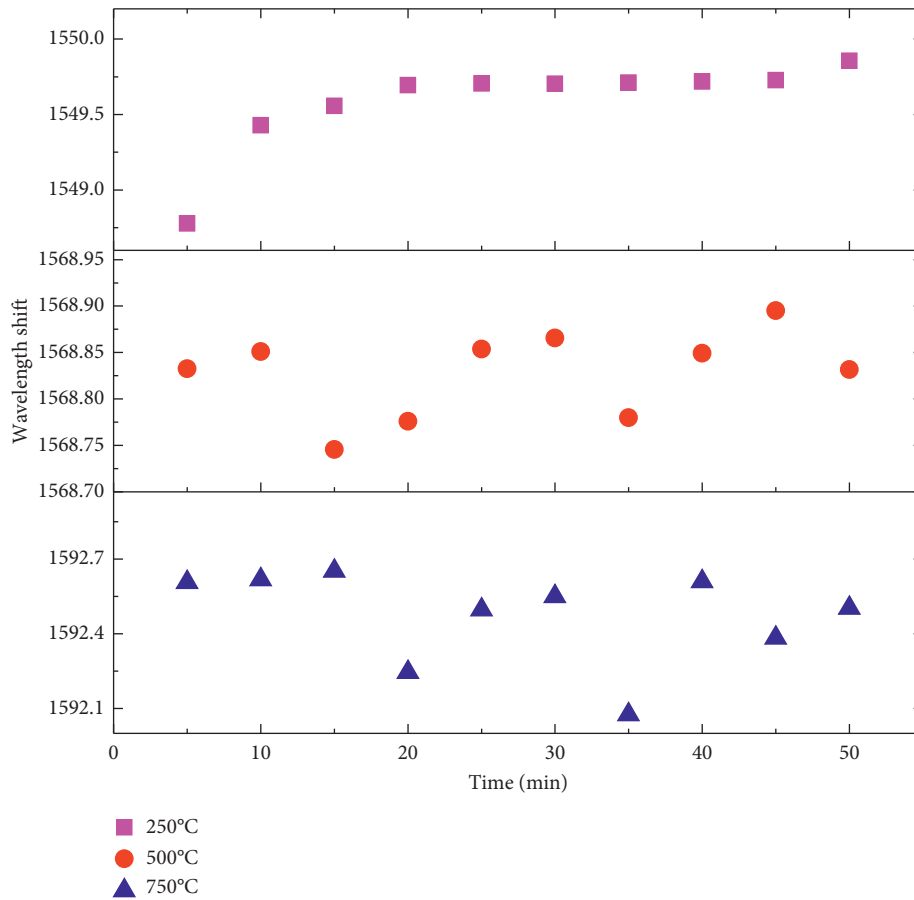


FIGURE 5: Signal changes with measurement time increasing at 250°C, 500°C, and 750°C.

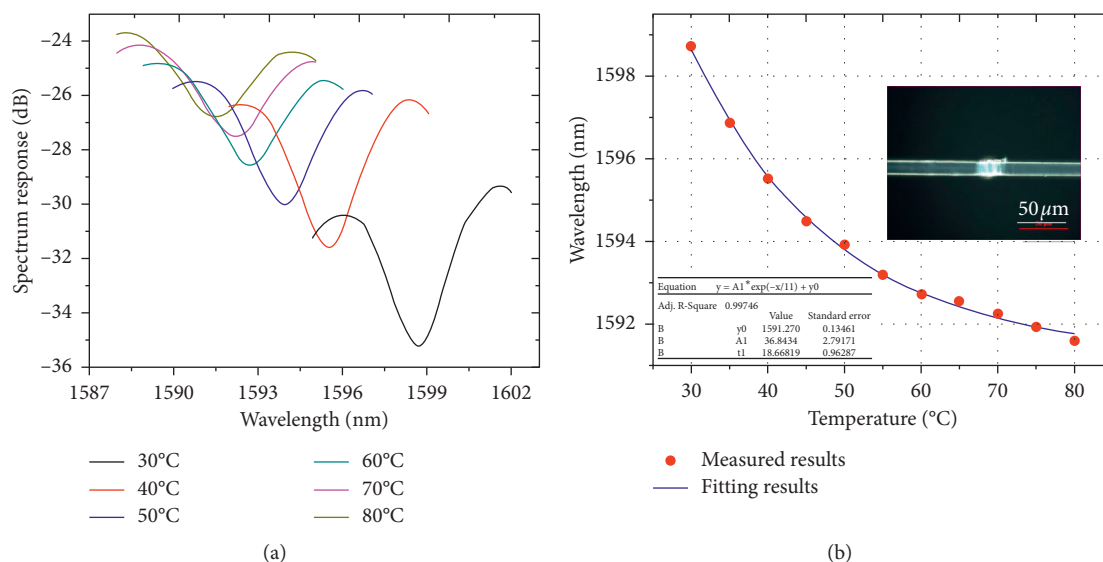


FIGURE 6: (a) Transmission spectrum of LPMFGs at different temperatures ranging from 30°C to 80°C; (b) corresponding relationships between temperature and the dip wavelength shift and the optical microscope image of modification zone of fabricated LPMFGs as shown in the inset.

the same exponential dependence on the temperature. The fit of the experimental data gave a sensitivity of about 0.085 nm/C. The different temperature sensitivity numbers result from the different temperature distribution during heating and cooling processes.

In order to investigate the stability of our LPFG temperature sensors in high temperature environment, signal changes with measurement time increasing at 250°C, 500°C, and 750°C are shown in Figure 5. Measured spectral responses during 50 minutes were recorded every 5 minutes. The redshift standard deviation of 0.54 nm at 250°C is larger than that of 500°C and 750°C, while the redshift standard deviation of 0.07 nm at 500°C is smaller than that of 250°C and 750°C. It believes that the discrepancy in dip wavelength shift at the same temperature mainly results from the limited precision in microheater heating controlling. We have reason to believe that LPFGs fabricated by local fictive temperature modification have excellent stability in the entire measurement process, and there is no stability performance degradation in high temperature environment.

As far as we know, reducing the diameter of LPFGs might result in a higher sensitivity. Hence, it is necessary to demonstrate temperature dependence of LPMFGs. In the experiment, microfibers with about 11 μm diameter were fabricated based on the taper drawing system using the microheater brushing technique. The fabrication and package process of LPMFGs were the same as that of the LPFGs. Considering more fragile mechanical stability, the fabricated LPMFGs were put into an airtight container with the function of precise control of temperature to measure the temperature dependence. The SLD source and OSA used were the same as the ones used for LPFG sensing. The transmission spectra of LPMFGs, as shown in Figure 6(a), were measured at different temperatures ranging from 30°C to 80°C. It was observed that, as the temperature increased from 30°C to 80°C, the central

wavelength of the spectral dip shifted to a shorter wavelength monotonically. The wavelength shifts versus temperature is clearly plotted in Figure 6(b). The modification zone of the fabricated LPMFGs can be observed in the inset of Figure 6(b). It is clear that wavelength shift changed exponentially with the increase in the temperature, from 30°C to 80°C. The total wavelength shifted from 30°C to 80°C was 7.1 nm, and the maximum sensitivity of 0.37 nm/C was achieved in the temperature range of 30°C to 35°C. The temperature sensitivity achieved in this experiment is 4 times higher than that of the LPFG temperature sensor. From the experimental results, the LPFGs fabricated by the local fictive temperature modification can be applied to the high temperature environment, but the LPMFGs are skilled in sensing of low temperature. Therefore, the parallel connection of the two methods can be used to realize the temperature sensing to ensure the measurement accuracy of low temperature.

4. Conclusion

In the work, a high temperature sensor based on LPFG fabricated by the local fictive temperature modification is demonstrated. Compared with LPFGs fabricated by other methods, the LPFGs demonstrated in the work provide a lower cost, shorter fabrication time, and wider temperature range. The sensor has an average temperature sensitivity of 0.084 nm/C in the range of RM-875°C by exponential fitting, while the maximum temperature sensitivity of LPMFGs is 0.37 nm/C. Moreover, the reason why the temperature sensitivity of LPMFGs can be enhanced is mainly due to the thinner diameter with thermo-optic effect. The high temperature sensor with compact structure and high sensitivity can be applicable to some structure health monitoring and material processing, electrical transformer, petroleum pipeline, and so on.

Data Availability

The datasets generated during and/or analysed during the current study are available from the corresponding author on reasonable request.

Conflicts of Interest

The authors declare that they have no conflicts of interest.

Acknowledgments

The work was supported by the National Natural Science Foundation of China (Grant nos. 51535003, 61605186, and 61705205) and Laser Fusion Research Center Funds for Young Talents (Grant no. RCFPD1-2017-7).

References

- [1] O. S. Wolfbeis, "Fiber-optic chemical sensors and biosensors," *Analytical Chemistry*, vol. 80, no. 12, pp. 4269–4283, 2008.
- [2] L. V. Nguyen, D. Hwang, S. Moon, D. S. Moon, and Y. Chung, "High temperature fiber sensor with high sensitivity based on core diameter mismatch," *Optics Express*, vol. 16, no. 15, pp. 11369–11375, 2008.
- [3] W. Liang, Y. Huang, Y. Xu, R. K. Lee, and A. Yariv, "Highly sensitive fiber Bragg grating refractive index sensors," *Applied Physics Letters*, vol. 86, no. 15, Article ID 151122, 2005.
- [4] X. Dong, H. Du, X. Sun, Z. Luo, and J. A. Duan, "A novel strain sensor with large measurement range based on all fiber Mach-Zehnder interferometer," *Sensors*, vol. 18, no. 5, p. 1549, 2018.
- [5] M. Janczuk-Richter, M. Dominik, E. Roźniecka et al., "Long-period fiber grating sensor for detection of viruses," *Sensors and Actuators B: Chemical*, vol. 250, pp. 32–38, 2017.
- [6] G. Zhang, X. Wu, S. Li et al., "Miniaturized Fabry-Perot probe utilizing PMPCF for high temperature measurement," *Applied Optics*, vol. 59, no. 3, pp. 873–877, 2020.
- [7] X. L. Cui, H. Zhang, and D. N. Wang, "Parallel structured optical fiber in-line Fabry-Perot interferometers for high temperature sensing," *Optics Letters*, vol. 45, no. 3, pp. 726–729, 2020.
- [8] T. T. Salunkhe, D. J. Lee, H. K. Lee, H. W. Choi, S. J. Park, and I. T. Kim, "Enhancing temperature sensitivity of the fabry-perot interferometer sensor with optimization of the coating thickness of polystyrene," *Sensors*, vol. 20, no. 3, p. 794, 2020.
- [9] T. Liu, J. Wang, Y. Liao, X. Wang, and S. Wang, "All-fiber Mach-Zehnder interferometer for tunable two quasi-continuous points' temperature sensing in seawater," *Optics Express*, vol. 26, no. 9, pp. 12277–12290, 2018.
- [10] S.-N. Wang, R.-Q. Lv, Y. Zhao, and J.-K. Qian, "A mach-zehnder interferometer-based high sensitivity temperature sensor for human body monitoring," *Optical Fiber Technology*, vol. 45, no. 9, pp. 93–97, 2018.
- [11] F. Zhang, X. Xu, J. He, B. Du, and Y. Wang, "Highly sensitive temperature sensor based on a polymer-infiltrated Mach-Zehnder interferometer created in graded index fiber," *Optics Letters*, vol. 44, no. 10, pp. 2466–2469, 2019.
- [12] J. Shi, Y. Wang, D. Xu et al., "Temperature sensor based on fiber ring laser with Sagnac loop," *IEEE Photonics Technology Letters*, vol. 28, no. 7, pp. 794–797, 2016.
- [13] L. Liu, H. Gao, T. Ning et al., "High accuracy temperature sensing system exploiting a Sagnac interferometer and an optoelectronic oscillator," *Optics & Laser Technology*, vol. 123, Article ID 105951, 2020.
- [14] G. Wang, Y. Lu, X. Yang, L. Duan, and J. Yao, "Square-lattice alcohol-filled photonic crystal fiber temperature sensor based on a Sagnac interferometer," *Applied Optics*, vol. 58, no. 8, pp. 2132–2136, 2019.
- [15] P. Cheng, L. Wang, Y. Pan et al., "Fiber Bragg grating temperature sensor of cladding with SrTiO₃ thin film by pulsed laser deposition," *Laser Physics*, vol. 29, no. 2, Article ID 025107, 2019.
- [16] P. Zhu, J. Wu, M. Huang, Y. Wang, P. Liu, and M. A. Soto, "Reducing residual strain in fiber bragg grating temperature sensors embedded in carbon fiber reinforced polymers," *Journal of Lightwave Technology*, vol. 37, no. 18, pp. 4650–4656, 2019.
- [17] A. Arora, M. Esmaelpour, M. Bernier, and M. J. F. Digonnet, "High-resolution slow-light fiber Bragg grating temperature sensor with phase-sensitive detection," *Optics Letters*, vol. 43, no. 14, pp. 3337–3340, 2018.
- [18] Q. Wang, C. Du, J. Zhang, R. Lv, and Y. Zhao, "Sensitivity-enhanced temperature sensor based on PDMS-coated long period fiber grating," *Optics Communications*, vol. 377, no. 15, pp. 89–93, 2016.
- [19] F. Zou, Y. Liu, S. Zhu, C. Deng, Y. Dong, and T. Wang, "Temperature sensitivity enhancement of the nano-film coated long-period fiber gratings," *IEEE Sensors Journal*, vol. 16, no. 8, pp. 2460–2465, 2016.
- [20] X. Dong, Z. Xie, C. Zhou, K. Yin, Z. Luo, and J. A. Duan, "Temperature sensitivity enhancement of platinum-nanoparticle-coated long period fiber gratings fabricated by femtosecond laser," *Applied Optics*, vol. 56, no. 23, pp. 6549–6553, 2017.
- [21] J. Mohanraj, V. Velmurugan, S. Sathiyam, and S. Sivabalan, "All fiber-optic ultra-sensitive temperature sensor using few-layer MoS₂ coated D-shaped fiber," *Optics Communications*, vol. 406, no. 1, pp. 139–144, 2018.
- [22] Y. Zhao, Y. Zhang, and R. Lv, "Simultaneous measurement of magnetic field and temperature based on magnetic fluid-infiltrated photonic crystal cavity," *IEEE Transactions on Instrumentation and Measurement*, vol. 64, no. 4, pp. 1055–1062, 2015.
- [23] B. Sun, Z. Zhang, W. Wei et al., "Unique temperature dependence of selectively liquid-crystal-filled photonic crystal fibers," *IEEE Photonics Technology Letters*, vol. 28, no. 12, pp. 1282–1285, 2016.
- [24] C. Colaco, P. Caldas, I. Del Villar, R. Chibante, and G. Rego, "Arc-induced long-period fiber gratings in the dispersion turning points," *Journal of Lightwave Technology*, vol. 34, no. 19, pp. 4584–4590, 2016.
- [25] C. Zhang, W. Liao, K. Yang et al., "Fabrication of concave microlens arrays by local fictive temperature modification of fused silica," *Optics Letters*, vol. 42, no. 6, pp. 1093–1096, 2017.

Research Article

Evaluation of Oxidation Performance of TRISO Fuel Particles for Postulated Air-Ingress Accident of HTGR

Fangcheng Cao ^{1,2}, De Zhang,² Qingjie Chen,¹ Hao Li,¹ and Hongqing Wang ¹

¹School of Chemistry and Chemical Engineering, University of South China, Hengyang Hunan 421001, China

²Cooperative Innovation Center for Nuclear Fuel Cycle Technology and Equipment, University of South China, Hengyang Hunan 421001, China

Correspondence should be addressed to Hongqing Wang; hqwang2015@126.com

Received 6 March 2020; Accepted 24 April 2020; Published 22 May 2020

Guest Editor: Yuxin Wang

Copyright © 2020 Fangcheng Cao et al. This is an open access article distributed under the Creative Commons Attribution License, which permits unrestricted use, distribution, and reproduction in any medium, provided the original work is properly cited.

In a high-temperature gas-cooled reactor, the integrity of tristructural-isotropic-(TRISO-) coated fuel particles ensures the safety of the reactor, especially in case of an air-ingress accident. The oxidation of TRISO particles with the outer layers of silicon carbide (SiC) was performed at temperatures of 900°C–1400°C in air environment. Both the microstructure and phase composition of the SiC layers were studied. The results showed that the SiC layers had a good oxidation resistance below 1100°C. However, the amorphous silica on the SiC layers formed at 1200°C and gradually crystallized at 1400°C with the presence of microcracks. The reaction rates of the SiC layers were determined by measuring the silica thickness. It was proposed that the oxidation of the SiC layers followed the linear-parabolic law with the activation energy of 146 ± 5 kJ/mol. The rate-determining step of the oxidation was the diffusion of oxygen in silica.

1. Introduction

The high-temperature gas-cooled reactor (HTGR) is considered as one of the promising reactors in the Generation IV nuclear energy system. The HTGR reference concept is a helium-cooled, graphite-moderated, thermal neutron spectrum reactor with a target coolant outlet temperature of ~900°C. The high outlet temperature offers higher efficiency electricity generation and new opportunities for a broad spectrum of process heat applications, including hydrogen production by thermochemical water splitting or high-temperature electrolysis [1]. The success of HTGR is due to its inherent safety characteristics, which rely closely upon the quality and integrity of the tristructural-isotropic- (TRISO-) coated fuel particles [2].

In the current reference TRISO-coated particle design, the kernel (microsphere) is typically formed from enriched uranium dioxide (UO₂) or uranium oxycarbide (UCO) and is surrounded by successive layers of porous pyrocarbon

buffer, dense inner pyrolytic carbon (IPyC), silicon carbide (SiC), and dense outer pyrolytic carbon (OPyC). The SiC layer, in particular, provides structural support to accommodate internal gas pressure and serves as the primary barrier to the release of fission products [3]. Therefore, the microstructure and properties of the SiC layer are essential to the safety of the reactors under operation conditions, even during any accidents, in the case of failure of all active cooling systems and complete loss of forced cooling.

Under normal operation conditions, the fuels work in helium loops and withstand a working temperature of ~1000°C in the HTGR. The highest normal operating fuel temperature should not be greater than 1250°C. In previous studies, postulated air-ingress accidents have got a lot of attention to the safety analyses of HTGR. In the case of off-normal transients, air ingress can result from breaches in the reactor system that link the internal and external gaseous atmospheres. The maximum fuel temperature might rise to 1300°C–1400°C. Under normal pressure and

high temperature air environment, the core components, including the fuel elements, would suffer extensive degradation and lead to a significantly enhanced release of fission products [4]. The oxidation of graphite is of primary importance with respect to the structural integrity of the graphite [5]. Much effort has been devoted to the consequences of graphite oxidation. The oxidation performance of matrix graphite under air-ingress accident conditions has not only been simulated under the conservative assumptions but also been studied thermogravimetrically for various oxygen concentrations and with temperatures from 600°C to 1600°C [6–8]. However, the matrix graphite of fuel elements is susceptible to oxidation damage. Once the graphite matrix of the compact or pebble fuel elements has been oxidized away, it may lead to the exposure of TRISO fuel particles and increase the risk of radioactivity release. The consequences of air-ingress for TRISO fuel particles have not been adequately addressed to date. Despite the rare probability of this accident, the oxidation behavior of the TRISO particle is of great importance for protecting the reactor core and decreasing the risk of radioactivity release in case of air-ingress accidents. As the OPyC layers begin to be oxidized at temperatures higher than 700°C, the exposed SiC layers in TRISO particles would play an important role in governing fuel performance. Therefore, the investigation of the oxidation performance of the SiC layers is imperative in the safety considerations.

The air oxidation of SiC materials (e.g., sintered α -SiC, high-purity β -SiC, and SiC-based composites) has attracted tremendous research interest for decades, due to its wide application in high-temperature components [9–11]. Two forms of SiC oxidation, such as the passive oxidation regime (weight gain) and the active oxidation (weight loss), were reported. SiC forms a silica layer comparable to silicon, and the oxidation of both materials follows a linear-parabolic or parabolic law. However, since the microstructure and properties of the SiC layers in TRISO particles are different from those of the SiC plate despite the same coating procedure, the oxidation mechanisms of the SiC layers are also needed to be clarified [12]. The impact of annealing in air atmosphere on TRISO particles has been investigated with temperatures up to 1600°C [13–15]. The results showed that intense regression of the SiC beneath the rough silica layer occurred at 1600°C, which was affected by the interaction between TRISO particles and the alumina crucible [13]. The mechanisms and kinetics of the oxidation process of the TRISO particles with the outer layers of SiC in air environment under different temperatures still need to be investigated to evaluate the microstructure evolution of the silica layer.

In the present work, the oxidation of TRISO particles with the outer layers of SiC was investigated in air environment at the temperature range of 900°C–1400°C. The composition and microstructure of the SiC layers after oxidation was characterized and analyzed. The oxidation kinetics of the SiC layer were studied, including oxidation rate, activation energy, and the rate-controlling step, which aims to predict the SiC degradation rate in case of an air-ingress accident in operation.

2. Experimental Procedure

2.1. High-Temperature Oxidation. The TRISO particle samples were made by fluidized bed chemical vapor deposition using zirconia particles with a diameter of $\sim 500\ \mu\text{m}$ as simulated kernels. The average thickness of the buffer, IPyC, SiC, and OPyC layers was $200\ \mu\text{m}$, $40\ \mu\text{m}$, $24\ \mu\text{m}$, and $40\ \mu\text{m}$, respectively. Before the oxidation test, the TRISO particle samples were exposed in air at 800°C for 8 hours to oxidize the OPyC layers and obtain the TRISO particles with the outer layers of SiC, as shown in Figure 1.

High-temperature oxidation behavior for the TRISO particles with the outer layers of SiC was investigated in atmospheric environment at 1 atm pressure under the isothermal conditions. The furnace was horizontally held with an alumina tube and has a 20 cm long hot zone. The TRISO particle samples were placed on the platinum crucible in the alumina reaction tube with both ends open. The samples were heated from room temperature at the programmed heat rate of 5°C/min up to the testing temperatures (900°C–1400°C). After keeping at the testing temperature for the desired time (0–48 h), the samples were cooled to room temperature in furnace naturally. To minimize contamination, the alumina reaction tube was aged in atmospheric environment for 50 h at 1400°C before beginning the experiments. Besides, the effects of interaction between the TRISO particle samples and the platinum crucible were neglected in the present work.

2.2. Characterization. The surface morphology and cross-section microstructure of the SiC layers in TRISO particles was characterized using a scanning electron microscope (SEM) (Inspect F50, FEI, US). The thickness of the silica on the SiC layer after oxidation was measured at approximately twenty points at the cross sections of TRISO particles. The phases of reactive products on the surfaces of TRISO particles were examined by X-ray diffraction (XRD) (Ultima IV, Rigaku, Japan) and by Raman spectroscopy (LabRAM HR Evolution, Horiba, France) with an incident laser beam of 532 nm (Nd: YAG). The XRD samples were made by around a number of 20 particles, which were pasted onto a horizontal glass slide and kept closely packed using the silicone paste that has no XRD spectra. For Raman spectroscopy measurement, the TRISO particle was placed on the sample stage under the Raman microscope objective. And the 50x microscope objective was used to focus the laser and collected the backscattered light.

3. Results and Discussion

3.1. The Microstructure of the SiC Layers. Figure 2 shows the surface morphology of the SiC layers before and after oxidation at different temperatures for 24 h. The as-deposited SiC layer exhibited faceted morphology on the outer surface (Figure 2(a)). No significant variation in the morphology was observed after oxidation below 1100°C (Figure 2(b)). However, the edge of the SiC grains became smooth after oxidation at 1200°C, which indicates the oxidation of SiC

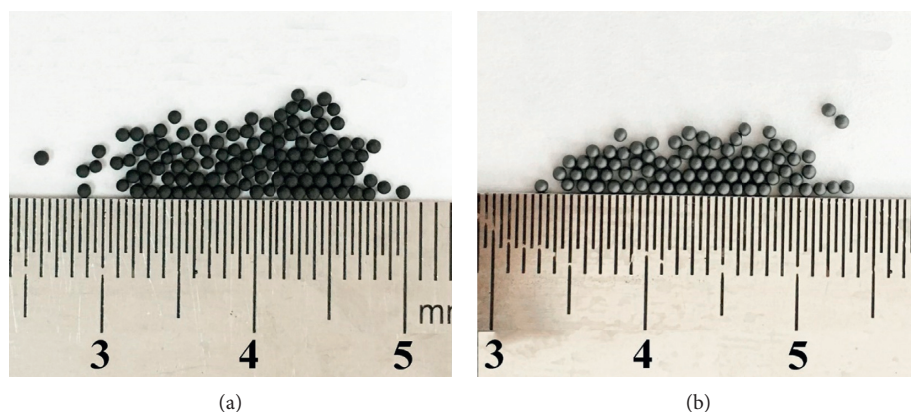


FIGURE 1: TRISO particle samples (a) with the OPyC layers and (b) without the OPyC layers.

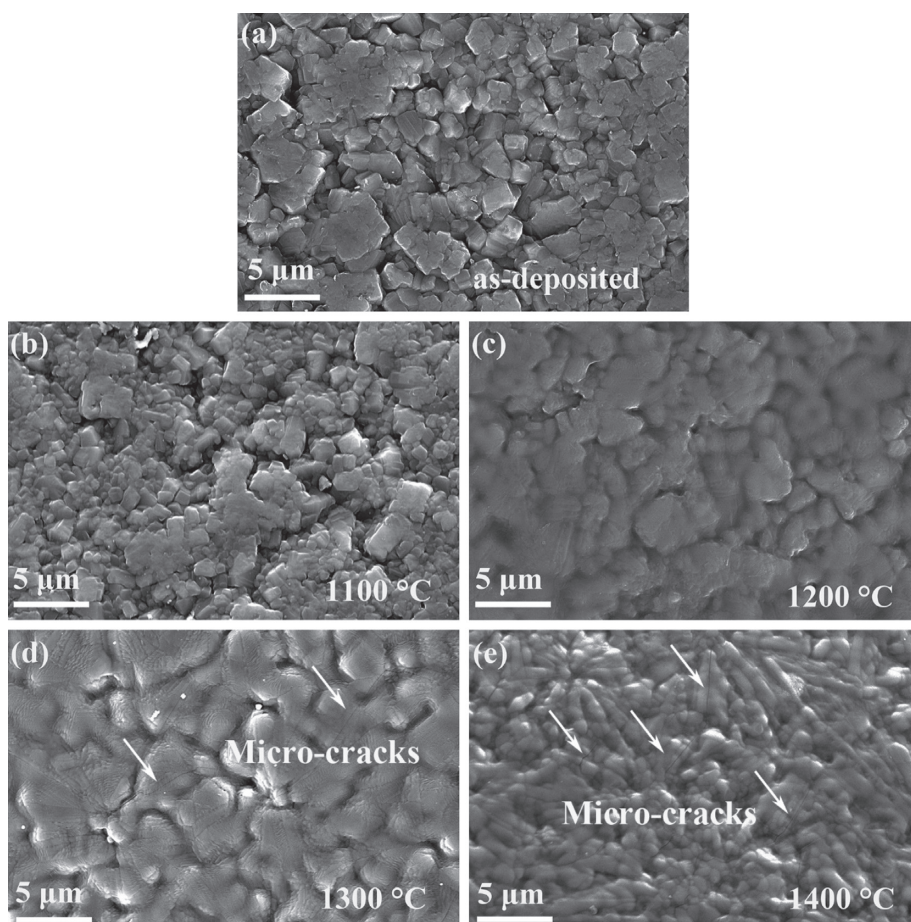


FIGURE 2: The outer-surface SEM morphology of the SiC layers of (a) as-deposited and after exposure in air at a temperature of (b) 1100°C, (c) 1200°C, (d) 1300°C, and (e) 1400°C for 24 h.

occurred (Figure 2(c)). Because the oxidation temperature was not high enough to cause an obvious change of the surface morphology, just the sharp edge became smooth could be observed. Besides, the thickness of the oxide layer was too thin to cover the faceted morphology of the SiC grains. Thus, there were still some pits that could not be covered by the oxide layer, where the oxidation would occur.

After oxidation at 1300°C, the surface morphology changed from multifaceted to smooth with the formation of a thin oxide layer (Figure 2(d)). The SiC grains were almost covered by the formation of the oxide layer, which could prevent inward diffusion of oxygen and the oxidation of SiC. When the oxidation temperature was further increased to 1400°C, apparent oxidation occurred with the increasing amount of

oxide on the SiC surface (Figure 2(e)). The surface of the oxide scale appeared a combination of elongated and spherulitic structure, which is the characteristic of the cristobalite formation. As reported, during the crystallization of amorphous silica, the nucleation of silica grains forms elongated structure and then turns to spherulitic structure with the growth of silica grains [16]. That is the reason why the elongated and spherulitic structure could be observed after high-temperature oxidation of SiC. Meanwhile, microcracks formed in the oxide layer (Figures 2(d) and 2(e)), which could be due to the volume change from the crystallization of amorphous silica and the phase transformation of crystallized silica during the cooling process. The formation of microcracks would reduce the protection of the oxide layer for SiC from oxidation. What is worse, a significant volume change might also loosen the structure of the oxide layer and lead to poor adhesion at the interface of the oxide layer and SiC.

Figure 3 shows the cross-section microstructure of the SiC layers before and after oxidation at the temperatures of 1100°C–1400°C for 24 h. There were no significant microstructure differences observed from the cross section between the as-deposited SiC layer and the SiC layer after oxidation at 1100°C. However, a thin oxide layer on the SiC coating was appeared after oxidation at 1200°C, and the thickness was about 0.41 μm . Due to the roughness of the as-deposited SiC layer, the oxide layer was rather rough. After oxidation at 1300°C, the thickness of the oxide layer increased to $\sim 0.7 \mu\text{m}$. Besides, the surface of the oxide layer became more flat, which indicates the oxide had filled in the roughness of the as-deposited SiC layer. When the oxidation temperature was further increased to 1400°C, the thickness of the oxide layer increased significantly to $\sim 1.24 \mu\text{m}$. No through-thickness cracks were observed.

3.2. The Phase Composition of the SiC Layers. Figure 4 shows the effects of oxidation temperature on the XRD patterns of TRISO particles after oxidized for 24 h. Three typical phases could be identified in the XRD pattern of the as-deposited sample, namely, ZrO_2 , PyC , and SiC. To amplify the small peaks, the Y-axis was plotted to the sqrt (intensity) (Figure 4(b)). At temperatures below 1300°C, no oxide phase was detected. After oxidation at 1400°C, diffraction peaks corresponding to the silica phase appeared with weak intensity. The results showed that the silica formed was amorphous at 1200°C–1300°C and gradually crystallized at 1400°C. It was coincident with the evolution of surface morphology observed in Figure 2. Besides, the major crystalline silica phase was detected to be α -cristobalite.

Raman spectroscopy was also employed to characterize the phase composition of TRISO particles after oxidation at different temperatures. Raman spectra of SiC showed two first-order peaks at around 796 cm^{-1} (TO band) and 972 cm^{-1} (LO band) with the second-order band between 1400 cm^{-1} and 1800 cm^{-1} , which corresponds to stoichiometry β -SiC. Significant differences in the Raman spectra at ranges of 100 cm^{-1} –550 cm^{-1} and 1200 cm^{-1} –1850 cm^{-1} were observed, as shown in Figure 5. When the oxidation

temperature increased to 1400°C, the peaks at 110 cm^{-1} , 230 cm^{-1} , and 417 cm^{-1} appeared which correspond to the existence of silica. The results were consistent with the XRD analyses. Besides, the *D* band (1350 cm^{-1}) and *G* band (1600 cm^{-1}) that are the first-order band of carbon also appeared with the increase of oxidation temperature above 1200°C, suggesting that the carbon was in form of amorphous structure [17]. The results revealed the formation of carbon occurred during the oxidation of SiC at high temperatures. The low intensity of the *D* and *G* bands indicates a small proportion of carbon produced after high-temperature oxidation of SiC, which was identified at the SiC/SiO₂ interface in the previous studies by transmission electron microscopy [18].

3.3. The Oxidation Behavior of the SiC Layers. To study the oxidation behavior of the SiC layers in TRISO particles, oxidation tests were further performed at different temperatures for different times. The oxide layer thickness as a function of the oxidation time is shown in Figure 6. When the temperature was below 1000°C, the changes in the surface morphology of the SiC layer were barely noticeable. It indicates that the SiC had good oxidation resistance at a temperature below 1000°C. Besides, it seems no measurable oxidation occurred at 1100°C within 36 h exposure until the oxidation time was prolonged to 48 h. The dense oxide layer produced on the surface of the SiC layer could prevent the inward diffusion of oxygen. With the increase of oxidation temperature, the diffusion rate of oxygen in the silica increased, so did the oxidation rate. As a result, the thickness of the silica layer increased obviously with the increase of oxidation time at the higher temperature ($\geq 1200^\circ\text{C}$). As shown in Figure 6, the silica layer thickness was 1.9 μm after exposure at 1400°C for 48 h, which is almost twice that at 1300°C for the same dwelling time.

When SiC material is exposed in air environment under high temperature, a dense silica layer would be formed on the SiC surface. The inward diffusion of oxygen through the oxide layer is impeded, which inhibits further oxidation of the underlying SiC. As a result, the oxidation of SiC would be slow, which leads to the regression of SiC within the passive oxidation regime. In air environment at high temperature, the passive oxidation between SiC and oxygen is expressed by the following equation [9, 19]:

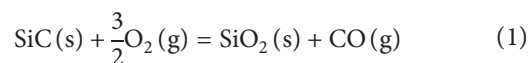


Figure 7 shows the oxidation kinetics of SiC in air environment using a dual logarithm coordinate. In the dual logarithm coordinate, a linear oxidation law presents a linear with a slope of 1, while a parabolic oxidation law presents a linear with a slope of 0.5 [20]. However, the slopes derived from Figure 7 were in a range of 0.75 to 0.67, which decreased with the increase of oxidation temperature. It indicates that the oxidation kinetics at the temperature range of 1200°C–1400°C could not be expressed using a simple linear or parabolic law. That is, the oxidation evolves both linear and parabolic law, which is reported as

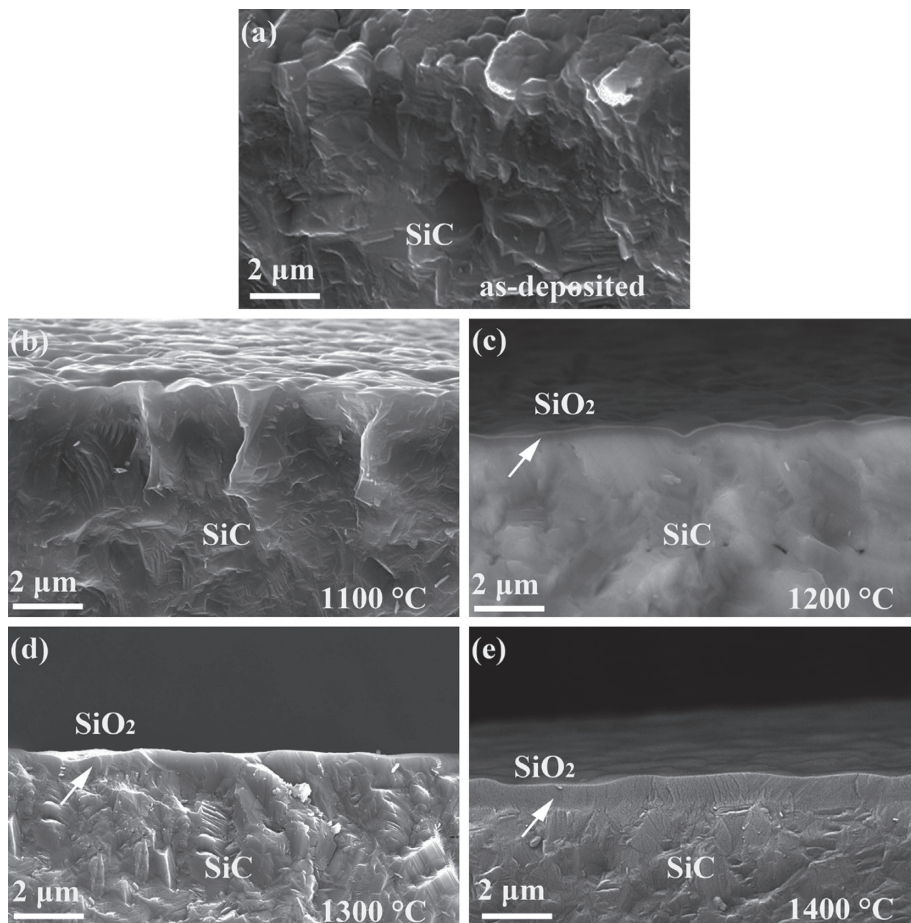


FIGURE 3: The fracture cross-section SEM morphology of the SiC layers of (a) as-deposited and after exposure in air at a temperature of (b) 1100°C, (c) 1200°C, (d) 1300°C, and (e) 1400°C for 24 h.

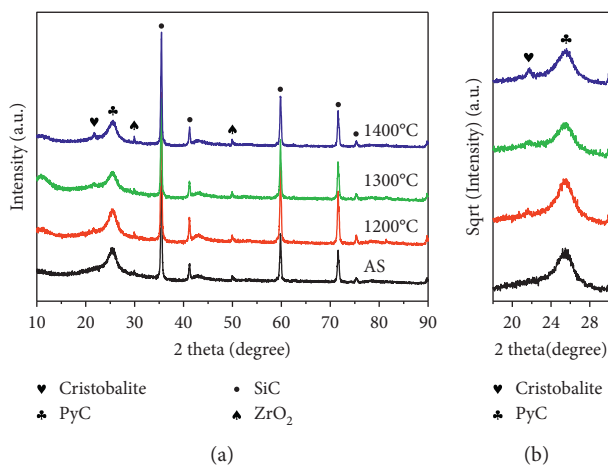


FIGURE 4: XRD patterns of TRISO particles. (a) Both as-deposited sample and the samples after air oxidation for 24 h at 1200°C–1400°C and (b) amplified XRD patterns from 18°–30°.

the linear-parabolic law. For the linear-parabolic law, the Deal–Grove model is often used to describe the relationship between the thickness of silica and the oxidation time, as follows [20]:

$$x^2 + Ax = Bt, \quad (2)$$

where x is the silica thickness (μm), t is the oxidation time (h), B/A is the linear oxidation rate ($\mu\text{m/h}$), and B is the parabolic

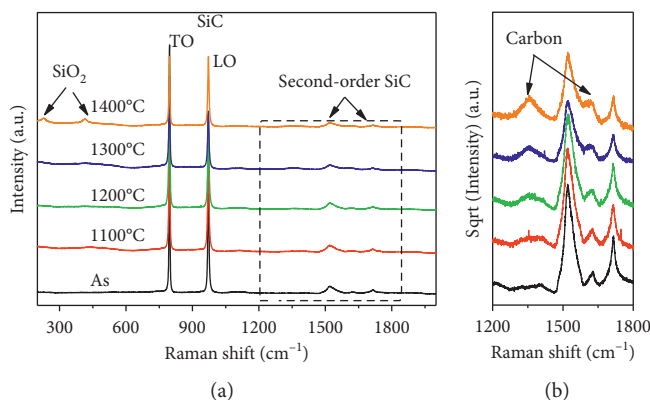


FIGURE 5: Raman spectra of TRISO particles. (a) Both as-deposited sample and the samples after air oxidation at 1200°C–1400°C for 24 h and (b) amplified Raman spectra from 1200 cm⁻¹–1800 cm⁻¹.

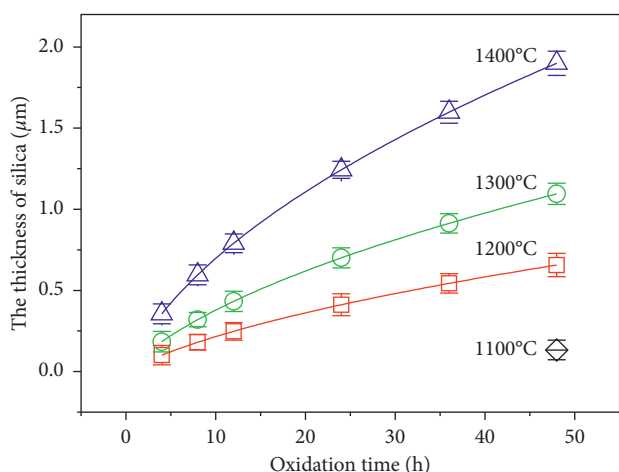


FIGURE 6: The thickness of the silica layer as a function of oxidation time under different temperatures in air atmosphere.

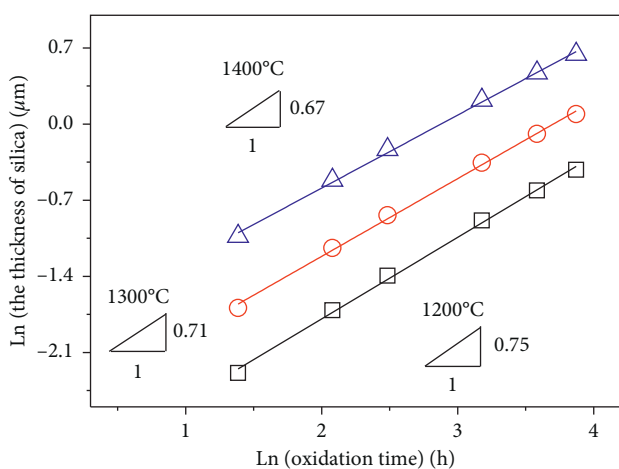


FIGURE 7: Oxidation kinetics of the SiC layer in air environment using a dual logarithm coordinate.

oxidation rate ($\mu\text{m}^2/\text{h}$). It is noted that B/A and B are the rate coefficients for the interfacial reaction and the diffusion of oxidants, respectively. By fitting the relationship between the

silica thickness and the oxidation time using equation (2), both the linear and parabolic rates were obtained and are summarized in Table 1. The linear and parabolic oxidation rates of SiC significantly increased with the increase of temperature. The growth rates of the silica oxidized at 1400°C are a little lower than the reported values (Table 1) [14]. According to the oxidation kinetics of the SiC layers, the microstructure evolution of the silica under different temperatures in air environment could be evaluated.

Meanwhile, the temperature dependence of the oxidation rate can be described using the Arrhenius equation:

$$k = K_0 \cdot \exp\left(\frac{-E_a}{RT}\right), \quad (3)$$

where k is the oxidation rate ($\mu\text{m}^2/\text{h}$), which is corresponding to the parabolic oxidation rate in this study, K_0 is the frequency factor ($\mu\text{m}^2/\text{h}$), E_a is the activation energy (kJ/mol), R is the ideal gas constant ($R = 8.314 \times 10^{-3} \text{ kJ}/(\text{mol}\cdot\text{K})$), and T is the temperature (K). Using equation (3) to fit the experimental data, the activation energy (E_a) can be estimated. Figure 8 shows the Arrhenius plot of the obtained parabolic rate constant versus temperature. The activation energy of the parabolic rates was yielded to be $146 \pm 5 \text{ kJ}/\text{mol}$ at the temperature range of 1200°C–1400°C. As reported in the previous literature, the activation energy values have ranged from 120 kJ/mol to 400 kJ/mol [14, 21, 22]. There is a general trend that the higher the temperature, the greater the activation energy. It is commonly accepted that the relatively low activation energy of 80 kJ/mol–120 kJ/mol may correspond to the permeation of oxygen molecule in amorphous silica and the high activation energy of 230 kJ/mol–400 kJ/mol may suggest the diffusion of oxide ion in amorphous silica or cristobalite [22]. The activation energy value obtained in the present work ($146 \pm 5 \text{ kJ}/\text{mol}$) is close to value for the diffusion of the oxygen molecules in amorphous silica. Therefore, the rate-controlling step was likely the diffusion of the oxygen molecules in the silica [23].

The continuing oxidation of SiC relies on the diffusion of oxygen through the covering silica layer, and thus, the diffusion kinetics control the oxidation rate of SiC. Initially, the formed layer was amorphous, but at temperatures above

TABLE 1: Summary of the linear and parabolic oxidation rates of the SiC layers in TRISO particles.

Oxidation temperature ($^{\circ}\text{C}$)	Linear rate ($\mu\text{m}/\text{h}$)	Parabolic rate ($\mu\text{m}^2/\text{h}$)
1200	0.030	0.017
1300	0.058	0.042
1400	0.125	0.121
	0.165 [14]	0.126 [14]

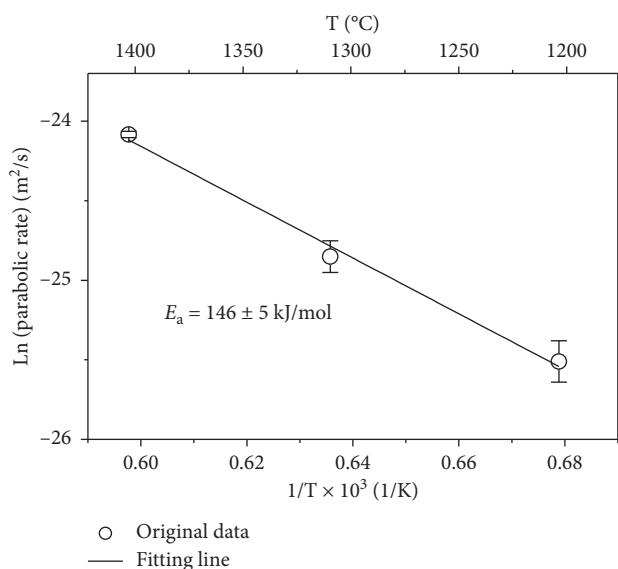


FIGURE 8: Arrhenius plots of parabolic oxidation rate as a function of temperature for the SiC layer oxidation in air atmosphere.

1400 $^{\circ}\text{C}$, devitrification of silica occurred, leading to the formation of α -cristobalite. Originally, it was considered that oxygen permeability in amorphous silica is high; however, some studies suggest that it might be similar for α -cristobalite. At higher temperatures, the viscous nature of silica may promote diffusion of oxygen. Some critical issues might arise, cristobalite undergoes a phase transformation associated with volume change during the cooling process that can lead to fracture and spallation. The formation of microcracks would provide the diffusion paths for oxygen and thus accelerated SiC oxidation significantly. Both the linear and parabolic oxidation rates of the SiC layers at 1400 $^{\circ}\text{C}$ were almost triple those at 1300 $^{\circ}\text{C}$.

4. Conclusions

The oxidation of TRISO particles with the outer layers of SiC in air environment was investigated at the temperature range of 900 $^{\circ}\text{C}$ –1400 $^{\circ}\text{C}$. The SiC layer had a good oxidation resistance at a temperature below 1100 $^{\circ}\text{C}$. The silica formed was amorphous at 1200 $^{\circ}\text{C}$ –1300 $^{\circ}\text{C}$ and gradually crystallized at 1400 $^{\circ}\text{C}$ with the major phase of α -cristobalite. The presence of carbon was detected after oxidation above 1200 $^{\circ}\text{C}$. Besides, the crystallization and phase transformation of silica resulted in the formation of cracks in the silica layer due to the volume change.

The thickness of the silica layer increased obviously with the increase of temperature. The oxidation kinetics of SiC followed the linear-parabolic law. Both the linear and parabolic oxidation rates were calculated according to the relationship between the thickness of the silica layer and the oxidation time. The calculated activation energy was 146 ± 5 kJ/mol, suggesting that the rate-controlling step of the oxidation was the diffusion of the oxygen molecule in silica.

Data Availability

The data used to support the findings of this study are available from the corresponding author upon request.

Conflicts of Interest

The authors declare that they have no conflicts of interest.

Acknowledgments

The authors would like to acknowledge the funding from the projects supported by the Natural Science Foundation of Hunan Province (no. 2020JJ3487), The Research Foundation of Education Bureau of Hunan Province (no. 18C0450), The Opening Project of Cooperative Innovation Center for Nuclear Fuel Cycle Technology and Equipment (no. 2019KFY22), and College Students' Innovation and Entrepreneurship Training Program of Hunan Province (no. s201910555095).

References

- [1] X. W. Zhou and C. H. Tang, "Current status and future development of coated fuel particles for high temperature gas-cooled reactors," *Progress in Nuclear Energy*, vol. 53, no. 2, pp. 182–188, 2011.
- [2] P. A. Demkowicz, B. Liu, and J. D. Hunn, "Coated particle fuel: historical perspectives and current progress," *Journal of Nuclear Materials*, vol. 515, pp. 434–450, 2019.
- [3] L. L. Snead, T. Nozawa, Y. Katoh, T.-S. Byun, S. Kondo, and D. A. Petti, "Handbook of SiC properties for fuel performance modeling," *Journal of Nuclear Materials*, vol. 371, no. 1–3, pp. 329–377, 2007.
- [4] Z. Chen, X. Chen, Y. Zheng et al., "Air ingress analysis of chimney effect in the 200 MWe pebble-bed modular high temperature gas-cooled reactor," *Annals of Nuclear Energy*, vol. 106, pp. 143–153, 2017.
- [5] C. I. Contescu, R. W. Mee, P. Wang, A. V. Romanova, and T. D. Burchell, "Oxidation of PCEA nuclear graphite by low water concentrations in helium," *Journal of Nuclear Materials*, vol. 453, no. 1–3, pp. 225–232, 2014.
- [6] W. Xu, J. Sun, Y. Zheng, and L. Shi, "The influence of nuclear graphite oxidation on air ingress accident of HTR-PM," *Annals of Nuclear Energy*, vol. 110, pp. 1242–1248, 2017.
- [7] J. J. Lee, T. K. Ghosh, and S. K. Loyalka, "Oxidation rate of graphitic matrix material in the kinetic regime for VHTR air ingress accident scenarios," *Journal of Nuclear Materials*, vol. 451, no. 1–3, pp. 48–54, 2014.
- [8] W.-H. Huang, S.-C. Tsai, I.-C. Chiu, C.-H. Chen, and J.-J. Kai, "The oxidation effects of nuclear graphite during air-ingress

- accidents in HTGR,” *Nuclear Engineering and Design*, vol. 271, pp. 270–274, 2014.
- [9] L. Charpentier, M. Balat-Pichelin, and F. Audubert, “High temperature oxidation of SiC under helium with low-pressure oxygen-Part 1: sintered α -SiC,” *Journal of the European Ceramic Society*, vol. 30, no. 12, pp. 2653–2660, 2010.
- [10] L. Charpentier, M. Balat-Pichelin, H. Glénat, E. Bêche, E. Laborde, and F. Audubert, “High temperature oxidation of SiC under helium with low-pressure oxygen. Part 2: CVD β -SiC,” *Journal of the European Ceramic Society*, vol. 30, no. 12, pp. 2661–2670, 2010.
- [11] K. Dawi, M. Balat-Pichelin, L. Charpentier, and F. Audubert, “High temperature oxidation of SiC under helium with low-pressure oxygen. Part 3: β -SiC-SiC/PyC/SiC,” *Journal of the European Ceramic Society*, vol. 32, no. 2, pp. 485–494, 2012.
- [12] S. Ueta, J. Sumita, T. Shibata et al., “R & D plan for development of oxidation-resistant graphite and investigation of oxidation behavior of SiC coated fuel particle to enhance safety of HTGR,” *Nuclear Engineering and Design*, vol. 271, pp. 309–313, 2014.
- [13] C. Tang, B. Liu, Z. Li, Y. Quan, H. Zhao, and Y. Shao, “SiC performance of coated fuel particles under high-temperature atmosphere of air,” *Nuclear Engineering and Design*, vol. 271, pp. 64–67, 2014.
- [14] R. Liu, B. Liu, K. Zhang, M. Liu, Y. Shao, and C. Tang, “High temperature oxidation behavior of SiC coating in TRISO coated particles,” *Journal of Nuclear Materials*, vol. 453, no. 1–3, pp. 107–114, 2014.
- [15] K. A. Terrani and C. M. Silva, “High temperature steam oxidation of SiC coating layer of TRISO fuel particles,” *Journal of Nuclear Materials*, vol. 460, pp. 160–165, 2015.
- [16] D. Das, J. Farjas, and P. Roura, “Passive-oxidation kinetics of SiC microparticles,” *Journal of the American Ceramic Society*, vol. 87, no. 7, pp. 1301–1305, 2004.
- [17] M. A. Pimenta, G. Dresselhaus, M. S. Dresselhaus, L. G. Cançado, A. Jorio, and R. Saito, “Studying disorder in graphite-based systems by Raman spectroscopy,” *Physical Chemistry Chemical Physics*, vol. 9, no. 11, pp. 1276–1290, 2007.
- [18] H. Katsui, M. Oguma, T. Goto, and N. Jacobson, “Carbon interlayer between CVD SiC and SiO₂ in high-temperature passive oxidation,” *Journal of the American Ceramic Society*, vol. 97, no. 5, pp. 1633–1637, 2014.
- [19] J. Eck, M. Balat-Pichelin, L. Charpentier, E. Bêche, and F. Audubert, “Behavior of SiC at high temperature under helium with low oxygen partial pressure,” *Journal of the European Ceramic Society*, vol. 28, no. 15, pp. 2995–3004, 2008.
- [20] B. E. Deal and A. S. Grove, “General relationship for the thermal oxidation of silicon,” *Journal of Applied Physics*, vol. 36, no. 12, pp. 3770–3778, 1965.
- [21] D. S. Fox, “Oxidation behavior of chemically-vapor-deposited silicon carbide and silicon nitride from 1200°C to 1600°C,” *Journal of the American Ceramic Society*, vol. 81, pp. 945–950, 1998.
- [22] T. Goto and H. Homma, “High-temperature active/passive oxidation and bubble formation of CVD SiC in O₂ and CO₂ atmospheres,” *Journal of the European Ceramic Society*, vol. 22, no. 14–15, pp. 2749–2756, 2002.
- [23] J. Wang, L. Zhang, Q. Zeng, G. L. Vignoles, L. Cheng, and A. Guette, “The rate-limiting step in the thermal oxidation of silicon carbide,” *Scripta Materialia*, vol. 62, no. 9, pp. 654–657, 2010.